

ResearchOnline@JCU

This file is part of the following reference:

Fernando Pinheiro Andutta (2012) *Water dynamics and transport timescales of coastal waters and estuaries.* PhD. thesis, James Cook University.

Access to this file is available from:

<http://eprints.jcu.edu.au/27181>

*The author has certified to JCU that they have made a reasonable effort to gain permission and acknowledge the owner of any third party copyright material included in this document. If you believe that this is not the case, please contact ResearchOnline@jcu.edu.au and quote [**http://eprints.jcu.edu.au/27181**](http://eprints.jcu.edu.au/27181)*

Water dynamics and transport timescales of coastal waters and estuaries



Thesis submitted by:

Fernando Pinheiro ANDUTTA DSc MSc BSc

In February 2012

for the degree of Doctor of Philosophy

in the School of Mathematics, Physics, and Information Technology

James Cook University

STATEMENT OF SOURCES

DECLARATION

I declare that this thesis is my own work and has not been submitted in any form for another degree or diploma at any university or other institution of tertiary education. Information derived from the published or unpublished work of others has been acknowledged in the text and a list of references and bibliography is given.

Fernando Pinheiro Andutta

/ /2012
Date

ELECTRONIC COPY

I, the undersigned, the author of this work, declare that the electronic copy of this thesis provided to the James Cook University Library is an accurate copy of the print thesis submitted.

Fernando Pinheiro Andutta

/ /2012
Date

STATEMENT ON THE CONTRIBUTION OF OTHERS

The contributions of others include knowledgeable discussions and proofreading of manuscripts. Part of travels to attend conferences, symposiums and others was covered by my mentor Peter V. Ridd, while another part was covered either by the Graduate Research School fund or personally. Fees and stipend support were paid by an International Postgraduate Research Scholarship.

Fernando Pinheiro Andutta

/ /2012
Date

ACKNOWLEDGEMENTS

I am heartily thankful to my mentors, Peter Ridd and Eric Wolanski, whose support, encouragement and guidance enabled me to develop as a researcher and a scientist. I owe my deepest gratitude for the comments on the scientific articles comprised in this thesis from the scientists, Luiz B. de Miranda, Lisa Lucas, David Prandle. Moreover, I would like to thank the kind assistance of Jonathan Lambrechts and other fellows in the use of the SLIM model. Lastly, I offer my regards and blessings to my family, to all friends and staff at James Cook University and those who supported me in any respect during the completion of this thesis.

Fernando Pinheiro Andutta

ABSTRACT

The transport time scales of water have been of considerable interest to marine biologists and biological oceanographers, as they are important parameters to determine aquatic ecosystem health and sensitivity to pollution threats (Lucas et al., 2009; McLusky and Elliott, 2004; Wolanski, 2007; Wolanski, et al., 2012). This thesis has two major components, (a) application of a numerical model to determine transport timescales of the GBR (Great Barrier Reef), and (b) the development and application of a new analytical model to determine timescales for river estuaries.

The SLIM model was used for the numerical simulations in the GBR (SLIM: Second-generation Louvain-la-Neuve Ice-ocean Model). The simulations were run with the Eulerian and Lagrangian schemes depending upon the application. This is the first model of the GBR that has been calibrated to accurately model mixing processes, which was done by comparison of model results with measurements of the hypersaline conditions of the dry season. The model properly simulated the rise of the salinity concentration, and the time to achieve steady state conditions in the dry season.

Model results of the hypersaline coastal waters in the central Great Barrier Reef have shown that the hypersaline waters formed near the coast and inside the bays are exported along the coast from bay to bay during the dry season. The bays supply hypersaline waters to coastal areas. The cross-shelf gradient of the hypersaline waters is mainly controlled by turbulent diffusion, whereas along the coast the salinity gradient is controlled by the residual currents due to the North Caledonia Jet inflow (NCJ) and the wind driven currents.

Results of the flushing time and the age of waters from the North Caledonia Jet inflow into the GBR were estimated under realistic boundary forces. The wind decreases the flushing time in the bays. In contrast, in coastal waters the wind may increase this timescale because the normal southerly flow due to the ocean inflow is opposed by the northward directed wind stress. A typical flushing time for the GBR under real wind conditions was about 70 days.

The sticky water effect in the Great Barrier Reef was estimated quantitatively using the SLIM model. It was demonstrated that some reef configurations result in high exposure time, which depends on the reef density (i.e. degree of aggregation by reefs). Two empirical formulations to estimate larvae retention within the reef matrix were

provided. One formula required measurement of tidal and mean currents, and the other formula, that was less accurate, requires only information of the bathymetry and reef density.

The transport time scales, namely water renewal, residence time and exposure time were calculated using analytical solutions for a range of estuaries worldwide, and the results were compared with residence time results from numerical models where estimates were available. A new modified LOICZ model has been developed that quantifies the relative contribution of advection and diffusion to water renewal in estuaries using simple measurements of river discharge, salinity and the estuarine geometry. The modified LOICZ model resulted in the best fit against numerical results. A graphic conceptual model, the advection/diffusion timescale diagram, was also developed, which was used to visualize where different estuaries lie in the advective/diffusive timescale space diagram. Estuaries can now be divided into those which are dominated by diffusion, those which are dominated by advection and those where diffusion and advection are of similar magnitude.

CONTENTS

List of figures	<i>page</i> v
List of tables	xii
List of acronyms and abbreviations	xv
List of symbols	xvi
1. Introduction	1
1.1 The Great Barrier Reef (GBR)	1
1.2 Challenges in implementing numerical models for the GBR	3
1.3 The finite element numerical model (SLIM)	6
1.4 Objectives and thesis layout	7
2. Dynamics of hypersaline coastal waters in the Great Barrier Reef	9
2.1 Introduction	10
2.2 Methods	12
2.3 Results	15
2.4 Discussion	19
2.5 Conclusions	22
3. Age of Coral Sea inflow shows coastal water trapping in the GBR	23
3.1 Introduction	24
3.2 Methods	26
3.3 Results	31
3.4 Conclusions	39
4. ‘Sticky water’ enables the retention of larvae in a reef mosaic	41
4.1 Introduction	42
4.2 Methods	45
4.3 Results	49
4.4 Discussion and Conclusions	58
5. Review on estuarine hydrology and transport time scales	62
5.1 Introduction	62
5.2 Genesis and geomorphologic time scales	63
5.3 Sediment dynamics time scales	67
5.4 Classification based on geomorphology and on water circulation	70
5.5 Biological implications of sediment transport	71
5.6 Tidal wetlands	72

	iv
5.7 The water transport time scales	73
5.8 Ecological implications of the transport time scales	79
6. Using field data for estimating estuarine water transport timescales and the associated return coefficient	83
6.1 Introduction	84
6.2 The LOICZ model	90
6.3 The modified LOICZ model	92
6.4 The difference between the water renewal time calculated from the LOICZ model and the modified LOICZ model	93
6.5 The CART analytical model	95
6.6 Results and discussion	99
6.7 Summary and conclusions	107
7. CONCLUSIONS	109
Appendix 1: Oceanographic features of the Curimataú Estuary	113
Appendix 2: Oceanographic features of the Caravelas Estuary	114
Appendix 3: Oceanographic features of the Peruípe Estuary	115
Appendix 4: Oceanographic features of the Hudson Estuary	116
Appendix 5: Oceanographic features of the Conwy Estuary	117
Appendix 6: Oceanographic features of the Mersey Estuary	118
Appendix 7: Oceanographic features of the Scheldt Estuary	119
Appendix 8: Oceanographic features of the York River Estuary	120
References	121
Bibliography for chapter 5	136

LIST OF FIGURES

CHAPTER 2:

Figure 2.1 – Location map of the central section of the Great Barrier Reef (Queensland, Australia). Field data sites of tidal currents (●), residual currents (+) and the salinity sites (1-6) along the transect (blue line). Details of bathymetry and salinity sites are shown in the inset. NCJ= North Caledonia Jet; EAC = Eastern Australian Current; NQC = North Queensland Current. The residual currents are indicated by the black arrows. The dominant direction of the tidal currents is indicated by the double pointed brown arrows, **p. 11**.

Figure 2.2 – (A) The numerical mesh of the whole GBR, (B) the bathymetry of the high resolution area, and (C) high resolution area of the numerical grid. Q denotes the location of the Coral Sea inflow. a, b and c denote Cleveland Bay, Bowling Green Bay and Upstart Bay, respectively, **p. 14**.

Figures 2.3 – Time series-plot of (A) the salinity (psu) at site 1 – inshore – as observed (year 1979) and predicted for different values of the Coral Sea inflow and the factor f in Eq. 1. (B) Observed and predicted salinity without wind at the six sites in the cross-shelf salinity transect, where periods of neap tides (n) and spring tides (s) are indicated. (C) Observed (dots) and predicted (continuous lines) salinity with the variable wind stress, **p. 16**.

Figure 2.4 – Predicted salinity distribution at steady state (A) in the presence of the wind and (B) assuming no wind. a, b and c denote Cleveland Bay, Bowling Green Bay and Upstart Bay, **p. 18**.

Figure 2.5 – Comparison between hypersalinity systems in Australia. In Spencer Gulf the hypersaline waters may be flushed out along the seabed at neap tides by salinity-driven baroclinic currents. In contrast, the waters in the shallow Hervey and Shark bays are vertically well-mixed, thus the hypersaline waters are trapped. In the shallow GBR the hypersaline waters are transferred sideways from bay to bay by the residual currents

and thus forming a coastal boundary layer of hypersaline waters. S1 to S3 indicate the increase of salinity towards inshore areas, **p. 21**.

CHAPTER 3:

Figure 3.1 – (A) Map of Australia indicating the GBR location, (B) the numerical grid of the whole Great Barrier Reef with the resolution from about 150 m to 22 km, and location of the Coral Sea inflow Q (between a and b) used in the simulation. (C) The central section of the Great Barrier Reef lagoon, located north-eastern Australia. The mean flushing time was estimated for the bays B1-B5, and the (S_i) South inshore, (S_m) South middle zone, (C_i) Central inshore, (C_m) Central middle zone, (N_i) North inshore and (N_m) North middle zone. The arrows indicate the residual currents, **p. 27**.

Figure 3.2 – The flushing time (A) for conditions C_2 and (B) for condition C_4 , shown for the first month of simulation. Results shown in (A) and (B) are for the bays B1-B5, and the zones (S_i) South inshore, (S_m) South middle, (C_i) Central inshore, (C_m) Central middle, (N_i) North inshore and (N_m) North middle (Fig. 3.1). (C) is the flushing time for the whole Central GBR, i.e. the 6 zones + 5 bays, which is shown for the first 3 months of simulation under conditions C_1, C_2, C_3, C_4, C_5 . (D) is the daily averaged real wind measured at Rib Reef weather station ($18^{\circ}28'50''S, 146^{\circ}52'12''E$) starting on 1st of August 2006. All results from the different conditions are summarized in Table 3.2, **p. 34**.

Figure 3.3 – (A) Alongshore travel distance of particles deployed initially at ($19^{\circ}S, 147^{\circ}E$), location near Townsville in inshore waters in the zone N_i (see figure 3.1). For conditions C_2 to C_5 . Age of the NCJ inflow in days is shown for conditions C_2 (B), C_3 (C), C_4 (D), and C_5 (E), **p. 36**.

Figure 3.4 – (A) Model description of the age from the Coral Sea inflow under an idealized condition of long term calm weather. Age shows faster water renewal in the outer GRB than for areas over reefs and between the reef matrix and the coast. High reef density areas waters are poorly renewed. U_i denotes the direction of tidal current between high reef density areas and the coast, and U_R the residual velocity. (B) Conceptual model describing long term trapped water forming a coastal boundary layer

increasing width southwards. The coastal water trapping is caused by fluctuating southeasterly trade wind combined with the residual circulation from the Coral Sea inflow. (C) MODIS chlorophyll-a image of the central and southern GBR showing oceanic (blue) water intruding in the central GBR and flowing southward inshore of the high reef density area. Red is high Chlorophyll-a or turbid water; blue is low Chlorophyll -a water; and black is land and cloud (Steinberg, 2007). (D) MODIS satellite view of ocean color of the central GBR on August 9, 2011. The satellite view indicated a coastal boundary layer with its width increasing southwards, and similar to the conceptual model (B), **p. 38**.

CHAPTER 4:

Figure 4.1 – (a) Sketch of the sticky water effect in a reef matrix over a continental shelf, showing (lines) streamlines of the residual current and (crosses) the tidal ellipses. (b) Definition of the reef architecture, **p. 44**.

Figure 4.2 – (A) Location map showing the grid over the whole GBR; the high resolution near reefs is highlighted by a zoom on the Swain reef area where were located three virtual spawning areas namely, (a) large dense archipelago, (b) large medium density archipelago and (c) large low density archipelago. (B) Map of the southern and central regions of the Great Barrier Reef, Australia. Field data sites of tidal currents (red dots), residual currents (green dots) and the salinity transect (blue line); (NCJ) North Caledonia Jet; (EAC) Eastern Australian Current; (NQC) North Queensland Current. Residual circulation indicated by the black arrows, and the dominant direction of the tidal currents is indicated by the double pointed brown arrows. The Coral Sea inflow was applied along the orange line. The squares (a) to (q) indicate the location of the virtual spawning sites in areas of different architecture. (C) Location of current meters in the sticky water experiment of Wolanski and Spagnol (2000) and used in this study to demonstrate that the mean currents are deflected around a high reef density area, **p. 47**.

Figure 4.3 – Predicted residual currents and the peak tidal currents during flood and ebb in the Swain reef area, **p. 51**.

Figure 4.4 – (A) Distribution of the virtual larvae plume after 12 days originating from three spawning sites in the Swain reef area, namely, (a) high-density archipelago, (b) medium-density archipelago and (c) low-density archipelago. (B) Time-series plot of the percentage of larvae remaining in the (10 by 10 km box) of the areas a, b, c and l (area characteristics see Table 4.2), and the simulation started at 1st of August 2006. The mean residence time is the time needed for the number of larvae inside the box to decrease to 0.37 its initial value (Deleersnijder et al., 2001), **p. 53**.

Figure 4.5 – MODIS chlorophyll-a image of the central and southern GBR showing oceanic (blue) water intruding in the central GBR and flowing southward inshore of the high reef density area. Red is high Chlorophyll-a or turbid water; blue is low Chlorophyll -a water; and black is land and cloud (Steinberg, 2007). The Swain reef area is indicated, and shows hot spots of high chlorophyll concentration in high reef density areas in agreement with our estimates of the sticky water effect, **p. 55**.

Figure 4.6 – Scatter plot of the residence time T2 predicted by the SLIM model against the residence time T1 predicted by Eq. (4.1) for (A) calm weather (no wind) and (B) southeasterly wind of 6.67 m s^{-1} . Residence time T2 predicted by the SLIM model against the residence time T1 predicted by Eq. (4.2) for (A) calm weather (no wind) and (B) southeasterly wind of 6.67 m s^{-1} . The figure indices (n) and (s) denotes simulations starting at neap (1st of August 2006) and spring tides (8th of August 2006), respectively, **p. 57**.

CHAPTER 5:

Figure 5.1 – (a) Time series plot of the global mean sea level over the last 140,000 years. (b) The approximate distribution of the coasts that followed one of the three typical relative mean sea-level curve types A, B and C as shown in (c). (Redrawn from Wolanski et al., 2009), **p. 64**.

Figure 5.2 – A sketch of the net sediment budget in an estuary, **p. 65**.

Figure 5.3 – The geomorphologic age of macro-tidal, muddy estuaries in the Pacific, **p. 65**.

Figure 5.4 – A sketch of the sediment budget in the micro-tidal Nile and Colorado deltas (a) before and (b) after dam construction, **p. 66**.

Figure 5.5 – Three typical vertical profiles of suspended sediment concentration in estuaries, where a, b, and c denote a nearly well-mixed profile, slightly mixed and a step structure (known as lutocline), **p. 68**.

Figure 5.6 – (a) The physical filter of fine sediment that generates (b) a turbidity maximum zone, i.e. a zone with the highest suspended sediment concentration (SSC); the SSC curve varies with the tides. (c) Biologically-produced transparent exopolymer particles and fine sediment in suspension interact to produce muddy marine snow flocs that accelerate the settling of the mud and generate a biological filter inhibiting the export of fine sediment seaward. (d) Riverine mud is diluted by estuarine mud, **p. 69**.

Figure 5.7 – Classification of estuaries based on the physical oceanography, **p. 71**.

Figure 5.8 – (a) The tidal prism box model (side view); (b) the gravitational circulation box model (side view); (c) the LOICZ box model for a vertically well-mixed estuary (plan view), **p. 75**.

Figure 5.9 – Path followed by a particle in the estuary from the upstream boundary to the coastal sea. At time t , the age of the particle is $t-t_0$, its residence time is t_1-t , its transit time is (t_1-t_0) , its exposure time is $(t_1-t)+(t_3-t_2)$, **p. 77**.

Figure 5.10 – (a) A typical pelagic food web in a vertically well-mixed estuary. It comprises a waterborne ecosystem (the blue box) that is moving with the water currents, thus comprising an inflow into the estuary and an outflow from the estuary; it is flushed at a rate determined by the water transport time scales. It comprises also suspended sediment that is also varying in time at a rate determined by the sediment transport time scales. It comprises also a benthos and bottom dwelling animals living in habitats that are varying in time at a rate determined by the geomorphologic time scale. (b) Typical salinity distribution increasing from the head to the mouth. The waterborne ecosystem (blue box) is advected seaward, thus remaining only in transient contact with

the substrate and the tidal wetlands, and at the same time it is subject to increasing salinity as a result of mixing. As it moves towards the head of the estuary, the waterborne ecosystem also encounters different habitats, **p. 80**.

Figure 5.11 – A sketch of the water circulation in a salt wedge estuary. Organic detritus settles from the top layer where it is produced by an algal/plankton bloom. By decaying in the bottom layer this material extracts dissolved oxygen from the water column. Low dissolved oxygen commonly results in the bottom layer. If the inflow rate of dissolved oxygen by oceanic inflow in the bottom layer is smaller than the consumption rate of dissolved oxygen by the decay of organic matter in suspension and on the bottom, anoxia can result, **p. 82**.

CHAPTER 6:

Figure 6.1 – Illustration of the concept of residence and exposure times for a single water particle in the domain between the upstream and downstream open boundaries that are respectively denoted by $x = 0$ and $x = L$. For the particle under consideration, the residence time and exposure time are $\bar{\phi} = t_1$ and $\bar{\Theta} = t_1 + (t_3 - t_2)$, respectively. Timescales related to a single particle are introduced for pedagogical purposes only and actually are physically meaningless, **p. 85**.

Figure 6.2 – (a) A 1-D estuary model; (b) the tidal prism box model (side view); (c) the gravitational circulation box model (side view); (d) the LOICZ box model for a vertically well-mixed estuary (plan view), **p. 89**.

Figure 6.3 – Conceptual description of a generic salinity distribution along an estuary from ($x = L_1$) to the mouth ($S = L_0$). The salinity S' at $x = 0$ where ($0 \leq S' < S_E$), **p. 94**.

Figure 6.4 – Representation of the residence time ϕ (solid curve; Eq. 25) and the exposure time Θ (dashed curve; Eq. 26a,b,c) as a function of the distance x to the upstream boundary of the domain of interest. The timescales are normalised by means of the advective timescale T_l . Various values of the Peclet number are considered: the larger this number, the larger the relative importance of advection and, hence, the

smaller the difference between the exposure time and the residence time. It is noteworthy that the exposure time, as opposed to the residence time, is defined outside the domain of interest ($0 \leq x \leq L$), **p. 97**.

Figure 6.5 – Representation for various values of the Peclet number of the return coefficient as defined by formula (6.26), **p. 98**.

Figure 6.6 – (a) Scatter plot of the water renewal timescale T_P against the maximum residence time from hydrodynamic numerical models. (b) Scatter plot of the diffusive contribution to water renewal ($1 - \theta$) against the return coefficient calculated using CART's formula. Data from all estuaries in table 6.2 aside from Curimataú and Conwy estuaries, **p. 104**.

Figure 6.7 – The position of estuaries on the advection-diffusion diagram to indicate the relative contribution to the water renewal T_P by the advective (T_1) and dispersive (T_2) timescales using a logarithmic scale. Subscript (n) and (s) indicate neap and spring tide conditions. For the Curimataú Estuary (C), K was estimated from Hansen-Rattray's formula. Hudson, Caravelas, Peruípe, and Conwy estuaries are denoted (H), (CA), (P), and (C), respectively. For the Mersey (M), and Scheldt (S) estuaries, results are from an average range. For the York River Estuary the conditions are for high river flow (Y_H), and mean river flow (Y_M). The parameter θ , represented by straight lines, indicates the relative advective contribution to water renewal varying in the range $0 \leq \theta \leq 1$. The diagonal line $\theta = 0.5$, separates the areas where transport is dominated by dispersion (diagram lower zone, $\theta < 0.5$) and advection (diagram upper zone, $\theta > 0.5$), **p. 106**.

LIST OF TABLES

CHAPTER 2:

Table 2.1 – Comparison between observed and predicted alongshore residual currents (m s^{-1}) of six sites (+) shown in Fig. 2.1. Predicted residual currents for different inflows Q (Sv) of the Coral Sea. The root mean square error RMSE (m s^{-1}) is shown in the last row. The data sources *, ** and *** are respectively Andrews (1983), Wolanski et al. (1989), and Spagnol et al. (2001). Northward and southward currents are represented by (N) and (S), respectively, **p. 12**.

Table 2.2 – The root mean square error RMSE of the salinity (psu) at sites 1 to 6 (Figure 2.1) for different inflows Q (Sv) of the Coral Sea, and the factor f in Eq. 2.1, **p. 17**.

CHAPTER 3:

Table 3.1 – Five boundaries conditions applied to the numerical simulations to estimate the flushing time and the age of waters in the Great Barrier Reef, **p. 28**.

Table 3.2 – Observed (U_o) and predicted (U_p) longshore residual currents in a range for conditions (C_2) under calm weather, (C_3) fluctuating wind of 6.67 m s^{-1} , (C_4) fluctuating wind of 10 m s^{-1} and (C_5) for a real wind condition (>0 if northward, <0 if southward) and peak tidal currents (U_T) at mooring sites. The wind condition does not affect the tidal currents, and thus U_T does not change. Data from the table extracted from Andutta et al. (2011) and Andutta et al. (pers. comm.). The root mean square error for velocity RMSE (m s^{-1}), **p. 30**.

Table 3.3 – The average flushing time T (in days) and the concentration of a passive tracer (in %) remaining after 12 and 24 days. The results are for the simulations assuming conditions (C_1), (C_2), (C_3), (C_4) and (C_5). Results are for the bays B1-B5, and the zones (S_i) South inshore, (S_m) South middle, (C_i) Central inshore, (C_m) Central middle, (N_i) North inshore and (N_m) North middle (Fig. 3.1). Central GBR rows show the flushing time for all the zones and bays. The return coefficient r calculated for

conditions C_1 and C_2 was nearly zero, while for conditions C_3 , C_4 and C_5 is shown in the table, **p. 33**.

CHAPTER 4:

Table 4.1 – Observed (U_o) and predicted (U_p) longshore residual currents ($m\ s^{-1}$, >0 if northward, <0 if southward) and peak tidal currents (U_T , in $m\ s^{-1}$) at mooring sites. The location of the current meter mooring sites is shown in Figure 2. The data sources A, B, C and D refer respectively to Andrews (1983), Wolanski et al. (1989), Spagnol et al. (2001) and Middleton and Cunningham (1984). The root mean square error RMSE ($m\ s^{-1}$) is shown in the last row, **p. 50**.

Table 4.2 – Location, reef architecture characteristics, and the reef cover parameter A and the lagoon closure parameter B of the 10 x 10 km spawning sites shown in Figure 4.2. The exposure time T_1 (in days) under calm weather, is estimated for simulations starting and neap (1st of August 2006) and spring tides (8th of August 2006). During calm weather conditions and for a simulation starting under neap tides, the table shows the relative number N_1 and N_2 (in %) of larvae remaining in the spawning sites after 12 and 24 days respectively. During windy conditions and for a simulation starting at neap tides, the residence time T_2 (in days) of the spawning sites. U_{R1} and U_{R2} ($m\ s^{-1}$) are the residual currents in the spawning sites under calm weather and windy conditions, respectively. U_T ($m\ s^{-1}$) is the peak tidal current averaged spatially in the spawning sites, **p. 54**.

CHAPTER 5:

Table 5.1 – Example of the water transport times (in days) for various vertically fairly well-mixed estuaries, **p. 79**.

CHAPTER 6:

Table 6.1 – Water renewal timescale (days) of the Curimataú, Caravelas, Peruípe, Hudson, Conwy, Scheldt and York estuaries. For the Curimataú Estuary, A denotes the diffusion timescale using horizontal diffusion calculated from Fisher's formula while B

uses Hansen-Rattray's formula. The advection contribution to water renewal is $\theta = T_p / T_a$ and $\theta_{LOICZ} = T_{LOICZ} / T_2^{LOICZ}$. The diffusion coefficient k^{LOICZ} was estimated using Eq. 6.12, i.e. $K^{LOICZ} = L Q_R 0.5(S_O + S_E) / A(S_O - S_E)$, and k was estimated using equations 6.17 and 6.18 combined, i.e. $K = L Q_R S_E / A(S_O - S')$, **p. 102**.

Table 6.2 – The mean residence time ($\bar{\phi}_{CART}$ in days), mean exposure time ($\bar{\Theta}_{CART}$ in days), and the return coefficient of the Curimataú, Caravelas, Peruípe, Hudson, Conwy, Mersey and Scheldt estuaries. The Peclet number $P_E = u L / K$ was calculated using the diffusion coefficient K from Fisher's formula (see caption of Table 6.1), which was used in our method. $\bar{\phi}_a$ and $\bar{\Theta}_a$ correspond to the mean advective timescale in the residence time and exposure time, respectively, **p. 103**.

LIST OF ACRONYMS AND ABBREVIATIONS

Acronym/Abbreviation	Meaning
GBR	Great Barrier Reef
EAC	Eastern Australian Current
NCJ	North Caledonia Jet
NQC	North Queensland Current
RMSE	Root Mean Square Error
SLIM	Second-generation Louvain-la-Neuve Ice-ocean Model
LOICZ	Land-Ocean Interaction in the Coastal Zone
CART	Constituent-oriented Age and Residence time Theory
MODIS	Moderate Resolution Imaging Spectroradiometer
PLD	Planktonic Larval Duration
PSU	Practical Salinity units
1D	One dimension
2D	Two dimensions
3D	Three dimensions
N	North
S	South
E	East
W	West
M_2	Principal Lunar Semi-diurnal
S_2	Principal Solar Semi-diurnal
N_2	Elliptical Lunar Semi-diurnal
K_2	Declination Lunar Solar Semi-diurnal
K_1	Declination Lunar Solar Diurnal
O_1	Principal Lunar Diurnal
P_1	Principal Solar Diurnal

LIST OF SYMBOLS

Symbol	Units	Description
K	$\text{m}^2 \text{s}^{-1}$	Diffusion coefficient
L	m	Length
H	m	Mean depth
T	s	time
U_T	m s^{-1}	Water tidal current
U_O	m s^{-1}	Mean water current
u	m s^{-1}	Water current
g	m s^{-2}	Gravity acceleration
τ	N m^{-2}	Stress due to bottom friction or wind (depend on context)
C	$\text{m}^{1/2} \text{s}^{-1}$	Chezy coefficient
Sv	$10^6 \text{m}^3 \text{s}^{-1}$	Sverdrup units
P_E	non-dimensional	Peclet number

CHAPTER 1

1. INTRODUCTION

The studies of transport time scales of water have been of considerable interest to biological oceanographers, marine biologists and researcher of related areas. Time scales are essential parameters to analyse a marine ecosystem health and sensitivity to pollution threats, and indicate the capacity of water renewal in a water body (e.g. estuaries, bays, lagoons etc). This manuscript comprises two major components, the first part of this thesis focus on the application of a numerical model to determine transport timescales of the Great Barrier Reef (GBR), and the second component refers to the development and application of a new analytical model to determine timescales for estuarine ecosystems, this new method is further compared with existent simple methods.

1.1 The Great Barrier Reef (GBR)

The Great Barrier Reef of Australia (Fig. 2.1), located on the northeastern continental shelf of Australia, is the largest coral reef ecosystem and one of the wonders of the natural world. The GBR is comprised of more than 2,800 individual reef scattered over its 2,600 km length (Pickard et al. 1977). The GBR has a highly complex topography, with individual reefs ranging in area from 0.01 to 100 km², often separated by very narrow passages (i.e. dozens to hundreds of meters). The continental shelf water depth tends to slope to 100 m at the shelf break, approximately (Pickard et al., 1977). The circulation on the GBR shelf is strongly influenced by the interaction between its complex topography, the wind, the tides and the circulation in the adjoining Coral Sea (Wolanski, 1994).

Currently, there is concern that coral reefs around the world are showing rapid degradation at a global scale due to human impacts. Although the GBR lagoon is one of the best managed of the world's coral reef ecosystems, many scientists are of the view that even this large and relatively unspoiled ecosystem is under threat from anthropogenic impacts. The nutrients and sediment running off the adjacent catchments

are thought to have influenced considerably both, health and productivity of the whole Great Barrier Reef ecosystem. The sediment and nutrient runoff to the reef has changed since 1850 by human activities in the catchments bordering the lagoon (Furnas, 2003). Nutrient and sediment inputs have increased by roughly a factor of 10 and 4 respectively.

There is some debate in the scientific community regarding the measurement and quantification of anthropogenic effects in GBR, especially related to the impacts from agriculture. Those impacts are not well understood, but it has been observed in other systems that high nutrient levels increase algae cover and decrease the coral cover (Furnas, 2003). For example in the reefs of Kaneohe Bay in Hawaii, a well-known instance of eutrophication occurred due to a sewage outfall discharging onto the reef flat (Hunter and Evans, 1995) and caused a phase shift from coral to algal communities. The long-term effect of pesticides on the GBR is largely unknown, however low concentrations of Diuron, an agricultural herbicide, have been already measured in the GBR lagoon (Haynes et al., 2000a,b). Several other pesticides mainly herbicides were detected in fresh and coastal water along the GBR coast and have been specifically attributed to land uses in catchments (Lewis, et al., 2009).

An important factor determining the effect of pollutants in a water body is the transport timescales such as the residence time. Long residence times such as in the Baltic Sea 25 years (Kremling and Wilhelm, 1997) and Sydney Harbor with 225 days (Das, P, et al. 2000) allow limited removal of pollutants. Short residence times mitigate against the buildup of pollutant concentrations. The transport time scales of water in an aquatic environment has long been of interest to biological oceanographers because it is an important parameter to determine the estuarine ecosystem health as well as its sensitivity to pollution threats (Lucas et al., 2009; McLusky and Elliott, 2004; Wolanski, 2007). It is difficult to estimate adequately those timescales from observations because it is necessary to introduce a large number of physical tracers into a system, and tracking those tracers involves much work. An alternative approach is to model the timescales in the GBR with Eulerian simulations or numerical Lagrangian models using a system release of thousands of virtual tracers (Wolanski, 2007).

Transport time scales in the Great Barrier Reef are key to understand the removal of pollutants from the GBR. This thesis aims is to use a high-resolution non-structured numerical model to estimate the transport timescales namely, flushing time

and the age of waters in the GBR. Different methods have already been used to estimate different definitions of time scales in the GBR, and results have shown both relatively short, *ca.* a few weeks (Hancock et al., 2006; Wang et al., 2007; Choukroun et al., 2010) or large time scales (Luick et al., 2007). Using hydrodynamic models, Luick et al. (2007) has shown the residence time to be up to one year, whereas Hancock et al. (2006) and Wang et al. (2007) found much shorter estimates of residence time (a few weeks) using measurements of salinity and radionuclides combined with very simple 1D cross-shelf diffusion models and simple exchange models. The difficulties in dealing with 1D cross-shelf models of the GBR is that they do not account for the transport of water particles along the coast, which is a well-known feature in the GBR (King and Wolanski, 1996; Brinkman et al., 2001; Lambrechts et al., 2008; Andutta et al., 2011).

1.2 Challenges in implementing numerical models for the GBR

It is a challenge to properly model the GBR because of the large scale of the system combined with the small scale of the individual reefs (a few hundred meters). Dight et al. (1990) used a 9.26 km mesh resolution to simulate currents and larval dispersion in the GBR. Brinkman et al. (2001) and King and Wolanski (1996) used a smaller mesh size of nearly 2 km; they showed the importance of the Coral Sea inflow to flush the shelf even in the absence of wind. Luick et al. (2007) used a model with a mesh resolution of 1.8 km to study transport time scales of the GBR. These finite-difference models all suffered from insufficient resolution of the reef matrix as the grid was too coarse to resolve the complex bathymetry that requires a grid of 300 m at most near reefs. These low horizontal resolution models ignored many of the individual reefs less than 2 km in size and their eddies, as well as reef passages between ribbon reefs. Thus they did not simulate properly the dispersive processes near reefs (Deleersnijder et al., 1992; Wolanski et al. 1996; Lambrechts et al., 2008).

The low mesh resolution is a limitation in the simulation of circulation in the complex GBR. Low horizontal resolution models do not resolve many of the individual reefs and eddies, and do not give the right shear distribution from the edges on the wakes of smaller reefs. They thus do not simulate properly the dispersive processes (Deleersnijder et al., 1992; Wolanski et al. 1996). Addressing the problem of high mesh

resolution increasing computational time, an unstructured model using the finite element method was applied to the whole GBR by Lambrechts et al. (2008). The mesh size was calculated as a function of distance from coastal line and bathymetry. Cells of a few hundred meters were used near reefs, islands and the coast, and cells of a few kilometers were used in deeper regions far from the coast and the central GBR. This use of variable dimension cells allows for the appropriate representation of the high velocity shear zones close to reefs and wakes of islands, and also of the tidal jets between narrow passages (e.g. Furukawa and Wolanski, 1997).

The coefficients of horizontal viscosity and diffusivity are another limitation of many models. To simulate sub-grid scale processes, assumptions are required to choose the values of the horizontal eddy diffusion and eddy viscosity coefficients, which usually depend on grid size. Okubo (1971) found an empirical relationship between the apparent diffusivity and the scale of diffusion. From his studies, a diagram was given to predict the rate of the horizontal spread from an instantaneous source. This study did not provide any parameterization to solve turbulent diffusion at the sub-grid scale in numerical models. This turbulent diffusion is likely to depend on the area of each grid cell, as well as on the velocity shear between the boundaries of the grid cell. Smagorinsky (1963) provided a parameterization of the horizontal diffusion of momentum that can be used to calculate the horizontal viscosity coefficient at sub-grid scale in numerical models. The proposed parameterization calculates the horizontal viscosity coefficient from the velocity shear between the boundaries of each grid cell, and is thus dependent on the grid size. Despite this advance, many numerical models still use a constant value for the horizontal viscosity coefficient, which needs to be adjusted and is often unknown a priori.

The simplifications of the boundary conditions also limit simulations. The offshore open boundary conditions of the GBR are forced by tides and water inflow from the adjoining Coral Sea, and this inflow is not always well known in terms of volume and position of entrance. The oceanic inflow inside the GBR is mainly caused by the North Vanuatu Jet (NVJ), the North Caledonian Jet (NCJ) and the South Caledonian jet (SCJ) (Ganachaud et al., 2007; Ganachaud et al., 2008). These jets originate from the South Equatorial Current (SEC) (Andrews and Clegg, 1989). The SEC and the three jets are free inertial turbulent jets (Burrage et al., 1991) of high spatial/time variability. From geostrophic calculations, these currents approach the

shelf-break between 15° S and 20° S (Church, 1987). To adequately represent the circulation within the GBR, Brinkman et al. (2001) adjusted the latitude of the inflow from the NCJ between 14.7° and 16.75° S. The NCJ inflow splits into two branches when meeting the shelf slope; a small part is able to cross the reef matrix mostly in low density reef areas, thus causing a residual onshore circulation inside the GBR (Andutta et al., 2011).

In the central GBR, where the reefs are widely scattered, the low frequency currents and the wind-driven circulation within the lagoon have shown a mean southward current at Myrmidon Reef (Fig. 2.1), in spite of a few occasions of northward currents due to Southeasterly winds (Burrage et al., 1997). The Southeasterly winds may create a northward flow for a few days (Andrews, 1983). In the low reef density zone the tidal currents were found to be oriented across the shelf (Church et al., 1985). South of Myrmidon reef the tidal currents are affected by high reef density. Wolanski and Pickard (1985) observed that the tidal currents were directed in the alongshore shore direction between the high density reef matrix and the coast at the mooring sites of Old Reef and Cape Upstart (Fig. 2.1). In this same area, a low frequency current was observed to the south with occasional northward flow during periods of Southeasterly winds. The residual southward flow splits into two branches as it approaches the high reef density area (Fig. 2.1), one branch channelled between the reef matrix and the coast, and the other beside the reef matrix out from the GBR (Brinkman et al., 2001).

The trade winds from the South-East generate the northward wind driven currents close to the shore inside the shallow GBR. This current overcomes the southward flow due to the Coral Sea inflow and inhibits the southward flushing with new oceanic waters south of the approximate intrusion latitude $\sim 15^{\circ}$ - 20° S (Andutta et al., 2011).

The main harmonic tide components inside the GBR are M_2 , N_2 , S_2 and K_2 , and the diurnal components are O_1 , P_1 , K_1 (Andrews and Bode, 1988). These two groups of components describe over 95% of the high frequency currents in the GBR. The M_2 tide dominates and propagates cross-shelf in the central section, and alongshore elsewhere.

1.3 The finite element numerical model (SLIM)

The SLIM was chosen to be applied for the numerical simulations in the GBR (SLIM: Second-generation Louvain-la-Neuve Ice-ocean Model). SLIM is a free-surface, hydrostatic, primitive equation ocean model that uses terrain following coordinates. SLIM is based on finite element method (FEM) with carries the advantage of using an unstructured mesh. The grid for SLIM is generated using GMSH, which is a three-dimensional finite element grid generator (access: <http://geuz.org/gmsh/>). Unlike all the structured models, the SLIM may vary greatly in the same grid, while for structured models the nesting features may be necessary and not always easily applied. SLIM prompts a single model to be capable of simulating the hydrodynamics at both, the large-scales of oceans and seas and also the small-scale within bays, estuaries and small reef mosaics. The SLIM mesh follows precisely complex coastlines comprising innumerable bays and estuaries. Therefore, this model is suitable for the complex topography of the GBR comprising innumerable islands and reefs of different shapes and sizes.

For the GBR the model was applied using different mesh configurations. The resolution was set to be a function of the bathymetry, distance to coastline and island, and areas of interest. The simulations were run with the Eulerian and Lagrangian scheme for different goals. To simulate the salinity during the dry season in the GBR the Eulerian method was used, while for the estimates of transport time scales we have chosen the Lagrangian method.

The 2D vertical integrated models can be applied to simulate the water circulation in the GBR (e.g. the SLIM), because little vertical stratification of salinity and temperature was found in most areas, aside from river mouths. Luick et al., (2007) has demonstrated that 3-D models may not be needed for the GBR because little vertical stratification of salinity and temperature was found in most areas, aside from river mouths, and thus lasting for the brief wet season. In addition, the temperature field does not affect the local circulation inside the GBR. The absence of significant horizontal gradients inside the relatively shallow GBR, and the nearly vertical, well-mixed waters, leads to a negligible local baroclinic circulation caused by temperature. However, surface heating briefly occurs during calm weather (Pickard et al. 1977).

1.4 Objectives and thesis layout

This thesis comprises separated chapters addressing new findings on the physical oceanography of the GBR and transport timescales of estuaries, and the major objectives were:

- To study the hypersaline coastal waters in the GBR;
- To estimate the flushing time and the age for bays and coastal areas in the GBR;
- To analyse the influence of reef density and reef configurations on water renewal in the GBR;
- To provide a review about the existing estuaries theory and then provide a new method to estimate water renewal in estuaries.

The thesis comprises four scientific papers and a book chapter that have been published or that are still under review. Each scientific manuscript corresponds to an individual chapter of this thesis. The chapters deal with different aspects of the Physical Oceanography in the Great Barrier Reef including the main physical oceanographic features of estuaries.

Chapter two examines the first predictions of the hypersaline coastal waters in the central Great Barrier Reef. The theoretical model results have shown that the hypersaline waters formed near the coast and inside the bays are exported along the coast from bay to bay during the dry season (typically between August and November), and the bays supply hypersaline waters to coastal areas. This chapter shows that the cross-shelf gradient of the hypersaline waters is mainly controlled by turbulent diffusion, whereas along the coast the salinity gradient is controlled by the residual currents due to the Coral Sea inflow and the wind driven currents. The distribution of hypersaline waters in the GBR is 2-D with both cross-shelf and longshore gradients of salinity, and thus differs from many hypersaline estuaries and other systems worldwide.

Chapter three describes estimates of the timescales namely flushing time and the age of waters from the North Caledonia Jet inflow into the GBR. This is the first model that has been calibrated to accurately model mixing processes, i.e. use of the calibrated model described in chapter two, which used measurements of hypersaline waters in the dry season. The transport timescales were estimated under realistic boundary forces, considering different weather conditions and the Coral Sea inflow. This chapter shows

that the wind decreases the flushing time in the bays. However, in coastal waters the wind may increase this timescale because the normal southerly flow due to the ocean inflow is opposed by the northward directed wind stress.

Chapter four addresses the sticky water effect in the Great Barrier Reef (Wolanski, 1994). The calibrated unstructured SLIM model was applied to estimate the retention of waterborne larvae within the reef matrix. A high resolution horizontal mesh was applied to all the reefs comprised between the Swain reef area ($\sim 22^{\circ} 30' S$) and the Ribbon reefs ($\sim 14^{\circ} 30' S$). It was demonstrated using the numerical results that some reef configurations may result in high self-seeding, which relies on the degree of aggregation by reefs and lagoon reef configurations. The sticky water effect for different reef configuration was estimated quantitatively in the GBR. This study provided two empirical formulations to estimate larvae retention within reef matrix; one formula requiring measurement of tidal and mean currents that explains about 68% of the variation in larval retention in both calm weather and windy conditions. The second formula was less accurate, but requires only information of the bathymetry and reef density.

Chapter five describes oceanographic aspects of estuaries. It is known that estuarine waters are more biologically productive than coastal and oceanic waters, moreover, estuaries are important for the reproduction of many marine species in the GBR. Because of this one chapter of this thesis was designated to discuss the genesis of estuaries, the different definitions of transport time scales applied for estuaries and their respective ecological implications.

Within Chapter six, transport time scales namely water renewal, residence time and exposure time were calculated using analytical solutions for a range of estuaries worldwide, and these results were compared with residence time results from numerical models. A new formulation of the LOICZ model has been developed and shown to be more accurate than the original LOICZ scheme. A graphic conceptual model, the advection/diffusion timescale diagram is presented, which was used to visualize where different estuaries lie in the advective/diffusive timescale space diagram.

CHAPTER 2

Dynamics of hypersaline coastal waters in the Great Barrier Reef

Fernando P. Andutta^{1,2}, Peter V. Ridd¹, Eric Wolanski²

¹ School of Engineering and Physical sciences, James Cook University, Townsville QLD 4811, Australia.

² ACTFR, James Cook University, Townsville, QLD, 4811, and Australian Institute of Marine Science, Townsville, Australia.

This chapter reproduces the following paper:

Andutta, F.P., Ridd, P.V., Wolanski, E., 2011. Dynamics of hypersaline coastal waters in the Great Barrier Reef. *Estuarine, Coastal and Shelf Science* 94, 299–305.

Keywords of this chapter: Salinity; evaporation; diffusion; trapping; diffusion-advection balance.

The coastal waters of the Great Barrier Reef (GBR) are hypersaline (salinity ~37) during the dry season as a result of evaporation greatly exceeding rainfall, of shallow waters, and of the presence of numerous bays along the coast preventing rapid flushing. These hypersaline waters are not flushed out by salinity-driven baroclinic currents because these waters are vertically well-mixed. Instead these waters are transported by a longshore residual current and thus form a coastal boundary layer of hypersaline waters. As a result the hypersalinity distribution is 2-D with both cross-shelf and longshore gradients of salinity. The cross-shelf gradients are largely controlled by turbulent diffusion, while the longshore gradients are controlled by the residual currents that transport hypersaline waters longshore south ward in the central and southern regions of the GBR. Because every bay supplies hypersaline waters, the width of the coastal hypersaline layer increases southwards. Steady state is reached in about 100 days, which is the typical duration of the dry season. The dynamics of the GBR hypersaline coastal boundary layer thus differ from the classical inverse hypersaline systems, e.g. in

Saloum River Estuary, Laguna San Ignacio, Mission Bay, Tomales Bay, San Diego Bay, Hervey Bay, Shark Bay, Coorong Coast Lagoon, Spencer Gulf, Gulf of California and many others where the salinity gradient is mainly 1-D with a dominant along-channel salinity gradient.

2.1 Introduction

Hypersaline systems are bodies of water such as estuaries, bays and gulfs with salinity larger than that of the oceanic waters ca. 35.5 (psu). The occurrence of hypersaline waters in estuaries, bays and coastal waters is caused by the excess of evaporation over freshwater input from rainfall and rivers. In such systems, the salinity does not continue to increase indefinitely even though evaporation continues as excess salt is flushed to the ocean by the water circulation (Lennon et al., 1987). Hypersalinity may occur in systems of a wide range of scales, typically from scales of 10's of km such as the estuaries in tropical and sub-tropical Australia, 100's of km such as in Spencer Gulf, the Gulf of California and its lagoons, the Great Australian Bight and the Gulf of Kachchh in the Arabian Sea, and even 1000's of km such as in the Mediterranean Sea and the Red Sea (Phillips, 1966; Lacombe and Richez, 1982; Wolanski, 1986; Nunes Vaz et al., 1990; Bray and Rubles, 1991; Chadwick and Largier, 1999; Valle-Levinson et al., 2001; Gutierrez de Velasco and Winant, 2004; Ribbe, 2006; Vethamony et al., 2007). In most systems hypersalinity is a seasonal phenomenon occurring only in the dry season, but in some systems such as Baja California, Mexico, the hypersalinity may persist throughout the year. As salinity is a conservative tracer, it is possible to use advection-diffusion models to estimate water residence times from observations of hypersalinity (Wang et al., 2007). Such models are easiest to apply in 1-D situations when homogeneity can be assumed both vertically and cross-channel. Hypersalinity (salinity ~ 37), has been reported in coastal waters of the Great Barrier Reef (GBR; Fig. 1) but only during the dry season typically from July to November (Wolanski et al., 1981; Walker, 1981, 1982; Wolanski, 1994). The dynamics of these hypersaline waters are unknown. A closed analytical solution, such a 1-D model (i.e. with a salinity gradient occurring only cross-shelf) suggests that the width of the hypersaline coastal zone depends on the balance between evaporation and cross-shelf diffusion (Wang et al., 2007). Such 1-D models however ignore the patchiness of the hypersalinity

distribution as well as the longshore gradients. In this paper we remove this disadvantage by using a 2-D, high resolution numerical model, verified against field data, to simulate their dynamics. A 2-D model was justified because the baroclinic circulation could safely be neglected as the waters are vertically well-mixed. We show that the dynamics of the GBR hypersaline waters differ from that in most other coastal hypersaline systems.

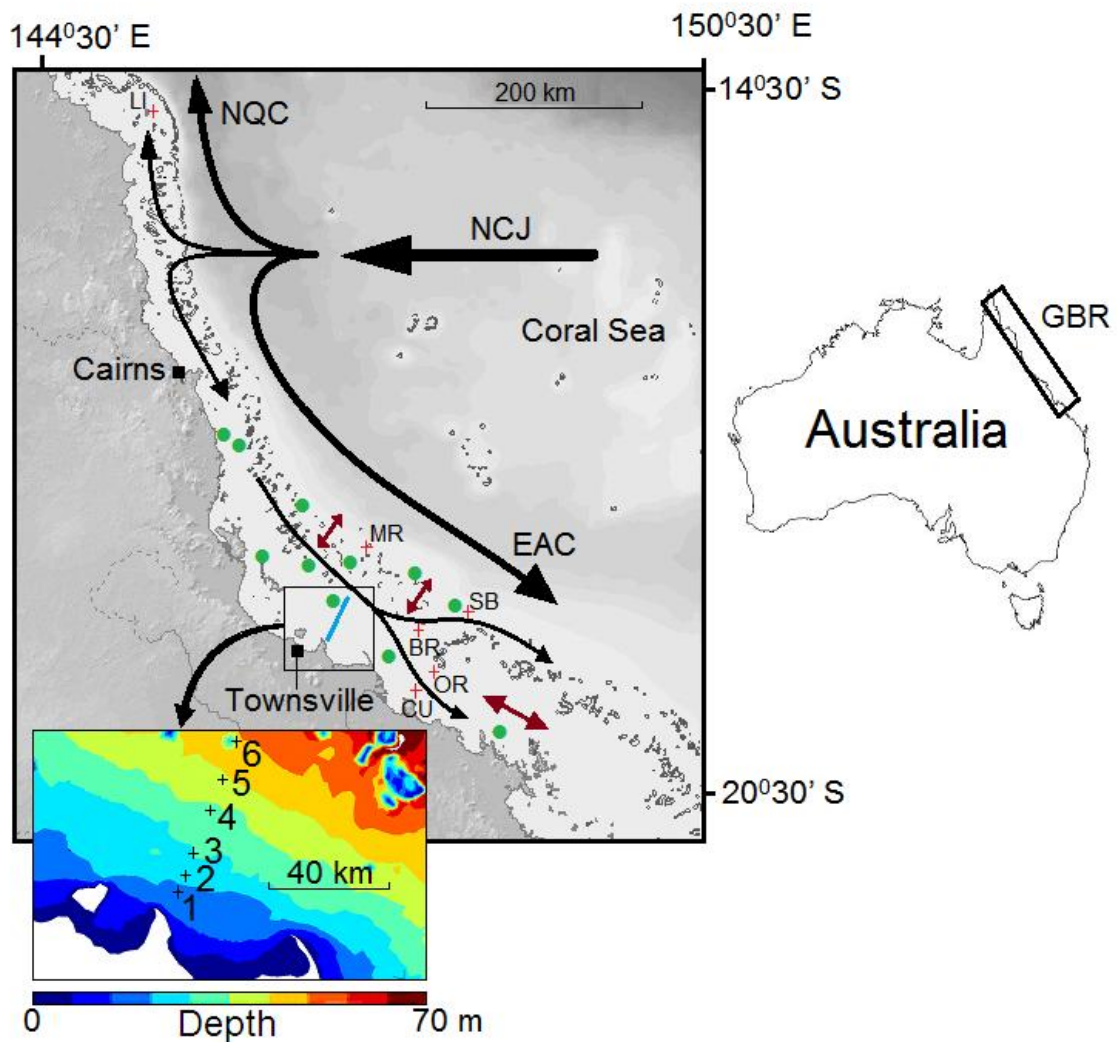


Figure 2.1 – Location map of the central section of the Great Barrier Reef (Queensland, Australia). Field data sites of tidal currents (●), residual currents (+) and the salinity sites (1-6) along the transect (blue line). Details of bathymetry and salinity sites are shown in the inset. NCJ= North Caledonia Jet; EAC = Eastern Australian Current; NQC = North Queensland Current. The residual currents are indicated by the black arrows. The dominant direction of the tidal currents is indicated by the double pointed brown arrows.

2.2 Methods

2.2.1 Field data

The field data on salinity in coastal waters in the dry season are those of Wolanski and Jones (1979) who measured salinity throughout the water column, at weekly intervals, throughout 1979, at six sites along a 58-km long cross-shelf transect shown in the inset of Fig. 2.1. There are only occasional measurements of salinity in the bays in the dry season, namely Walker (1981) for Cleveland Bay in 1978, Wolanski and Ridd (1990) and Sheaves (2006) for Bowling Green Bay in 1985.

Field data of currents (tidal and low-frequency) at six moored current meter sites and of tides at eleven sites were obtained from Andrews and Bode (1988), Andrews (1983), Wolanski and Pickard (1985), Wolanski et al. (1989), and Spagnol et al. (2001). The location of the current meter sites is shown in Fig. 2.1 and details of their location and references are listed in Table 2.1.

Table 2.1 – Comparison between observed and predicted alongshore residual currents (m s^{-1}) of six sites (+) shown in Fig. 2.1. Predicted residual currents for different inflows Q (Sv) of the Coral Sea. The root mean square error RMSE (m s^{-1}) is shown in the last row. The data sources *, ** and *** are respectively Andrews (1983), Wolanski et al. (1989), and Spagnol et al. (2001). Northward and southward currents are represented by (N) and (S), respectively.

Residual currents in the GBR in m s^{-1}								
Site name	Latitude S	Longitude E	observed	Q = 0	Q = 2	Q = 4	Q = 6	Source
Lizard Island LI	14.7406	145.4253	0.05 (N)	0.00 (N)	0.06(N)	0.07(N)	0.10(N)	***
Cape Upstart CU	19.6253	147.9142	0.11(S)	0.01(S)	0.06(S)	0.10(S)	0.10(S)	***
Old Reef OR	19.4071	148.0197	0.10(S)	0.01(S)	0.05(S)	0.09(S)	0.11 (S)	**
near shelf break SB	18.8311	148.2896	0.25(S)	0.01(S)	0.10 (S)	0.20 (S)	0.28 (S)	*
Myrmidon Reef MR	18.2452	147.4100	0.18 (S)	0.01 (S)	0.16 (S)	0.25 (S)	0.31 (S)	*
Bowden Reef BR	19.0600	147.9597	0.1-0.25 (S)	0.00 (S)	0.02 (S)	0.02 (S)	0.03 (S)	**
RMSE	-	-	-	0.14	0.08	0.04	0.07	-

2.2.2 Numerical model

The GBR bathymetry is very complex with ~2800 reefs scattered over its 2600 km length, with individual reefs ranging in area from ~0.01 to ~100 km² and often separated by narrow passages. A high horizontal resolution is required because low resolution models erase the smaller reefs and do not yield the correct shear distribution near the edges of the remaining reefs; thus they do not simulate correctly the dispersive processes (Wolanski et al., 1996). It is an unresolved challenge to use finite-difference, regular grids models to model the whole GBR (King and Wolanski, 1996; Spagnol et al., 2001; Brinkman et al., 2001; Luick et al., 2007). To avoid these disadvantages we have thus used the non-structured grid model SLIM (Lambrechts et al., 2008). The cell size varied from 300m near reefs, headlands and islands and the coast to cells of several kilometers over the shelf far from reefs and the land (Fig. 2.2). We focused the study on the central and southern region of the GBR, thus explaining the high resolution of the grid in these areas. The bathymetry was derived from the data of Webster and Petkovic (2005) with a resolution of 250 m. The maximum depth was 200 m. The offshore open boundary conditions were the tides from TOPEX and the Coral Sea inflow Q (Fig. 2.2). This water inflow in the GBR from the adjoining Coral Sea is an unknown fraction of the North Caledonian Jet (NCJ; Fig. 2.1) (Andrews and Clegg, 1989; Ganachaud et al., 2007). The NCJ generates a southward net current (the East Australian Current) to the south of the separation point and a northward net current (the North Queensland Current, NQC) to the north of the separation point. This inflow is thus little known. It was considered an external parameter to be adjusted until the model predictions for the residual currents match well the observed currents. For the simulations we varied the Coral Sea inflow Q in the range 0–6 Sv ($1 \text{ Sv} = 10^6 \text{ m}^3 \text{ s}^{-1}$).

For the wind stress, a temporally variable and spatially uniform wind field was taken from the data of Wolanski (1994) at the Rib Reef weather station ($18^{\circ}28'50''\text{S}$, $146^{\circ}52'12''\text{E}$). Trade winds prevail on the GBR with the long-term mean wind speed of 24 km h^{-1} . This wind condition precedes a short calm weather period (typically from October to December). The calm weather period is later replaced by the monsoonal wind (north-westerly), from the Indian Ocean and southern Asian coastal waters (Wolanski, 1994).

The evaporation rate was assumed to be 0.005 m d^{-1} following Wang et al. (2007). Its value may vary spatially and temporally depending upon air temperature and

humidity, water temperature and wind but this variation is believed to be small in the study area (Wang et al., 2007). The bottom friction was parameterized using a quadratic expression (Lambrechts et al., 2008). The horizontal diffusion coefficient K_h applied to each grid cell was size dependent following Okubo (1971). Okubo's formula applies for open-water and it under-estimates the true value of K_h in the presence of macro-turbulence generated by a complex bathymetry (Wolanski et al., 1984; de Brauwere et al., 2011), thus a factor was used to increase mixing at the sub-grid scale. It resulted in:

$$K_h = f [2.05 \times 10^{-4} \times r^{1.15}] \quad (2.1)$$

where r is the grid size and f is a factor that was set to 2, 20, and 200 in sensitivity analyses.

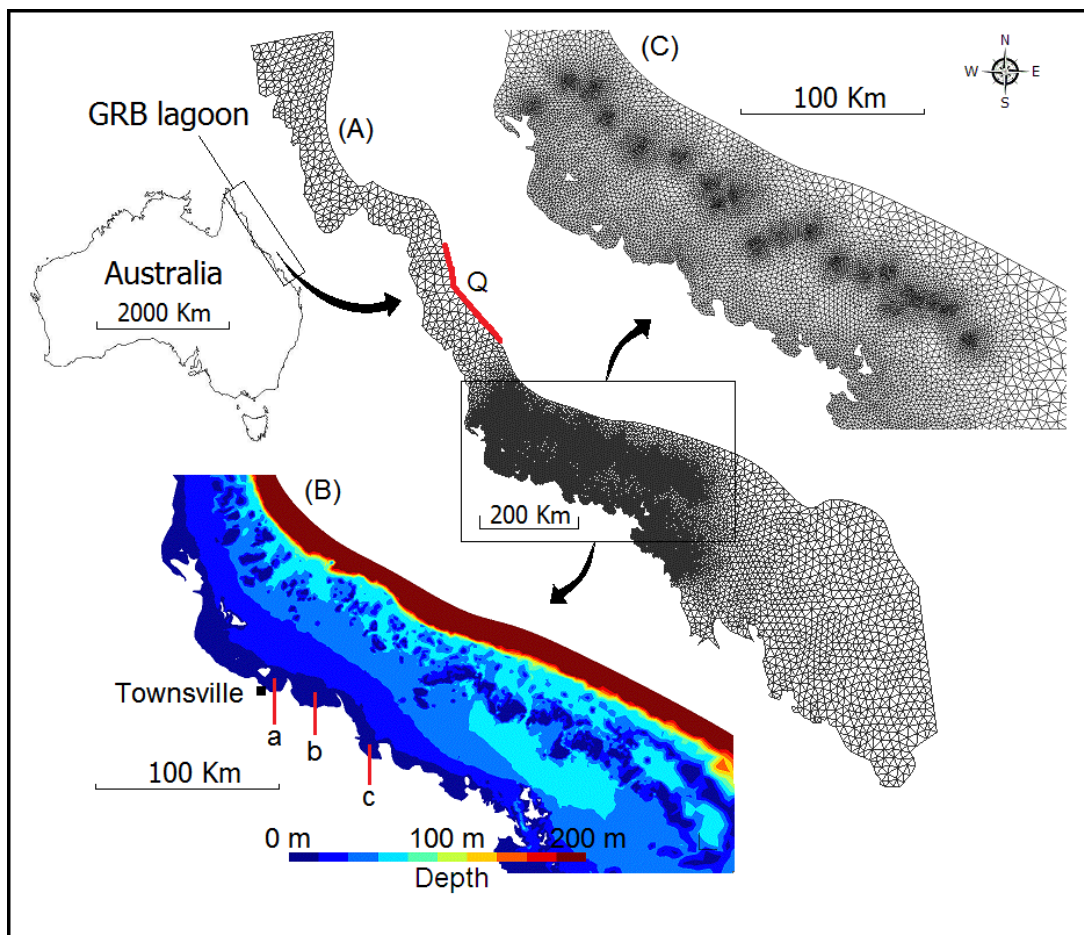


Figure 2.2 – (A) The numerical mesh of the whole GBR, (B) the bathymetry of the high resolution area, and (C) high resolution area of the numerical grid. Q denotes the location of the Coral Sea inflow. a, b and c denote Cleveland Bay, Bowling Green Bay and Upstart Bay, respectively.

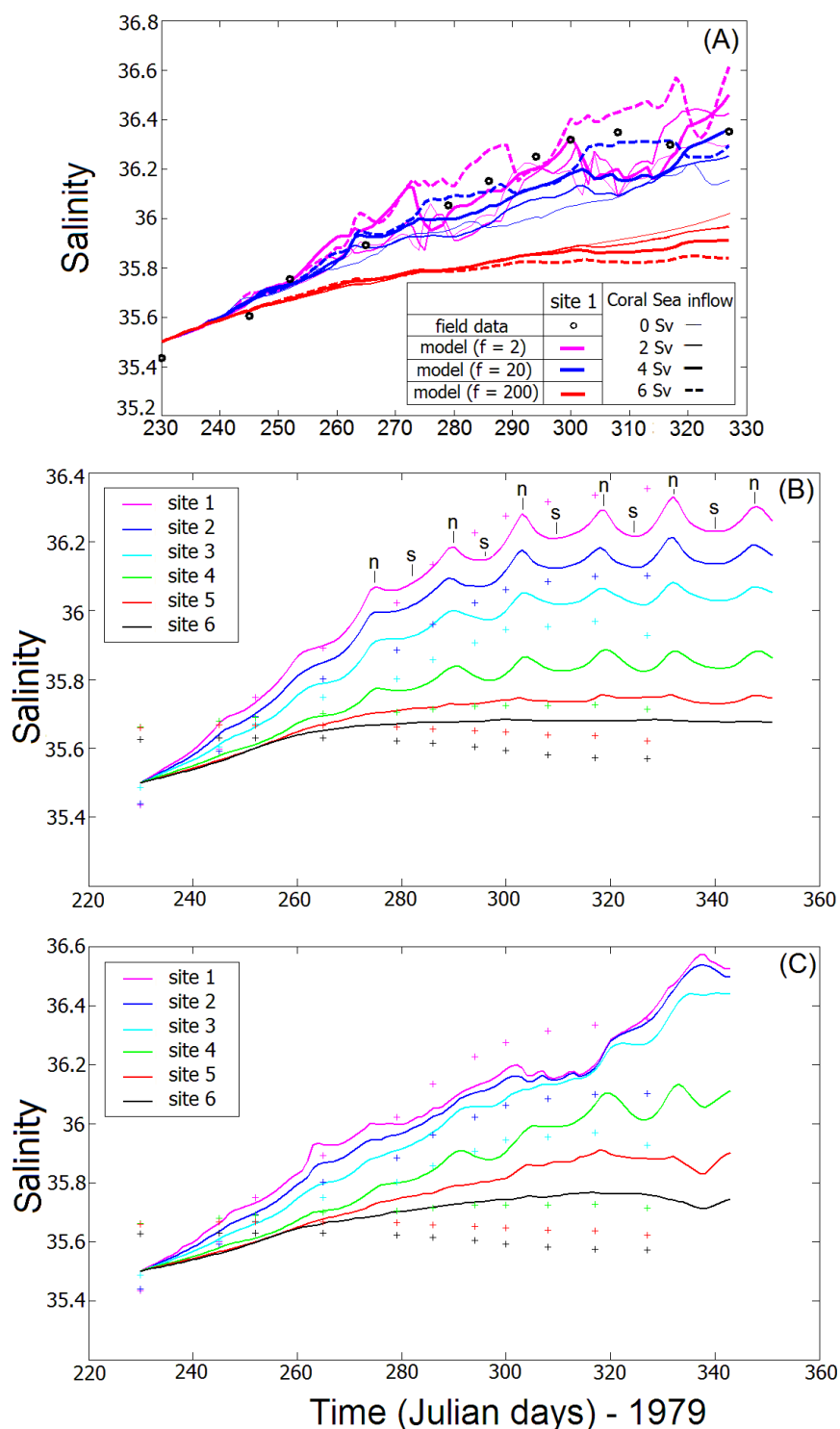
2.3 Results

For the simulation we varied (a) the values of Coral Sea inflow, (b) the horizontal diffusion coefficient K_h , and (c) the wind stress. The tidal currents are mainly cross-shelf in areas of low reef density and long-shelf in areas of high reef density; they are channeled between high reef density zones and the coast especially so offshore from Cape Upstart (Fig. 2.1; Church et al., 1985; Andrews and Bode, 1988; Wolanski, 1994; Spagnol et al., 2001; Lambrechts et al., 2008). Over 95% of the high frequency currents in the GBR lagoon is well represented by the semidiurnal tide components M_2 , N_2 , S_2 and K_2 , and the diurnal components O_1 , P_1 , K_1 (Andrews and Bode, 1988). The ellipses of the predicted tidal currents (not shown) agreed well with the observations of Andrews and Bode (1988).

Table 2.1 shows that the predicted residual currents assuming a Coral Sea inflow of 2 Sv are too small compared to the observations. For an inflow of 6 Sv, the predicted currents are too large. The best agreement in both magnitude and direction was obtained for an inflow of 4 Sv, with the Root Mean Square Error RMSE equal to 0.04 m s^{-1} .

The predicted circulation over the GBR continental shelf reproduces well the results of King and Wolanski (1996), Spagnol et al. (2001), Brinkman et al. (2002) and Luick et al. (2007), the main difference being that, in order to reproduce the observations, the inflow from the Coral Sea needs to be 4 Sv, i.e. twice as large as that previously assumed.

The data on the observed and predicted salinity in coastal waters along the cross-shelf transect are shown in Fig. 2.3. Fig. 2.3A shows temporal salinity changes at site 1 (inshore) for different values for the Coral Sea inflow in the range 0–6 Sv, and different values for the factor (f) from (Eq. (2.1)). From this figure it is apparent that an inflow of ~4–6 Sv is necessary for the model to reproduce the observations. The wind and tides also modulate the hypersalinity. In the absence to wind the model predicts spring-neap tidal fluctuations of the salinity inshore (Fig. 2.3B), with the peaks and troughs of the salinity corresponding to neap and spring conditions respectively. The effect of the trade winds was to increase the salinity at the inshore sites while monsoonal winds decreased the salinity at the inshore sites (Fig. 2.3C). Table 2 shows that the salinity model best fits the salinity data (RMSE from the six sites w 0.1) for an inflow from the Coral Sea of inflow of 4 Sv and the factor $f = 20$ in Eq. (2.1).



Figures 2.3 – Time series-plot of (A) the salinity (psu) at site 1 – inshore – as observed (year 1979) and predicted for different values of the Coral Sea inflow and the factor f in Eq. 1. (B) Observed and predicted salinity without wind at the six sites in the cross-shelf salinity transect, where periods of neap tides (n) and spring tides (s) are indicated. (C) Observed (dots) and predicted (continuous lines) salinity with the variable wind stress.

Table 2.2 – The root mean square error RMSE of the salinity (psu) at sites 1 to 6 (Figure 2.1) for different inflows Q (Sv) of the Coral Sea, and the factor f in Eq. 2.1.

Site location								
	site 1	site 2	site 3	site 4	site 5	site 6	all sites	
Distance from coast (km)	10	15	22	34	46	58	-	
Latitude S	19.1521	19.1121	19.0530	18.9404	18.8590	18.7581	-	
Longitude E	147.0874	147.1089	147.1375	147.1931	147.2337	147.2779	-	
Root mean square error (psu) at sites 1 to 6								
Q	f	site 1	site 2	site 3	site 4	site 5	site 6	all sites
0	0	0.1947	0.1691	0.1565	0.1423	0.1693	0.1727	0.1674
0	20	0.1505	0.1148	0.1212	0.1502	0.1738	0.1477	0.1430
0	200	0.2888	0.1412	0.1708	0.1988	0.1911	0.1507	0.1902
2	0	0.1983	0.1797	0.1546	0.1650	0.1822	0.1844	0.1774
2	20	0.1274	0.1496	0.1647	0.1486	0.1638	0.1756	0.1550
2	200	0.2873	0.1403	0.1713	0.1943	0.1909	0.1912	0.1959
4	0	0.1158	0.1308	0.1549	0.1583	0.1410	0.1024	0.1339
4	20	0.0913	0.0883	0.1063	0.1322	0.1513	0.1207	0.1150
4	200	0.2621	0.1557	0.1285	0.1417	0.1870	0.1846	0.1766
6	0	0.1018	0.2001	0.1704	0.1895	0.1648	0.1498	0.1627
6	20	0.0994	0.0919	0.1431	0.1583	0.1584	0.1146	0.1276
6	200	0.3287	0.1842	0.1194	0.1621	0.1642	0.1558	0.1857

The predicted surface salinity maps of the Central Section of the Great Barrier lagoon are shown at steady state (100th day of simulation) in Fig. 2.4A (with wind) and 2.4B (no wind). The predicted hypersalinity reaches a peak value of 37.5 and the width of the coastal boundary layer of hypersaline waters increases southwards from Cleveland Bay, to Bowling Green Bay to Upstart Bay.

The model performed well in predicting the hypersaline waters in the bays, namely about (36.0–36.6), (36.6–37.0) and (36.6–37.0) in Cleveland Bay, Bowling Green Bay and Upstart Bay respectively; these values agree with observations of Walker, (1981) and Sheaves (2006). The hypersaline waters were not predicted between the latitudes 15 S–17 S (northern area of the domain not comprised in figure 2.4), which is the region where we have applied the Coral Sea inflow Q . This is in agreement with field results of Orr (1933), Brandon (1973) and Pickard (1977). It should also be noted that this region receives higher rainfall than the most of the GBR lagoon which may be the reason that no hypersaline water was measured.

The influence of the application of a southeasterly wind stress is to lower the salinity of bays (Fig. 2.4A) compared with conditions of no wind (Fig. 2.4B). For example, the maximum salinity in Bowling Green Bay and Upstart Bay is 36.5 when wind is considered rising to 36.8 with no wind. The simulation with wind (Fig. 2.4A) also shows hypersaline waters of up to 37 in a 100 km long coastal band from Cleveland Bay to Ingham, while for the simulation with no wind stress (Fig. 2.4B), the highly hypersaline water is confined to Cleveland Bay.

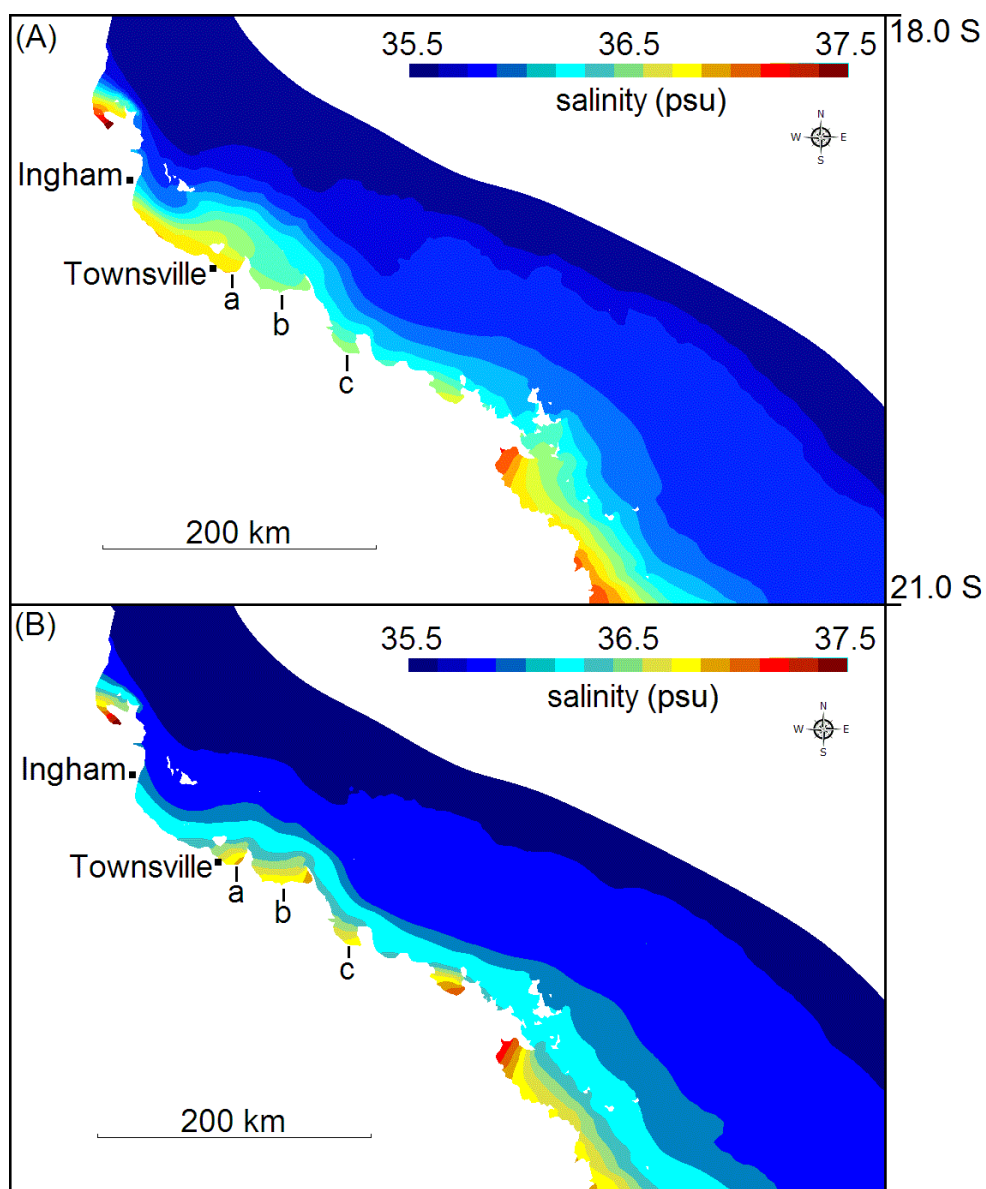


Figure 2.4 – Predicted salinity distribution at steady state (A) in the presence of the wind and (B) assuming no wind. a, b and c denote Cleveland Bay, Bowling Green Bay and Upstart Bay.

2.4 Discussion

The Coral Sea inflow determines the residual currents in the GBR. An inflow of 4 Sv is required to match the observations of residual currents on the GBR continental shelf. This residual circulation combined with tidal mixing determines the time it takes for steady state conditions to prevail. Using $f = 20$, steady state for salinity is achieved after 90 days, while for $f = 2$ it required more than 160 days. For $f = 200$ the steady-state condition was reached much faster (~ 70 days), however, the salinity at the inshore sites did not rise measurably and thus the Coral Sea inflow combined with wind driven currents determine the residual currents in the lagoon.

The results show that the GBR hypersaline zone exists in all wind conditions in the dry season. Hypersaline waters are generated every day and in every bay. Every bay is very shallow (mean depth < 5 m) and drains extensive hypersaline salt flats; salinity in inshore waters of these bays at the mouth of tidal creeks peaks at 37.7 in Bowling Green Bay and 38.7 in Upstart Bay. The residual currents export hypersaline waters from bay to bay longshore southwards; as result the width of the hypersaline zone increases longshore southwards. At the same time, turbulent diffusion spreads the isohalines seawards. The combination of the residual southwards currents with the cross-shelf export of salinity from each bay and turbulent diffusion determines how the width of hypersaline zone increases longshore southwards.

The dynamics of the hypersaline coastal boundary layer in the GBR differs from that in other coastal hypersaline systems in Australia. In Hervey Bay and in Shark Bay (Fig. 2.5) that are relatively shallow systems (average depth < 10 m), vertical mixing inhibits vertical stratification (Nahas et al., 2005; Ribbe, 2006). In those systems the hypersaline waters are trapped in the bay without the possibility of escaping sideways or along the bottom. Similarly, a salinity maximum zone develops in Australian tropical estuaries in the dry season (Wolanski, 1986). A similar long-term trapping of hypersaline waters has been reported for several estuaries and shallow bays world-wide, e.g. the Saloum River Estuary, Tomales Bay, Coorong Lagoon, Gulf of California and Laguna San Ignacio (Diop et al., 1997; Largier et al., 1997; Lavin et al., 1998; Webster, 2010; Winant and de Velasco, in press). In contrast, in Spencer Gulf (Fig. 2.5), which is a deeper near the mouth (50 m), conditions at neap tides result in a vertical stratification of salinity, and the resultant baroclinic circulation allows the hypersaline water to

escape along the seabed (Nunes Vaz et al., 1990). During spring tides, however, the hypersaline water is trapped in Spencer Gulf due to increased tidal mixing ensuring vertical homogeneity and thus preventing a baroclinic circulation to develop. In the GBR different dynamics prevail because the bays are much more open and as a result hypersaline water is exported sideways from bay to bay by a longshore currents as well as cross-shelf by tidal diffusion. This generates a longshore gradient in the hypersalinity. The width of the hypersaline zone in coastal waters is determined by cross-shelf diffusion and the longshore export of hypersaline waters is mainly controlled by advection by the southward residual current due the Coral Sea inflow.

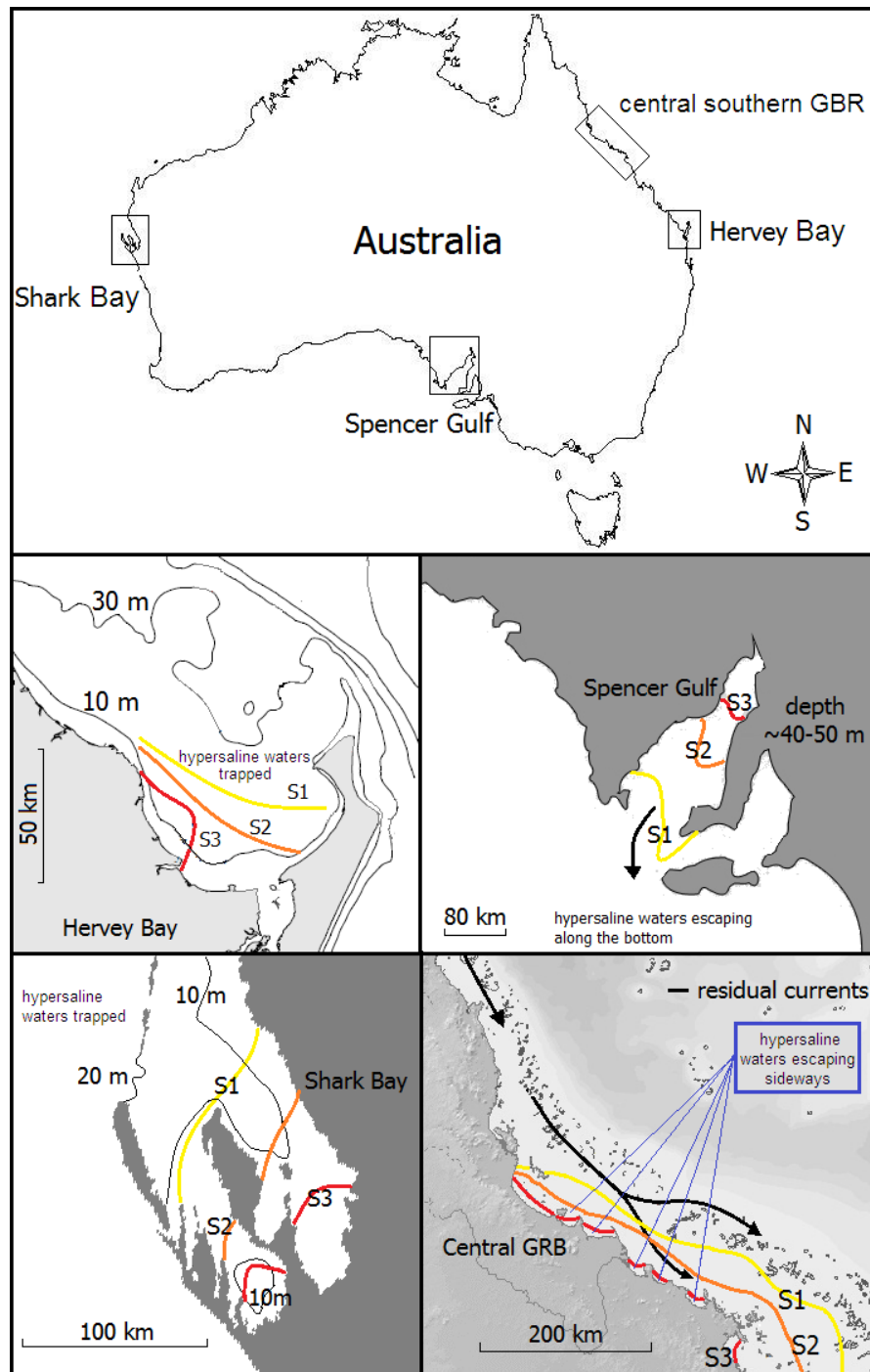


Figure 2.5 – Comparison between hypersalinity systems in Australia. In Spencer Gulf the hypersaline waters may be flushed out along the seabed at neap tides by salinity-driven baroclinic currents. In contrast, the waters in the shallow Hervey and Shark bays are vertically well-mixed, thus the hypersaline waters are trapped. In the shallow GBR the hypersaline waters are transferred sideways from bay to bay by the residual currents and thus forming a coastal boundary layer of hypersaline waters. S1 to S3 indicate the increase of salinity towards inshore areas.

2.5 Conclusions

The inflow of oceanic waters from the Coral Sea, turbulent diffusion and the wind control the dynamics of the GBR hypersaline coastal waters during the dry season. Both the magnitude of the hypersalinity and the time to reach steady-state conditions were used to compare predictions and observations. The model suggests that the cross-shelf salinity gradient was more sensitive to adjustments of the residual current inflow from the Coral Sea than adjustments to the diffusion coefficient K_h . The dynamics of the hypersaline zone are also modulated by the wind and the tides.

The dynamics of the hypersaline coastal zone in the GBR appear different from those in other hypersaline systems in Australia and world-wide. Hypersaline waters in bays along the GBR coast escape sideways by the residual longshore southward currents; hypersaline waters are thus not trapped and are transferred from bay to bay. This demonstrates connectivity between bays. The width of the hypersaline coastal zone increase longshore southwards. The model suggests that steady-state conditions are reached after about 100 days, indicating a long residence time of inshore waters. All these findings may have biological implications that need to be investigated.

Acknowledgements

This study was made possible by the IPRS PhD fellowship to FPA. The kind assistance of J. Lambrechts in the use of the SLIM model is gratefully acknowledged.

CHAPTER 3

Age and the flushing time in the Great Barrier Reef coastal waters

Fernando P. Andutta^{1,2}, Peter V. Ridd¹, Eric Wolanski²

¹ School of Engineering and Physical sciences, James Cook University, Townsville QLD 4811, Australia.

² Centre for Tropical Water and Aquatic Ecosystem Research, James Cook University, Townsville, QLD, 4811, and Australian Institute of Marine Science, Townsville, Australia.

This chapter reproduces the following paper:

Andutta, F.P., Wolanski, E., Ridd, P.V. (Submitted). Age and the flushing time in the Great Barrier Reef coastal waters.

Keywords of this chapter: flushing time, age, Coral Sea inflow, North Caledonian Jet, residual circulation, mixing.

A numerical model of the Great Barrier Reef was verified using currents data from twenty sites and applied to estimate the flushing time and the age of waters. This is the first numerical model applied to the GBR that has been previously calibrated to model accurately mixing processes. These timescales were investigated under different conditions for the wind and inflow from the Coral Sea by the North Caledonia Jet (NCJ). For the whole central GBR, the flushing time was estimated in the range of 1.5 to 9 months under different realistic boundary forcings, while for the bays the flushing time varied between 0.5 and 6 weeks. For the whole central GBR, the flushing time was 67 days under real wind. The effect from the wind and the NCJ inflow was to reduce the flushing time in the bays. In contrast, in coastal waters the wind increases the flushing time because the reversing wind-driven currents transport some water back to the source; this process is comparable to that in an estuary where water that leaves the estuary at ebb tide may return at flood tide, a process parameterized by the return coefficient. For the GBR the return coefficient due to wind reversals may be as large as

60%. The age of waters has shown that the NCJ inflow in the GBR requires over 5 months to exit the GBR under calm weather, and over 7 months under southeasterly winds. In the south and central regions of the GBR, the southeasterly wind was observed to deflect seaward away from the inner shelf and towards the outer shelf the southward flowing NCJ inflow, making room for a wind-driven current of opposite direction on the inner shelf. Thus the intrusion of oceanic water in the GBR depends on the wind over the GBR.

3.1 Introduction

The transport time scales of water in an aquatic environment has long been of interest to biological oceanographers because it is an important parameter to determine the estuarine ecosystem health as well as its sensitivity to pollution threats (Lucas et al., 2009; McLusky and Elliott, 2004; Wolanski, 2007; Wolanski, et al., 2012). Physical oceanographers have provided a number of definitions of transport time scales. The flushing time is defined as the time necessary for a concentration to decrease to $1/e$ (~ 0.37) of its initial concentration (Ketchum, 1950; Dyer, 1973; Deleersnijder et al., 2006). Flushing time is an integrative parameter used to describe the water body exchange without identifying the mass concentration distribution in the domain (Monsen et al., 2002; Valle-Levinson, 2010). To incorporate this spatial distribution there is the definition of residence time, which is the time necessary for a water particle to initially exit a domain; thus the residence time depends on the release location and time (Monsen et al., 2002). For the residence time definition, once water particles have crossed the first time one of the domains open boundaries, those particles are assumed never to return. In practice however some of those particles may return with reversing tidal currents in an estuary, or return by other physical mechanisms in different aquatic systems (Monsen et al., 2002). To account for the excess time for water particles re-entering a specific domain, the exposure time is used. The exposure time is the total time that a parcel of water spend inside the estuary, this time accounts for the period in which water parcels re-enter the estuary (Delhez, 2006). The age is the time necessary for a water parcel to move from a defined inlet boundary to another specific location (e.g. the mouth of an estuary); thus particles released at different boundary locations show different ages (Monsen et al., 2002). The return coefficient, a non-dimensional

parameter, is used to quantify the propensity of particles to return into a pre-defined domain after crossed the first time one of its open boundaries. This coefficient is defined as the ratio of the difference between the exposure time and the residence time to the exposure time, and its value ranges between 0 and 1. The return coefficient is close to unity for areas where water particles have a higher propensity to re-enter the domain, and is zero for areas where particles never re-enter the domain after having first crossed one of its open boundaries (Arega et al., 2008; de Brauwere et al., 2011).

It is not possible to estimate adequately those time scales for the Great Barrier Reef of Australia (GBR; Figure 3.1) using physical tracers, because such data are unavailable. An alternative approach is to use numerical models by tracking hundreds to thousands of virtual tracers (Wolanski, 2007).

This paper uses the high-resolution, non-structured, numerical model (Lambrechts et al., 2008, Andutta et al., 2011, Andutta et al., 2012) to estimate the transport timescales namely, flushing time and the age of waters in the Great Barrier Reef. The mesh size was calculated as a function of distance from coastal line and bathymetry. Cells of a few hundred meters were used near reefs, islands and the coast, and cells of a few kilometers were used in deeper regions far from the coast and the central GBR. This use of variable dimension cells allows for the appropriate representation of the high velocity shear zones close to reefs and wakes of islands, and also of the tidal jets between narrow passages.

The SLIM 2D vertical integrated model can be used to represent the hydrodynamics within the GBR, because baroclinic circulation due to salinity stratification is confined to short periods of relatively large river discharges in the coastal zone (Wolanski and van Senden, 1983), and upwelling events at the shelf break (Andrews and Furnas, 1986). This is the first numerical model applied to the GBR that has been previously calibrated to model accurately mixing processes. This calibration was achieved by comparing model results with measurements of salinity during the dry season, i.e. measurements of hypersaline coastal waters in the GBR (Andutta et al., 2011). The problem of using 3D models with low horizontal resolution as opposed to 2D vertical integrated models with high horizontal resolution was addressed by Luick et al. (2007) who showed that 3-D models may not be needed because little vertical stratification of salinity and temperature was found in most areas, aside from river

mouths and then only during the short-lived wet season, and thus the local baroclinic circulation was negligible.

In this paper these estimates were re-calculated to take into account of a process so far neglected in the GBR, namely the wind-driven return flows that can return particles to the source. The return coefficient is seldom larger than 60% over the time scale of a wind event because the wind also deflects seaward toward the outer shelf the oceanic waters intruding on the shelf, making room for a wind-driven of opposite direction on the inner shelf. The GBR can thus be viewed as a giant estuary where the ‘river’ is the oceanic inflow from the Coral Sea, the buoyancy effects are negligible, and where the tides are important to generate mixing, and the wind generates flow reversals resulting in a return coefficient that inhibits flushing of the GBR. The age of the inflow is as large as 7 months on leaving the GBR.

3.2 Methods

The SLIM model

The numerical model has being already described in sub-section 2.2 (Andutta et al., 2011). Different from the mesh configuration applied by (Andutta, et al., 2011), the present study used a higher horizontal resolution (Figure 3.1B), e.g. for the reef matrix. The model uses grid cells in the range of 150 m near reefs to nearly 20 km in open waters far from reefs (Figure 3.1B).

The model reproduces well (Andutta et al., 2011) the observations of a mean southward current at Myrmidon Reef and at Old Reef and Cape Upstart (Figure 3.1), except during southeasterly winds (Burrage et al., 1997; Andrews, 1983), of tidal currents oriented across the shelf in the central region of the GBR and longshore in the southern region (Church et al., 1985) and that the residual southward flow splits into two branches as it approaches the high reef density area (Figure 3.1C), one branch channelled between the reef matrix and the coast, and the other beside the reef matrix out from the GBR (Brinkman et al., 2001).

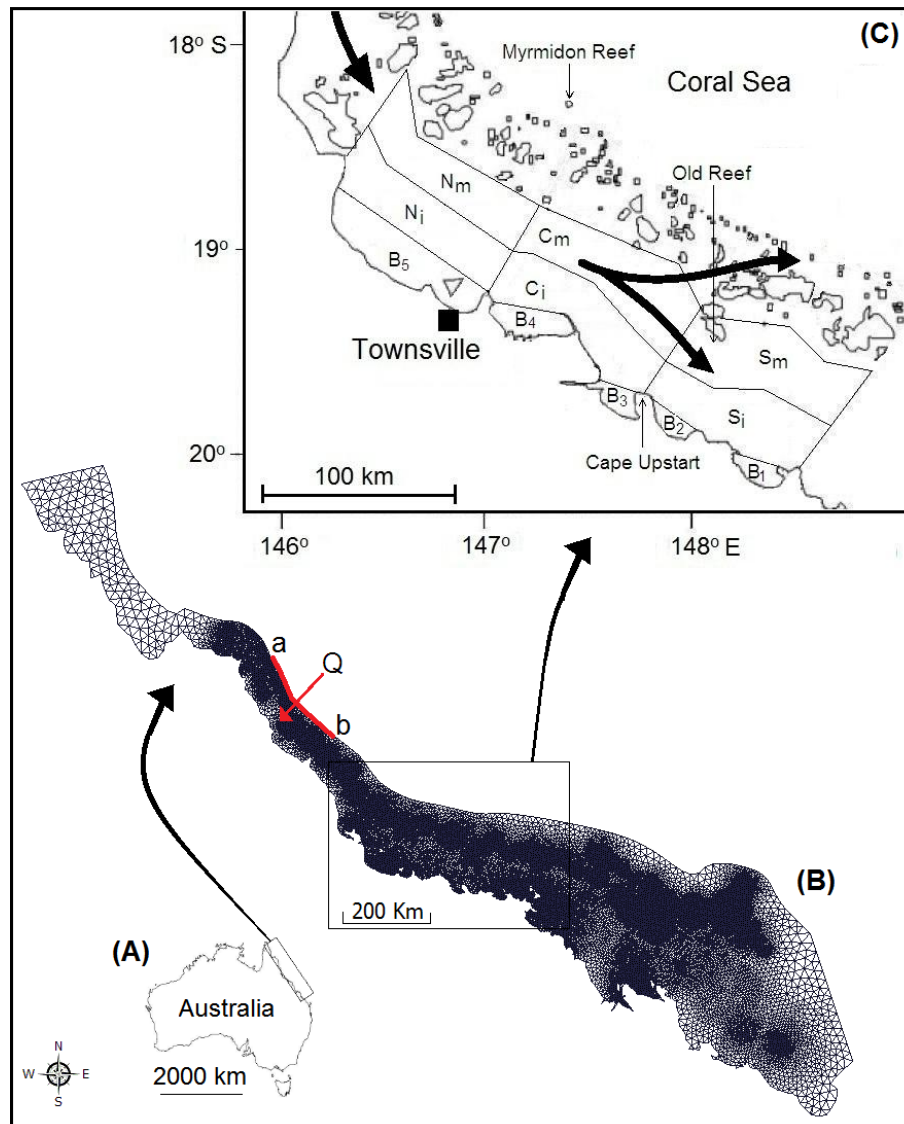


Figure 3.1 – (A) Map of Australia indicating the GBR location, (B) the numerical grid of the whole Great Barrier Reef with the resolution from about 150 m to 22 km, and location of the Coral Sea inflow Q (between a and b) used in the simulation. (C) The central section of the Great Barrier Reef lagoon, located north-eastern Australia. The mean flushing time was estimated for the bays B_1 - B_5 , and the (S_i) South inshore, (S_m) South middle zone, (C_i) Central inshore, (C_m) Central middle zone, (N_i) North inshore and (N_m) North middle zone. The arrows indicate the residual currents.

The estimates of flushing time and age were made using a Lagrangian scheme that avoids negative diffusion effects near sloping boundaries (Spagnol et al., 2002), using up to 300,000 virtual drifters. To estimate the age of the NCJ inflow, the virtual drifters were released at the open boundary (Q), which is where the NCJ inflow enters the GBR (Figure 3.1B). To estimate the flushing time the drifters were released in the study areas shown in Figure 3.1A and labeled B (bays), N (North), C (central) and S (South); these domains include 5 bays, 3 inshore regions and 3 mid-shelf regions with alongshore and cross shelf dimension of 100 km by 30 km, respectively.

The open boundary forcing

Five different boundary conditions have been considered (Table 3.1). The real wind field was from Australian Institute of Marine Sciences (AIMS), collected at the Rib Reef weather station (18°28'50''S, 146°52'12'' E), and the simulations under real wind conditions starting at 1st of August 2006 (Andutta et al., 2011). The wind stress was assumed to be only spatially uniform. Sea level data from TOPEX was used to force tides at the open boundaries.

The inflow Q from the Coral Sea by the NCJ was modeled following Andutta et al (2011); Q was set to either 0 Sv or 4 Sv ($1 \text{ Sv} = 10^6 \text{ m}^3 \text{ s}^{-1}$) and was applied to the open boundary, between $\sim 16.3^\circ \text{ S}$ and 17.4° S (Figure 3.1B). The southern open boundary was forced to drain the flow volume of $0.7 \times Q$, while on the northern GBR the open boundary was forced to drain the other $0.3 \times Q$.

Table 3.1 – Five boundaries conditions applied to the numerical simulations to estimate the flushing time and the age of waters in the Great Barrier Reef.

Condition	Description of the boundary forcing assumed
C ₁	Calm weather (i.e. no wind), zero Coral Sea inflow ($Q = 0$).
C ₂	Calm weather, Coral Sea inflow $Q = 4 \text{ Sv}$.
C ₃	Fluctuating southeasterly wind of 6.67 m s^{-1} (i.e. moderate wind) occurring in bursts of 10 days followed by 20 days of calm weather; Coral Sea inflow $Q = 4 \text{ Sv}$.
C ₄	Fluctuating southeasterly wind of 10 m s^{-1} (strong wind) occurring in bursts of 10 days followed by 20 days of calm weather; Coral Sea inflow $Q = 4 \text{ Sv}$.
C ₅	Real wind conditions; Coral Sea inflow $Q = 4 \text{ Sv}$. The real wind simulation starts on 1 st of August 2006.

The physical parameters

High values of the Manning roughness coefficients were used over the reef zones ($2.5 \times 10^{-1} \text{ m}^{-1/3}\text{s}$) and lower values ($2.5 \times 10^{-3} \text{ m}^{-1/3}\text{s}$) elsewhere.

The bottom friction stress (τ) inside the GBR was parameterized using

$$\tau = \frac{g}{C^2 H} \|u\|, u, \quad (3.1)$$

Where C , $[C] = \text{m}^{1/2}\text{s}^{-1}$, is the Chezy roughness coefficient and H the local water depth.

The Chezy coefficient calculated with $C = H^{\frac{1}{6}} n^{-1}$, with n denoting the Manning coefficient.

The eddy viscosity parameterization was used to solve diffusion of momentum to the sub grid scale (Smagorinsky, 1963). The coefficient for the horizontal diffusion of mass, K_h , is assumed to be a function of the mesh size, thus constant in time. A modification of the empirical formula from (Okubo, 1971) was used to solve the macro-turbulence generated by a complex bathymetry, i.e.

$$K_h = f [2.05 \times 10^{-4} \times r^{1.15}] \quad (3.2)$$

where r is the length scale which here is assumed to be the grid resolution and f was a factor that has been introduced to the formula of Okubo (1971), and was found to be equal to 20 in order for the model to fit field observations of the GBR coastal hypersaline zone during the dry season (Andutta et al., 2011).

Table 3.2 – Observed (U_o) and predicted (U_p) longshore residual currents in a range for conditions (C_2) under calm weather, (C_3) fluctuating wind of 6.67 m s^{-1} , (C_4) fluctuating wind of 10 m s^{-1} and (C_5) for a real wind condition (>0 if northward, <0 if southward) and peak tidal currents (U_T) at mooring sites. The wind condition does not affect the tidal currents, and thus U_T does not change. Data from the table extracted from Andutta et al. (2011) and Andutta et al. (pers. comm.). The root mean square error for velocity RMSE (m s^{-1}).

Currents (m s^{-1}) in the GBR at mooring sites								
Site name	Lat. ($^{\circ}\text{S}$)	Lon. ($^{\circ}\text{E}$)	U_o	$U_p(C_2)$	$U_p(C_3)$	$U_p(C_4)$	$U_p(C_5)$	U_T
Lizard Island	14.7406	145.4253	0.05	0.06	0.07	0.08	0.07	0.23
Cape Upstart	19.6253	147.9142	-0.11	-0.12	-0.10	-0.09	-0.10	0.63
Old Reef	19.4071	148.0197	-0.10	-0.11	-0.09	-0.08	-0.09	0.59
near shelf break	18.8311	148.2896	-0.25	-0.19	-0.23	-0.25	-0.20	0.36
Myrmidon Reef	18.2452	147.4100	-0.18	-0.20	-0.21	-0.24	-0.25	0.52
Bowden Reef	19.0600	147.9597	-0.02	-0.03	-0.02	-0.01	-0.02	0.47
Rattray Island	19.9826	148.5833	-0.08	-0.10	-0.09	-0.08	-0.09	0.47
Hook	19.9400	149.1100	-0.15	-0.17	-0.16	-0.15	-0.16	0.71
Bushy	20.8900	150.1600	-0.13	-0.15	-0.12	-0.12	-0.13	0.32
Bell	21.8200	151.1400	-0.06	-0.08	-0.06	-0.05	-0.06	0.45
RMSE	-	-	-	0.025	0.022	0.024	0.028	-

The flushing time, the return coefficient and age simulations

Because of the large number of lagrangian particles used in each location, we have assumed the residence time to be the time for 63% of the particles to exist firstly the domain, and similarly for the exposure time (Deleersnijder et al., 2001). This was implemented by applying an initial concentration of lagrangian drifters in the region of interest, and with zero drifters in all other areas. We have used 3×10^5 virtual lagrangian particles inside the 100 km by 30 km areas, and for the bays 10^3 particles per km^2 . The size of those inshore and mid-shelf regions was not smaller because tidal mixing would

result in a flushing time too short to be analyzed. The size of those regions was not larger because we intended to show the patchiness for the flushing time in the GBR, and thus to show the potential deficiency of the 1D models (Hancock et al., 2006; Wang et al., 2007). The mean concentration value is computed inside each area according to the number of particles remaining in the sub-domains, and the timescales were calculated for conditions C_1 to C_5 (Table 3.1).

The return coefficient was estimated for the coastal areas and the bays in the GBR, and the formulation to estimate the age is described in details by Arega et al., (2008) and de Brauwere et al., (2010). This coefficient was calculated for conditions C_3 , C_4 and C_5 using the following equations,

$$r(C_3) = \frac{\phi(C_3) - \varphi(C_3)}{\phi(C_3)}; \quad r(C_4) = \frac{\phi(C_4) - \varphi(C_4)}{\phi(C_4)}; \quad r(C_5) = \frac{\phi(C_5) - \varphi(C_5)}{\phi(C_5)}, \quad (3.3)$$

where r , ϕ and φ are the return coefficient, exposure time and residence time, respectively. The return coefficient for conditions (C_1) and (C_2) was negligible because under calm weather a negligible fraction of the total particles number returned to its source by the reversal tidal currents.

For the age estimates we assumed the Coral Sea inflow ($Q = 4 \text{ Sv}$) for conditions C_2 to C_5 (Table 3.1). The age was computed as the elapsed time of particles deployed initially at the boundary where NCJ (Figure 3.1); the contours of the age were computed similar to Shen and Hass (2004). Unlike the flushing time simulations, for the age we considered four different conditions based on the wind stress. To help the interpretation of the age of waters in coastal areas, we have released 10 thousand particles in coastal waters near Townsville (19° S , 147° E), and thus quantifying the alongshore travel distance in time under different wind conditions.

3.3 Results

Results of the model performance are shown in Table 3.2, where the Root Mean Square Error RMSE was calculated for the simulated velocity. Under the different conditions applied to the wind the residual currents were well simulated by the numerical model. The prediction of the salinity in the dry season was also well simulated and thus there is confidence that mixing and exchange processes within the

domain were well simulated by the numerical model. Tidal currents were also well simulated (Andutta et al., 2011).

Flushing time and return coefficient

The flushing time T was estimated for the three inshore and mid-shelf areas, and for bays 1 to 5 (Table 3.3). In addition, in this table is shown the percentage of a conservative concentration in those areas after 12 and 24 days. The conservative concentration decay in time for those sites is presented in (Figure 3.2) for conditions (C₂) and (C₄).

The flushing time for condition (C₂) is in the order of 0.5–1.5 weeks for the inshore and mid-shelf areas, and in the order of 0.5–3 weeks for the bays 1 to 5 (Figure 3.2B). For conditions (C₃) and (C₄), the flushing time T increased in inshore and mid-shelf areas while it decreased in the bays (Table 3.3, and Figure 3.2). For condition (C₃) T was calculated in the order of 0.5–3 weeks (inshore and mid-shelf areas), and 0.5–2 weeks (in the bays). While for (C₄), T was calculated in the order of 0.5–4.0 weeks (inshore and mid-shelf areas) and 0.5–2 weeks (in the bays). The flushing time in the bays were slightly lower for the (C₄) than for (C₃); however, slightly smaller for inshore and mid-shelf areas for (C₃).

The return coefficient was calculated for those inshore and mid-shelf areas, which indicates the propensity of particles to return to their source (Table 3.3). For conditions (C₁) and (C₂) the return coefficient was close to zero. In contrast, for (C₃) and (C₄) the largest return coefficients were calculated for the southern (S_i and S_m) and northern areas (N_i and N_m), although in the central mid-shelf area (C_i) this coefficient was relatively large, $r \sim 0.60$. For condition (C₅), the results were similar to (C₂), aside from the results in areas B5 and S_i, where the flushing time has nearly doubled under condition (C₅).

The flushing time for $Q = 0$ and zero wind (C₁) is in the order of 5–8.5 weeks in the six coastal zones and in the order of 1–6 in the bays (Table 3.3). C₁ resulted in the largest time of flushing because tidal mixing becomes the only important remaining mixing mechanism for these conditions. The effect in the bays of applying the southeasterly wind of 6.67 m s^{-1} and 10 m s^{-1} is to reduce the flushing times (Table 3.3), because alongshore wind-driven residual currents inhibit water particles to return to its source bay (Figure 3.2).

For the whole central GBR the flushing times vary from 1 to 9 months (Table 3.3). Results were ~ 6.5 weeks for (C_2). For conditions (C_3) and (C_4), the flushing T was estimated in ~ 12 and ~ 15 weeks, respectively. The largest flushing time of ~ 9 months was obtained for (F_1), i.e. calm weather with no inflow Q . For the real wind C_5 , the flushing time in the central GBR was ~ 9.5 weeks.

Table 3.3 – The average flushing time T (in days) and the concentration of a passive tracer (in %) remaining after 12 and 24 days. The results are for the simulations assuming conditions (C_1), (C_2), (C_3), (C_4) and (C_5). Results are for the bays B1-B5, and the zones (S_i) South inshore, (S_m) South middle, (C_i) Central inshore, (C_m) Central middle, (N_i) North inshore and (N_m) North middle (Fig. 3.1). Central GBR rows show the flushing time for all the zones and bays. The return coefficient r calculated for conditions C_1 and C_2 was nearly zero, while for conditions C_3 , C_4 and C_5 is shown in the table.

Two conditions of inflow Q , under calm weather condition									
Location	$(C_1) Q = 0 \text{ Sv}$				$(C_2) Q = 4 \text{ Sv}$				
	T	N_1 (12 d)	N_2 (24 d)	T	N_1 (12 d)	N_2 (24 d)			
B ₁	21.0	53.0	34.0	20.0	52.4	33.0			
B ₂	6.0	21.6	10.2	3.0	5.0	17.5			
B ₃	18.5	47.4	29.6	9.5	34.1	0.0			
B ₄	18.5	46.8	29.2	14.0	40.7	19.2			
B ₅	41.0	66.6	53.0	18.0	53.5	27.0			
S_i	60.0	81.0	69.9	5.5	16.7	0.0			
S_m	42.5	67.2	54.1	10.0	30.9	13.6			
C_i	37.0	62.9	48.4	8.5	28.8	9.4			
C_m	37.0	63.5	49.3	5.0	6.1	0.0			
N_i	35.0	56.8	42.9	8.0	28.8	13.0			
N_m	37.0	61.3	49.1	11.0	35.6	16.8			
central GBR	270	92.0	88.0	43.0	74.0	56.0			
Two conditions of fluctuating southeasterly wind, and the Coral Sea inflow of 4 Sv									
Location	(C_3) Wind 6.67 m s^{-1}				(C_4) Wind 10 m s^{-1}				
	T	r	N_1 (12 d)	N_2 (24 d)	T	r	N_1 (12 d)	N_2 (24 d)	
B ₁	14.0	-	47.1	6.8	13.4	-	43.0	2.5	
B ₂	2.7	-	0.0	0.0	2.7	-	0.0	0.0	
B ₃	10.0	-	28.5	0.0	10.0	-	26.1	0.0	
B ₄	12.5	-	38.8	1.6	11.7	-	35.2	0.0	
B ₅	15.0	-	49.2	11.0	14.0	-	45.8	1.4	
S_i	5.8	0.05	24.1	15.4	20.7	0.74	26.3	25.2	
S_m	22.9	0.56	38.8	35.1	26.1	0.62	38.9	42.5	
C_i	21.8	0.61	36.0	31.5	23.1	0.63	35.8	35.1	
C_m	5.0	0.00	11.0	8.0	5.0	0.00	10.7	2.0	
N_i	21.4	0.63	34.5	31.1	22.6	0.65	34.6	32.4	
N_m	22.0	0.50	38.8	32.8	25.0	0.56	39.5	40.0	
central GBR	86.0	0.50	76.6	76.9	100	0.57	78.4	86.2	
(C_5) real wind, and the Coral Sea inflow of 4 Sv									
Location	T	r	N_1 (12 d)	N_2 (24 d)	Location	T	r	N_1 (12 d)	N_2 (24 d)
B ₁	20.4	0.05	57.3	33.4	S_i	11.5	0.52	36.5	11.7
B ₂	3.8	0.22	14.0	3.6	S_m	10.4	0.04	33.2	6.1
B ₃	11.2	0.15	35.3	18.1	C_i	13.1	0.35	38.8	17.2
B ₄	10.7	-	32.7	18.0	C_m	5.1	0.02	11.1	0.0
B ₅	30	0.40	63.4	46.3	N_i	9.9	0.19	34.3	17.0
central GBR	67.0	0.36	87.0	69.0	N_m	10.8	-	34.2	9.9

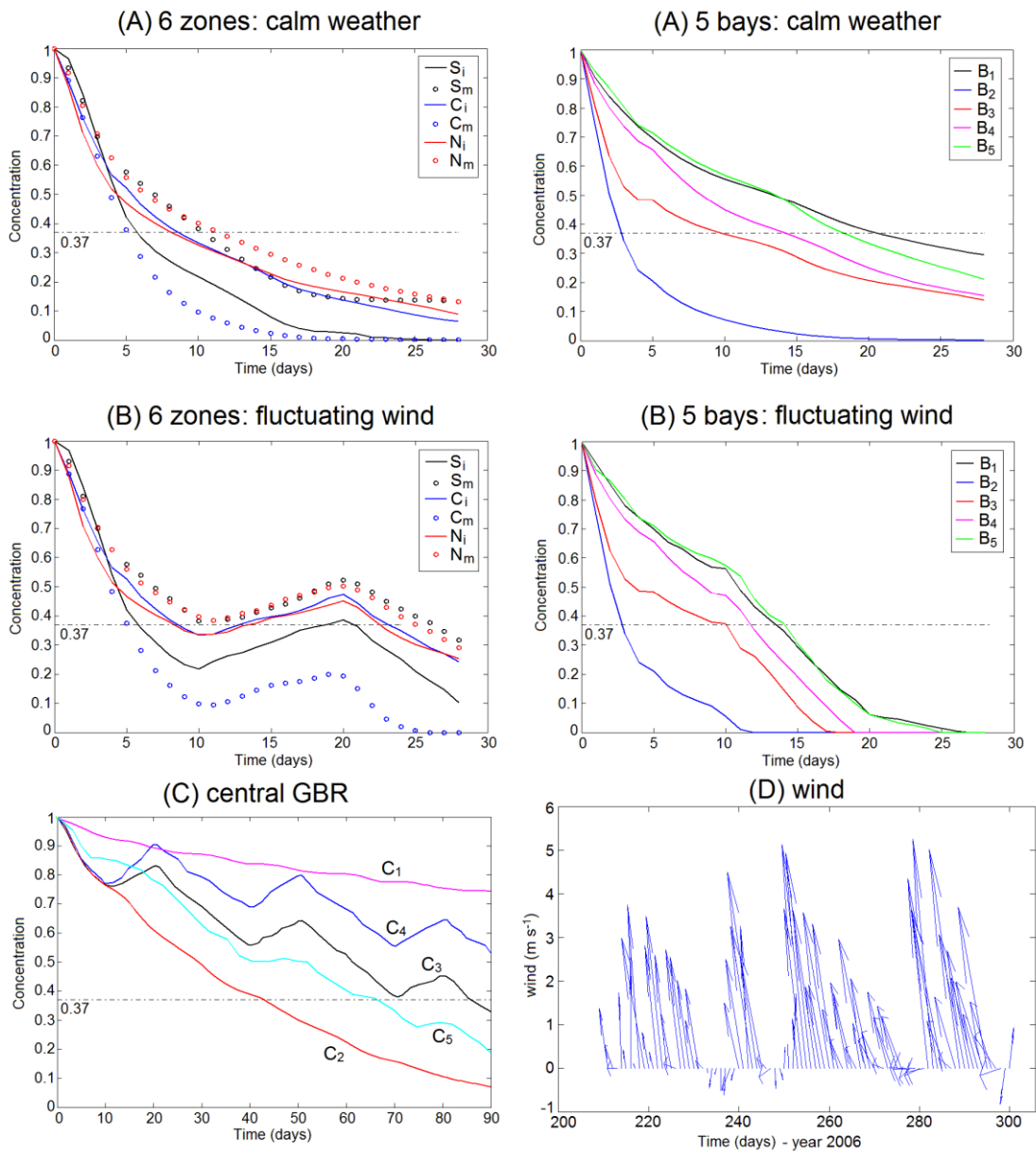


Figure 3.2 – The flushing time (A) for conditions C_2 and (B) for condition C_4 , shown for the first month of simulation. Results shown in (A) and (B) are for the bays B_1 - B_5 , and the zones (S_i) South inshore, (S_m) South middle, (C_i) Central inshore, (C_m) Central middle, (N_i) North inshore and (N_m) North middle (Fig. 3.1). (C) is the flushing time for the whole Central GBR, i.e. the 6 zones + 5 bays, which is shown for the first 3 months of simulation under conditions C_1 , C_2 , C_3 , C_4 C_5 . (D) is the daily averaged real wind measured at Rib Reef weather station ($18^{\circ}28'50''\text{S}$, $146^{\circ}52'12''\text{E}$) starting on 1st of August 2006. All results from the different conditions are summarized in Table 3.2.

Under calm weather, and changing the inflow from 0 Sv to 4 Sv resulted in a 3.5 to 10 fold reduction in the flushing times (for no wind conditions) for the inshore and mid-shelf zones. S_i showed the most dramatic reduction (from 60 to 5.5 days) which was due to the Coral Sea inflow (Table 3.3). For the bays, the influence of the Coral Sea inflow was also to reduce T , because the alongshore transport of particles inhibited the reversal tidal currents to transport those particles back into the bays, i.e. negligible return coefficient.

Age

Figure 3.3A shows the alongshore transport of particles deployed at coastal waters near Townsville (Figure 3.1C). Results for the zero wind condition (C_2) show that water particles moved southward (Figure 3.3A), and for the period of three months those particles travelled southwards a distance of ~ 350 km. In contrast, when a fluctuating southeasterly wind is applied (C_3 and C_4) for short periods, those water particles moved back and forth near the coast and thus the southward net transport was reduced (Figure 3.3A). After nearly three months those particles released at coastal waters near Townsville had travelled southwards a distance of ~ 170 km and ~ 40 km for conditions (C_3) and (C_4), respectively. For the real wind C_5 , the particles were transported southwards, but slower than for a calm weather condition (Figure 3.3A).

For zero wind shown in Figure 3.3B, under condition (C_2), the southward flow is fast near the shelf break with water particles exiting the domain in the southern GBR in less than 2 months. While the water that entered the GBR lagoon took over 5 months to travel along the central and southern GBR in coastal areas. Over the high reef density areas the bottom friction reduced residual currents and thus reduces the local water renewal by the coming inflow. For conditions under calm weather (Figure 3.3B) and the real wind (Figure 3.3E), the age of waters show the NCJ inflow splitting around the high reef density matrix into two branches, indicating high retention time of water in the reef matrix. This effect of high reef density areas steering the flow around and decreasing water renewal within these areas was defined as the sticky water effect (Wolanski, 1994).

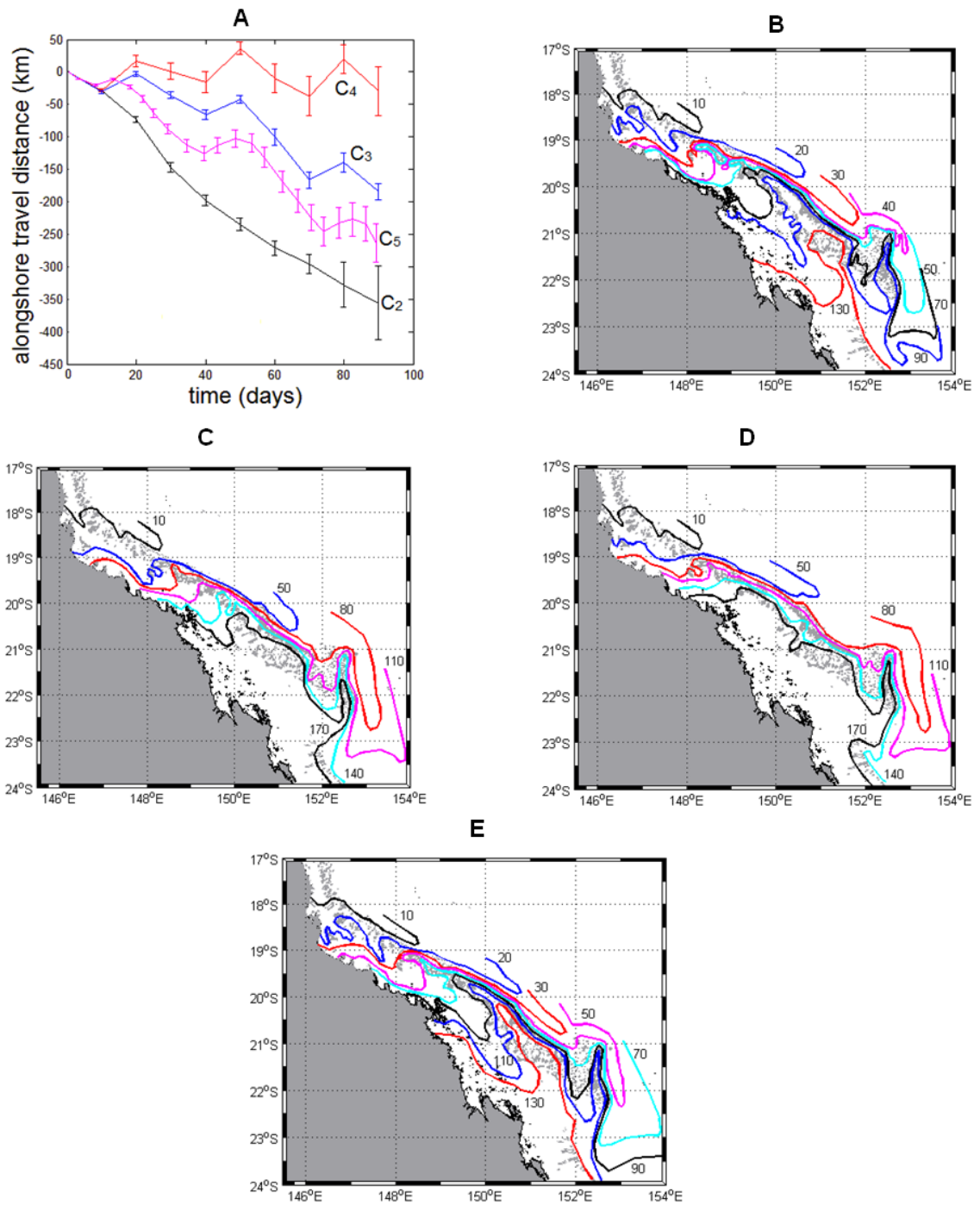


Figure 3.3 – (A) Alongshore travel distance of particles deployed initially at $(19^\circ \text{ S}, 147^\circ \text{ E})$, location near Townsville in inshore waters in the zone N_1 (see figure 3.1). For conditions C₂ to C₅. Age of the NCJ inflow in days is shown for conditions C₂ (B), C₃ (C), C₄ (D), and C₅ (E).

Conditions C_3 and C_4 (Figures 3.3C and 3.3D) indicate a reduced transport of particles between the reef and the coast due to the reversal generally southerly current caused by the Southeasterly wind. This northward wind driven water intrusion inhibited a fraction the Coral Sea inflow to cross between the reef matrix and the coast in the Southern GBR, thus forming a coastal boundary layer. Water particles were transported back and forth near the coast, while spreading cross-shelf. A small fraction of particles crossed the reef matrix towards the shelf-break and were then quickly transported southwards outside the lagoon by the EAC with speed of, *ca.* 0.20 to 0.30 m s⁻¹. For the condition (C_4) (Figure 3.3D), most of water particles did not flow southwards between the reef matrix and the coast in the southern GBR, i.e. between 20° S and 23° S. These results show a trapped water mass forming a coastal boundary layer (Figures 3.3C and 3.3D). For the real wind condition (C_5), the NCJ inflow was not deflected from the coastal areas, because the southeasterly wind for that period was not strong.

A conceptual model summarizing the results of the age of waters is shown in Figures 3A and 3B. For calm weather condition (Figure 3.4A), a large fraction of the NCJ inflow moves southwards among the reefs and the coast, and thus reducing water trapping in coastal areas. This is evidenced by the MODIS satellite image (Figure 3.4C). In contrast, under southeasterly wind, there is reduced flushing of inshore water; the wind not only deflects a larger fraction of the NCJ inflow to the outer GBR, it also generates a wind driven current of opposite direction in coastal areas (Figure 3.4B). This is evidenced by the MODIS satellite (Figure 3.4D), where a turbulent nearshore zone was observed with its width increasing southwards. This turbulent zone evidenced that new oceanic inflow in the GBR was deflected seaward. A similar process of the wind preventing oceanic inflow unto a continental shelf has been observed in other systems (Haley Jr. and Lermusiaux, 2010; Ramp et al., 2011).

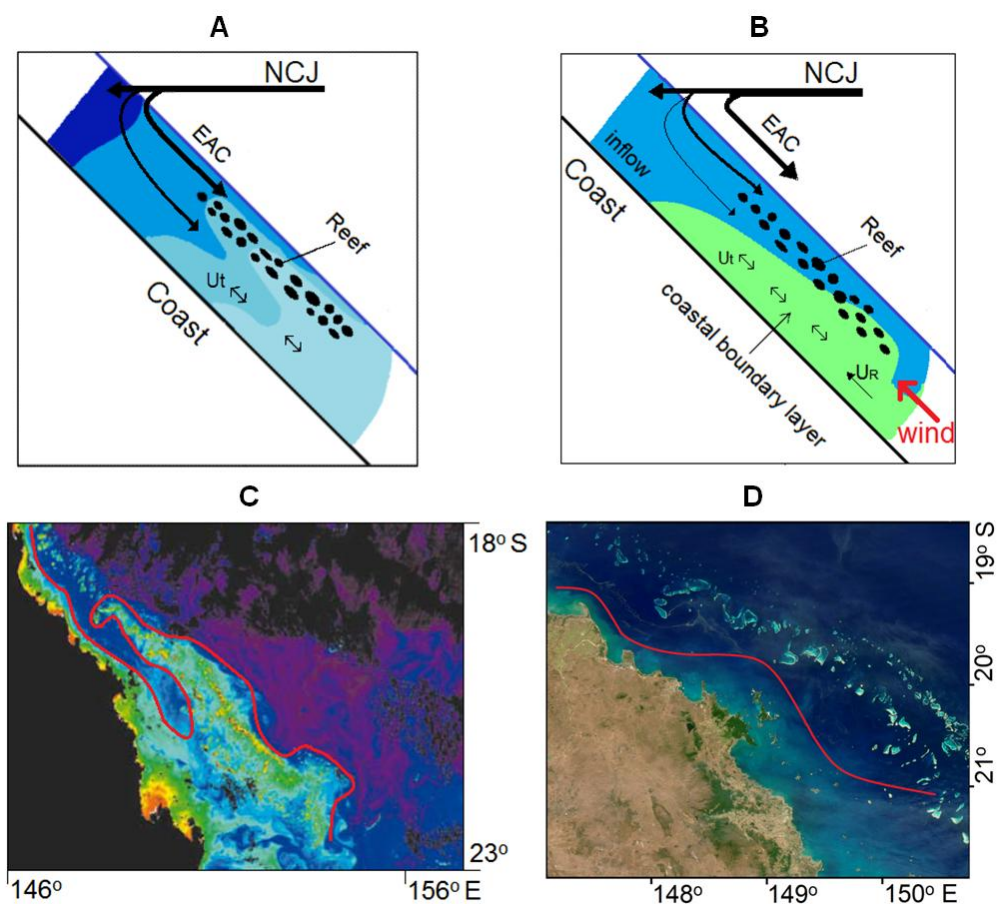


Figure 3.4 – (A) Model description of the age from the Coral Sea inflow under an idealized condition of long term calm weather. Age shows faster water renewal in the outer GRB than for areas over reefs and between the reef matrix and the coast. High reef density areas waters are poorly renewed. U_t denotes the direction of tidal current between high reef density areas and the coast, and U_R the residual velocity. (B) Conceptual model describing long term trapped water forming a coastal boundary layer increasing width southwards. The coastal water trapping is caused by fluctuating southeasterly trade wind combined with the residual circulation from the Coral Sea inflow. (C) MODIS chlorophyll-a image of the central and southern GBR showing oceanic (blue) water intruding in the central GBR and flowing southward inshore of the high reef density area. Red is high Chlorophyll-a or turbid water; blue is low Chlorophyll -a water; and black is land and cloud (Steinberg, 2007). (D) MODIS satellite view of ocean color of the central GBR on August 9, 2011. The satellite view indicated a coastal boundary layer with its width increasing southwards, and similar to the conceptual model (B).

3.4 Conclusions

The NCJ inflow has shown to be important mechanism for the flushing of waters in the GBR. Hancock et al (2006) and Wang et al. (2007) have previously estimated the residence time using measurements of salinity and radionuclides combined with very simple 1D cross-shelf diffusion models and simple exchange models that neglect advection due to the NCJ inflow from the Coral Sea. The time for water to completely leave the GBR is in the order of a couple of weeks for offshore water and 3 months for inshore areas, but these results were dependent on high values of the diffusion coefficient estimated for the cross-shelf mixing, and this high diffusion coefficient was likely to compensate the missing NCJ inflow.

The NCJ inflow and the fluctuating southeasterly wind increase the flushing times in inner shelf waters because of the reversing wind driven currents transport some water back to source. A similar process to that in the GBR is observed in an estuary, where waters leaving the estuary at ebbs tides may return later at flood tide, a process parameterized by the return coefficient (Lermusiaux, 2001; Haley Jr. et al., 2009).

In estuaries the reversal tidal currents increases the propensity of water particles to return the estuary for a few hours or even days (Arega et al., 2008; de Brauwere et al., 2010). In contrast, for the GBR the reversal wind-driven currents may transport water back to source after a few weeks. The resulting return coefficient may be as large as 60%.

For the whole central GBR the flushing time was calculated in the range of 1.5 to 9 months. For the real wind condition, the flushing time was 67 days. The largest flushing time (i.e. ~9 months) was calculated for calm weather and negligible NCJ inflow, which is a flushing time controlled by diffusion, i.e. tidal mixing. While the shortest flushing time (i.e. ~1.5 months) was calculated under calm weather and applying the NCJ inflow from the Coral Sea. For the bays the flushing time was calculated between 0.5 to 6 weeks. The effect of the NCJ inflow and the wind was to reduce the flushing time in the bays. Despite the fact that the absolute values of the deviation are small, a residual current of 0.01 m s^{-1} would result in a transport of ~6 km in a week, which is nearly one third of the width of the smallest bays (B_1 , B_2 and B_3). However, the inshore residual currents connect from cape to cape, and the main

physical mechanism responsible to water renewal in those bays is tidal dispersion as shown in the results neglecting the Coral Sea inflow.

The flushing time varied between the different areas in the central GBR depending on the size and location of those areas, which raises a potential deficiency of the 1D models (Hancock et al., 2006; Wang et al., 2007). Although the results presented here are not directly comparable with the results of Wang et al., 2007 and Hancock et al., 2006, because the time scale is defined differently, it is evident that residence times in the GBR calculated from our model are less than 1 year as inferred from some of the results by Luick et al., 2007. Our predicted flushing times are also larger than a few weeks as inferred from 1D models (Hancock et al., 2006), using a simple water exchange model (Wang et al., 2007), and using satellite tracked drifters (Choukroun et al., 2010).

The principal mechanism for flushing of the GBR is the oceanic inflow of the NCJ that enters the central GBR on the outer shelf and creates a mean current that replaces the GBR water with oceanic water. To that process are added tidal mixing and wind-driven currents. A previously unsuspected finding is the importance of the unsteadiness of the wind. Under southeasterly wind, an inflow occurs in the southern GBR and prevails in coastal waters, flowing in opposite direction to the mean current driven by the NCJ. As a result the southeasterly wind was observed to deflect seaward away from the inner shelf towards and toward the outer shelf the southward flowing NCJ inflow, making room for a wind-driven current of opposite direction on the inner shelf. A similar process was observed at the New Jersey shelf and on the continental shelf north of the Monterey Bay (Haley Jr. and Lermusiaux, 2010; Ramp et al., 2011). The reversing currents generate a high value of the return coefficient, as high as 60% over a time scale of several weeks.

Acknowledgements

The authors wish to thank to the IPRS Fellowship to FPA.

CHAPTER 4

‘Sticky water’ enables the retention of larvae in a reef mosaic

Fernando P. Andutta^{1, 2, 3}, Michael Kingsford⁴, Eric Wolanski⁴

¹ School of Engineering and Physical sciences, James Cook University, Townsville QLD 4811, Australia.

² ACTFR, James Cook University, Townsville, QLD, 4811, and Australian Institute of Marine Science, Townsville, Australia.

³ Australian Institute of Marine Science, Townsville, Australia.

⁴ School of Marine and Tropical Biology, James Cook University, Townsville, QLD, 4811, Australia

This chapter reproduces the following paper:

Andutta, F.P., Kingsford, M., Wolanski, E. (In press). ‘Sticky water’ enables the retention of larvae in a reef mosaic. *Estuarine, Coastal and Shelf Sciences*.

Keywords of this chapter: exposure time; patchiness; tidal currents; residual currents; larval dispersion; self-seeding.

To study retention of waterborn larvae in a reef matrix we used a finite-element unstructured numerical model with a minimum horizontal resolution of 150 m that can capture variability of currents on a spatial scale relevant to coral reefs in the Great Barrier Reef. Areas of high reef density (i.e. closely aggregated reefs) are poorly flushed because the prevailing currents are steered around and away from these regions, which is an oceanographic process called the ‘sticky water’ effect. The model showed that the sticky water effect leads to decreased flushing and a high exposure time in high reef density areas in the southern and central regions of the GBR matrix. In turn this generated hotspots of high self-seeding, and these hotspots existed under both calm weather conditions and wind conditions typical of those during the coral spawning season. Away from these areas, self-seeding was less likely to occur and larval

replenishment would result mainly from connectivity between reefs located kilometers to tens of kilometers apart.

The location of sticky water areas varied spatially within the reef matrix according to tidal and mean currents, local bathymetry and reef density (defined as the degree of aggregation by reefs). A simple analytical formula is presented that explains about ~70% of the variation in larval retention in both calm weather and windy conditions. Complex reef mosaics and the related sticky water effect may have significant implications on the fate of larvae, and thus on connectivity for coral reefs worldwide.

4.1 Introduction

The circulation of water around islands and reefs is a key driver of ecological factors such as connectivity, dispersal and species assemblages (Wolanski et al., 1997; Jones et al., 1999 and 2005; Swearer et al., 1999; Carleton et al., 2001; Almanay et al., 2007; Paris et al., 2007; Burgess et al., 2007; Munday et al., 2009; Christie et al., 2010a,b, Hamann et al., 2011). Most of these studies have focused on relatively isolated reefs. Coral eggs and fish larvae spawned in isolated reefs may be potentially easily expatriated. Retention of these eggs and larvae near their natal reefs has commonly been attributed to eddies (Graber and Limouzy-Paris, 1997; Crawford et al., 1990). Indeed, large-scale eddies in the ocean outside a reef can return larvae to their natal reefs after weeks to months (Lobel and Robinson, 1986; Lee et al., 2002). For some reef fishes and corals the lower rates of flow commonly at neap tides may improve retention of fish larvae and coral eggs near natal reef (e.g. Babcock et al., 1986; Gladstone and Westoby, 1988; Robertson et al., 1990; Reynolds and Sponaugle, 1999; Sponaugle et al., 2002). Levels of natal recruitment are known to be high at some reefs (e.g. 30–60%; e.g., Jones et al., 2005; Almanay et al., 2007), this level of self-recruitment is likely to vary by bathymetric and oceanographic context (i.e. tidal and residual currents) as well as the role of larval behavior (Kingsford et al., 2002). Large-scale oceanic eddies do not exist in a reef matrix (Wolanski, 1994) and reef-induced, reef-size eddies are short-lived (e.g. tidal phase-eddies, Black and Gay 1987; Wolanski et al., 2003; Burgess et al., 2007). Retention in semi-permanent eddies from strong current flow on the wake of shallow individual reef, therefore, lasts only hours to a few days at most (Spagnol et al.,

2002). However fish and coral larvae commonly remain at sea for days to weeks before they settle, i.e. when recruitment occurs (Hutchings et al., 2008). Accordingly, it is unlikely that reef-induced phase-eddies can generate a high degree of reef self-seeding. Recruitment to many reefs is likely to be highly subsidized by connectivity with reefs that are km to tens of km apart, and occasionally hundreds of km apart (e.g. Cowen et al., 2006 for Caribbean reefs, and Ayre and Hughes 2000; Bode et al., 2006; and van Oppen et al., 2008 for the Great Barrier Reef).

Reefs in the Great Barrier Reef are not distributed uniformly; most reefs are aggregated in a matrix of reefs. Where the density of the reef matrix is high (i.e. reefs closely aggregated), the self-seeding potential may increase because the reef matrix steers the mean circulation away from and around the reef matrix (Figure 4.1). This process was demonstrated from field and model studies by Wolanski and Spagnol (2000) and Spagnol et al. (2001) and was coined the 'sticky water effect' by Wolanski (1994). The focus of their study was on the deflection of the mean circulation away from and around the reef matrix. These authors did not study variation in the reef matrix, namely that as the complexity of within reef and among reef architecture goes up, the sticky water effect should increasingly dominate, reducing expatriation and increase retention of waterborne larvae.

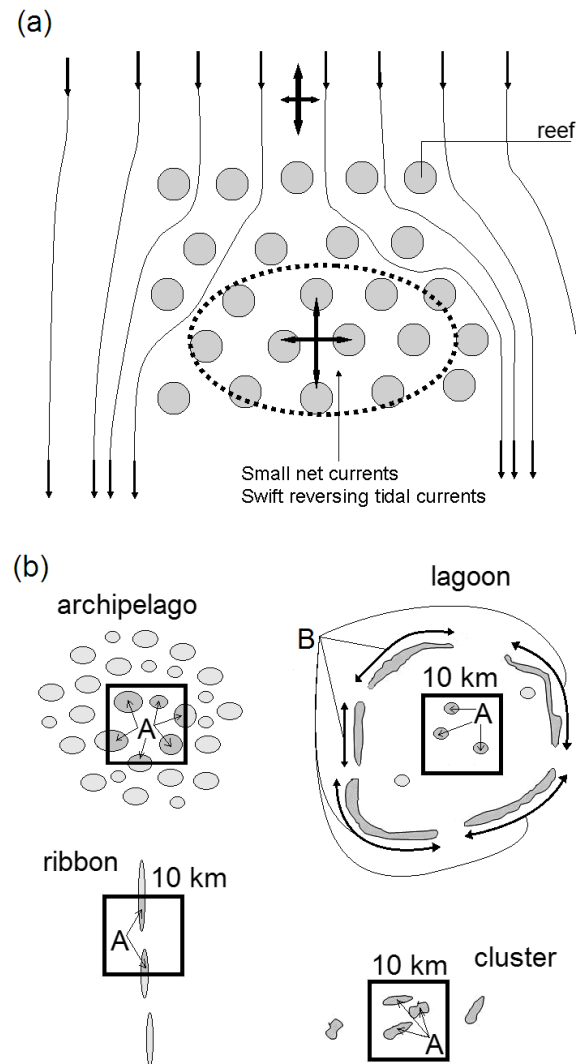


Figure 4.1 – (a) Sketch of the sticky water effect in a reef matrix over a continental shelf, showing (lines) streamlines of the residual current and (crosses) the tidal ellipses. (b) Definition of the reef architecture. Parameters A and B refers respectively to the degree of closure around the spawning sites and degree of reef area within the spawning site, where A and B vary between 0 (minimum) and 1 (maximum).

In this paper we used a high resolution oceanographic model to demonstrate that in areas of high reef density waterborne larvae may be retained for several weeks, a period long enough for the larvae to develop to a competent settlement size. The choice of the numerical model was crucial because the model must be able to cope with details of the complexity of the bathymetry. To model the GBR accurately one must cope with 2800 reefs scattered over its 2600 km length, with reefs ranging in area from ~ 0.1 – ~ 100

km² and often separated by narrow passages (i.e. tens to a few hundred meters). Finite-difference, regular grid models would need millions of grid points to represent the whole GBR at small scales of about 150 m. This is prohibitive and as a result modellers generally use a coarse grid to cope with the whole GBR. For instance Dight et al. (1990) used a 9.26 km grid, King and Wolanski (1996) and Brinkman et al. (2001) used a 2 km grid, and Luick et al. (2007) used a 1.8 km grid. In contrast a non-structured grid model, such as the SLIM model of Lambrechts et al. (2008) allows for fine-scale resolution (~150 m) near reefs and a coarser resolution far from reefs, where high resolution mesh is not needed (Legrand et al., 2006; Andutta et al., 2011), so that the numbers of grid points typically is less than 0.1 million. 2D vertically-integrated numerical models are useful tools to simulate the hydrodynamics in the GBR because Luick et al. (2007) found few differences between the results from a 3D model and a 2D vertical integrated model for the GBR; this is because with the exception of upwelling events at the shelf break (Andrews and Furnas, 1986), and short periods of stratification where large rivers discharge in the coastal zone (Wolanski and van Senden, 1983) there is negligible density stratification with depth.

We used the SLIM model to demonstrate that the sticky water occurs in patches throughout areas of high reef density in the southern GBR matrix. We show that these areas have a high self-seeding potential and that their location is determined by the interaction between the reef density and the oceanography of surrounding waters. We suggest that the GBR, and by inference also reef archipelagos elsewhere, have hot spots of high self-seeding reefs imbedded within a network of reefs that are heavily subsidized by larvae from other reefs. We argue that this self-seeding effect has important ecological and management implications for coral reefs.

4.2 Methods

We used the vertical integrated SLIM non-structured finite-element model of Lambrechts et al. (2008). This depth-averaged barotropic model computes the horizontal velocity and sea surface elevation. Unlike previous models of the GBR, the equations are discretized on a fully unstructured mesh. Thus, the resolution was very high (~150 m) near reefs where it is needed and coarse (~5 km) in open waters far from reefs (Figure 4.2).

TOPEX data was used to force sea level variation and currents at the open boundaries. The exposure time was calculated for simulations starting at 1st August 2006 and 8th August 2006 for conditions initially under neap and spring tides, respectively. For the Coral Sea inflow (Figure 2) we applied 4 Sv to the open boundary, between $\sim 16.3^\circ$ S and 17.4° S ($1 \text{ Sv} = 1 \times 10^6 \text{ m}^3 \text{ s}^{-1}$). This inflow was the North Caledonia Jet (NCJ) (Andrews and Clegg, 1989; Wolanski, 1994; Ganachaud et al., 2007; Lambrechts et al., 2008; Andutta et al., 2011). For the bottom friction we used high values of the Manning roughness coefficients over the reef zones ($2.5 \times 10^{-1} \text{ m}^{-1/3} \text{ s}$) to simulate high roughness and lower values ($2.5 \times 10^{-3} \text{ m}^{-1/3} \text{ s}$) elsewhere. Higher and lower values of roughness coefficients compared to the value $2.5 \times 10^{-2} \text{ m}^{-1/3} \text{ s}$ from King and Wolanski, 1996, were obtained from the adjustment of the currents within the high reef density zones and its surrounding areas. In addition, reef zones have higher friction than those of sand.

The eddy viscosity parameterization of Smagorinsky (1963) was used. The coefficient for the horizontal diffusion of mass, K_h , is assumed to be a function of the mesh resolution, but constant in time. The detailed description of the physical and numerical parameters used in the simulations follows Andutta et al. (2011).

To verify the model we used the data from tide gauges and moored current meters of Andrews (1983), Wolanski et al. (1989), Spagnol et al. (2001), Middleton and Cunningham (1984) and the salinity data from Andutta et al. (2011). The location of the current meter moorings is shown in Figure 2; the moorings were all deployed outside of the GBR reef matrix except for those of Spagnol et al. (2001). The residual currents were measured at 10 moored sites, and tidal currents at 10 sites.

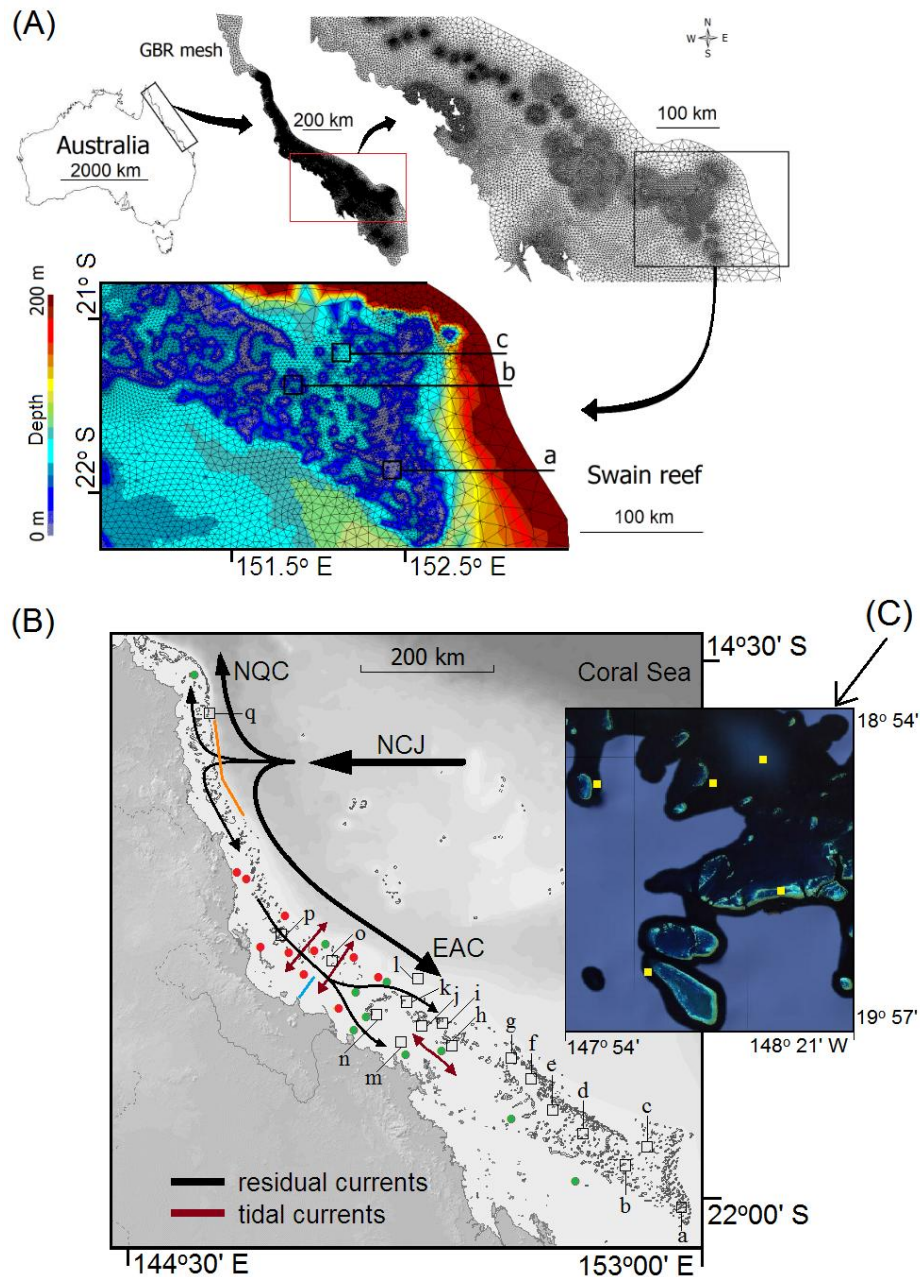


Figure 4.2 – (A) Location map showing the grid over the whole GBR; the high resolution near reefs is highlighted by a zoom on the Swain reef area where were located three virtual spawning areas namely, (a) large dense archipelago, (b) large medium density archipelago and (c) large low density archipelago. (B) Map of the southern and central regions of the Great Barrier Reef, Australia. Field data sites of tidal currents (red dots), residual currents (green dots) and the salinity transect (blue line); (NCJ) North Caledonia Jet; (EAC) Eastern Australian Current; (NQC) North Queensland Current. Residual circulation indicated by the black arrows, and the dominant direction of the tidal currents is indicated by the double pointed brown arrows. The Coral Sea inflow was applied along the orange line. The squares (a) to (q) indicate the location of the virtual spawning sites in areas of different architecture. (C) Location of current meters in the sticky water experiment of Wolanski and Spagnol (2000) and used in this study to demonstrate that the mean currents are deflected around a high reef density area.

While the open boundary conditions for the model, namely the tides and the inflow from the Coral Sea, are well known, the wind is an additional independent variable. On the GBR mass coral spawning usually occurs in November and December. We used two wind conditions typical of those months, namely (1) no wind conditions (Oliver et al., 1992), and (2) a southeasterly wind at 6.67 m s^{-1} , which is the long-term wind speed and direction for the southern GBR during that period (Wolanski, 1994).

This model provided the current data needed to track waterborne larvae using the Lagrangian advection-diffusion model of Spagnol et al. (2002). One hundred thousand virtual non-swimming larvae were released in one batch at each of the 17 spawning sites (Figure 4.2B) for a 2 months simulation. Each such site was a $10 \times 10 \text{ km}$ square (i.e. 10^3 virtual lagrangian particles per km^2). It was not useful to use a smaller square because it needs to be larger than the maximum tidal excursion length ($\sim 6 \text{ km}$). It was not useful either to use a larger size (e.g. $100 \times 100 \text{ km}$) because that scale is much larger than that of which reef density varies ($\sim 10 \text{ km}$). A $10 \times 10 \text{ km}$ box was adequate because numerical experiments showed that particles released at small reefs within such a box quickly filled that box, while large reefs fill the box and thus spawning can be considered uniform within the box.

The spawning sites were chosen to encompass a range of reef architecture from isolated reefs to complex reef mosaics to lagoons. Coral eggs are buoyant and are not uniformly distributed vertically; this lasts less than a day at which time larvae emerge. Coral larvae are largely not buoyant (Black et al., 1990; Black, 1993), and thus vertically integrated models may be used to study their fate.

Our terminology for reef architecture (Figure 4.1b) was as follows. Firstly, an *archipelago* is a reef mosaic bigger than the $10 \times 10 \text{ km}$ site and the reef density A ($0 < A < 1$) is the fraction of the area covered by reefs; a reef is defined as an area of depth less than 5 m ; for instance $A = 1$ means that reefs cover the entire spawning $10 \times 10 \text{ km}$ spawning site. Secondly, a *lagoon* is an area of the shelf that is partially enclosed by reefs that are outside the $10 \times 10 \text{ km}$ site; reefs within the $10 \times 10 \text{ km}$ site may contain reefs at a density A ; the degree of closure of the lagoon perimeter is the ‘lagoon closure’ B ($0 < B < 1$); for instance, $B = 0$ if there is no lagoon enclosing the spawning site, and $B = 1$ if the lagoon fully encloses the spawning site (i.e. the lagoon is mainly flushed by flows over the reef flat). Thirdly, a *cluster* refers to an assemblage of reefs where some reefs are partially shielded by adjacent reefs (i.e. a lagoon closure $B < 0.5$). Fourthly, a

ribbon refers to a series of linear reefs separated by a narrow passage. The characteristics of the reef architecture and the value of the parameters A and B for the 17 spawning sites are listed in Table 4.2.

The self-seeding potential was estimated as the mean exposure time, which is defined as the time needed for the number of larvae in the spawning site to finally decrease to $1/e \sim 0.37$ of its initial value (Deleersnijder et al., 2001; Delhez, 2006; Monsen et al., 2002; Lucas et al., 2009; Valle-Levinson, 2010). Therefore, the exposure time is the time necessary for $\sim 67\%$ of the larvae to leave the spawning site and never return. The self-seeding potential was also calculated as the percentage of larvae remaining in the spawning site after 12 and 24 days.

4.3 Results

The whole GBR model was successfully verified against observations of residual currents at ten sites of tidal currents (Table 4.1; Fig. 4.2B), of tidal currents at the same ten sites (not shown), and of tides at another ten sites (not shown). The root mean square error (RMSE) for the residual currents was only 0.03 m s^{-1} . While most data are for open waters far from reefs, the model within the GBR matrix was also verified (Table 4.1) for the high reef density area shown in Figure 4.2C using the oceanographic data of Wolanski and Spagnol (2000) to demonstrate that the currents upstream of a high reef density area are steered away from the area to flow around it instead of through it – i.e. the ‘sticky water effect’ of Wolanski and Spagnol (2000).

Table 4.1 – Observed (U_o) and predicted (U_p) longshore residual currents (m s^{-1} , >0 if northward, <0 if southward) and peak tidal currents (U_T , in m s^{-1}) at mooring sites. The location of the current meter mooring sites is shown in Figure 2. The data sources A, B, C and D refer respectively to Andrews (1983), Wolanski et al. (1989), Spagnol et al. (2001) and Middleton and Cunningham (1984). The root mean square error RMSE (m s^{-1}) is shown in the last row.

Currents (m s^{-1}) in the GBR at mooring sites						
Site name	Latitude ($^{\circ}\text{S}$)	Longitude ($^{\circ}\text{E}$)	U_o	U_p	U_T	Source
Lizard Island	-14.7406	145.4253	0.05	0.07	0.23	C
Cape Upstart	-19.6253	147.9142	-0.11	-0.10	0.63	C
Old Reef	-19.4071	148.0197	-0.10	-0.09	0.59	
near shelf break	-18.8311	148.2896	-0.25	-0.20	0.36	A
Myrmidon Reef	-18.2452	147.4100	-0.18	-0.25	0.52	A
Bowden Reef	-19.0600	147.9597	-0.02	-0.02	0.47	B
Ratray Island	-19.9826	148.5833	-0.08	-0.09	0.47	
Hook	-19.9400	149.1100	-0.15	-0.16	0.71	D
Bushy	-20.8900	150.1600	-0.13	-0.14	0.32	D
Bell	-21.8200	151.1400	-0.06	-0.07	0.45	D
RMSE	-	-	-	0.03	-	-

Where the reef density was high the tidal currents were also the smallest except in small isolated reef passages (Fig. 4.3). There was a great variation in the residual currents and the peak tidal currents for the Swain reef area (Fig. 4.3). Three virtual spawning sites (a)–(c), each 10 x 10 km, were within the Swain reef area and were within a relatively short distance from each other (Fig. 4.4A). The residual currents (Fig. 4.3) were found to be the smallest in site (a) of high reef density; they were the largest in the site (c) of small reef density, and intermediate in site (b) of moderate reef density.

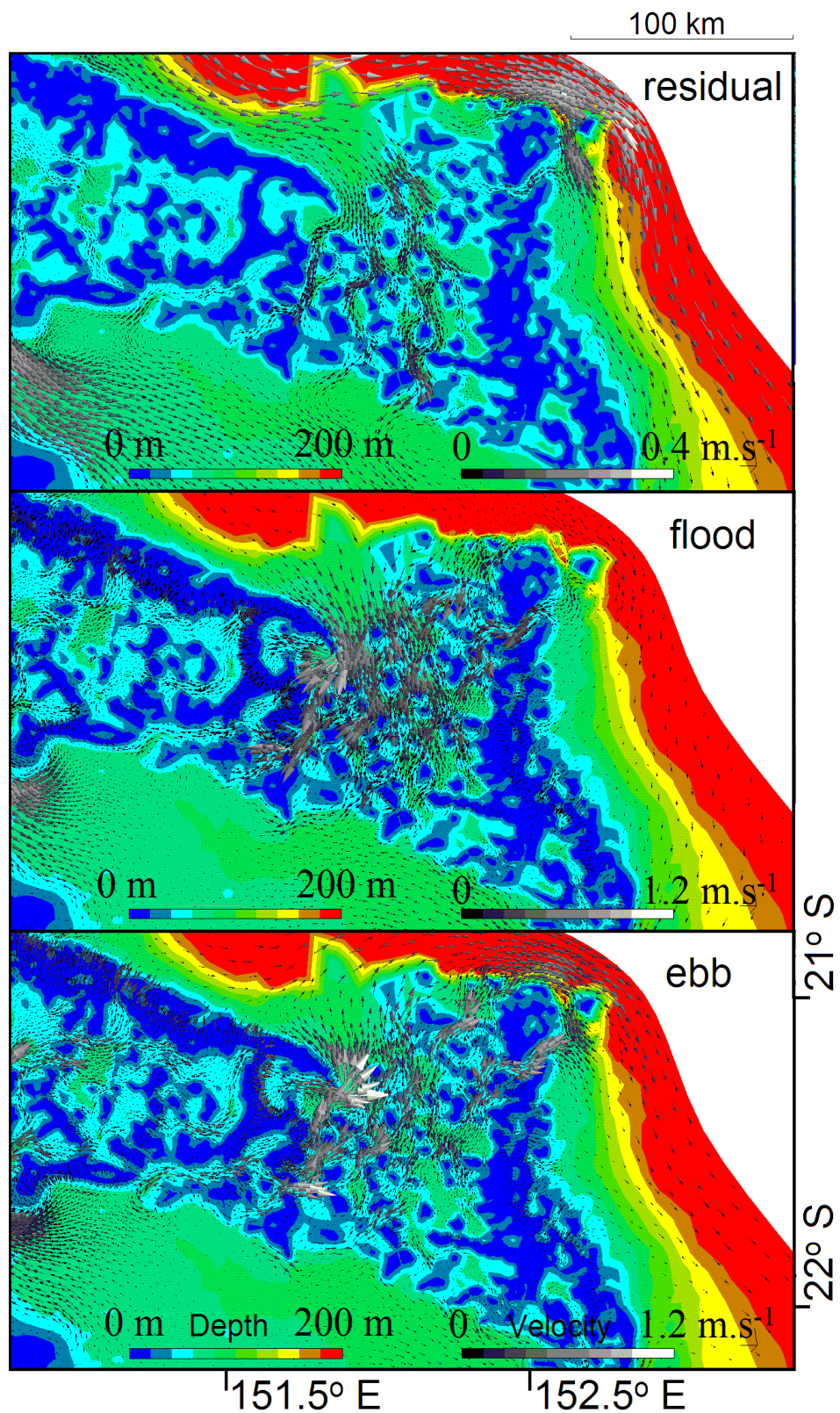


Figure 4.3 – Predicted residual currents and the peak tidal currents during flood and ebb in the Swain reef area.

In calm weather conditions, most (~62%) simulated larvae remained after 12 days in the spawning site (a) where reef density was high (95%, see Table 2), and about 30% of the larvae remained after 24 days. In contrast only few (~3%) larvae remained after 12 days and no larvae remained after 24 days at site (c) where reef density was small (3%). At site (b) where the reef density was 55%, about 16% and 4% of the larvae remained after 12 and 24 days respectively.

The rate of loss of larvae from spawning sites was the smallest at site (a) where reef density was the highest, it was the largest at site (c) where reef density was the lowest, and it was intermediate at site (b) where reef density was about half way between that at sites (a) and (c) (Fig. 4.4B). This decrease in larvae number was modulated by the tides that resulted in rises and falls in number of larvae as the larval plume moved in and out of the spawning sites.

The trapping efficiency was parameterized by the exposure time. During calm weather conditions (see Table 4.2) it was 20.6 days for site (a), 7.5 days for site (b), and 2.5 days for site (c). During windy conditions the exposure time was 18.4, 8.7 and 4.8 days for sites (a), (b) and (c) respectively.

Seventeen sites with various reef architecture were selected (Fig. 4.2) for a sensitivity study. Exposure time results varies greatly from site to site (mean = 7.15 ± 6.6 days; maximum = 22.8 days; Table 4.2). Areas in a high-density archipelago (high value of A) or those in a highly restricted lagoon (high value of B) had the largest exposure times (14.8–22.8 days). Areas partially sheltered upstream by large reefs (i.e. in the lee of a large reef or sandwiched between two reefs) had a relatively high exposure time (4.7–6.6 days) but only if the tidal currents were small, otherwise the exposure time was much smaller (e.g. 1.8 days at site J). By contrast the flushing of larvae was very swift at isolated reefs at sites l and m in open offshore waters, with an exposure time of 1 day (Table 4.2, Fig. 4.4B). Open inshore waters similarly had an exposure time of 1.3 day (site m in Table 4.2). The Ribbon Reefs (site q, Table 4.2) had an exposure time of 1.1 day, similar to that in open waters site q.

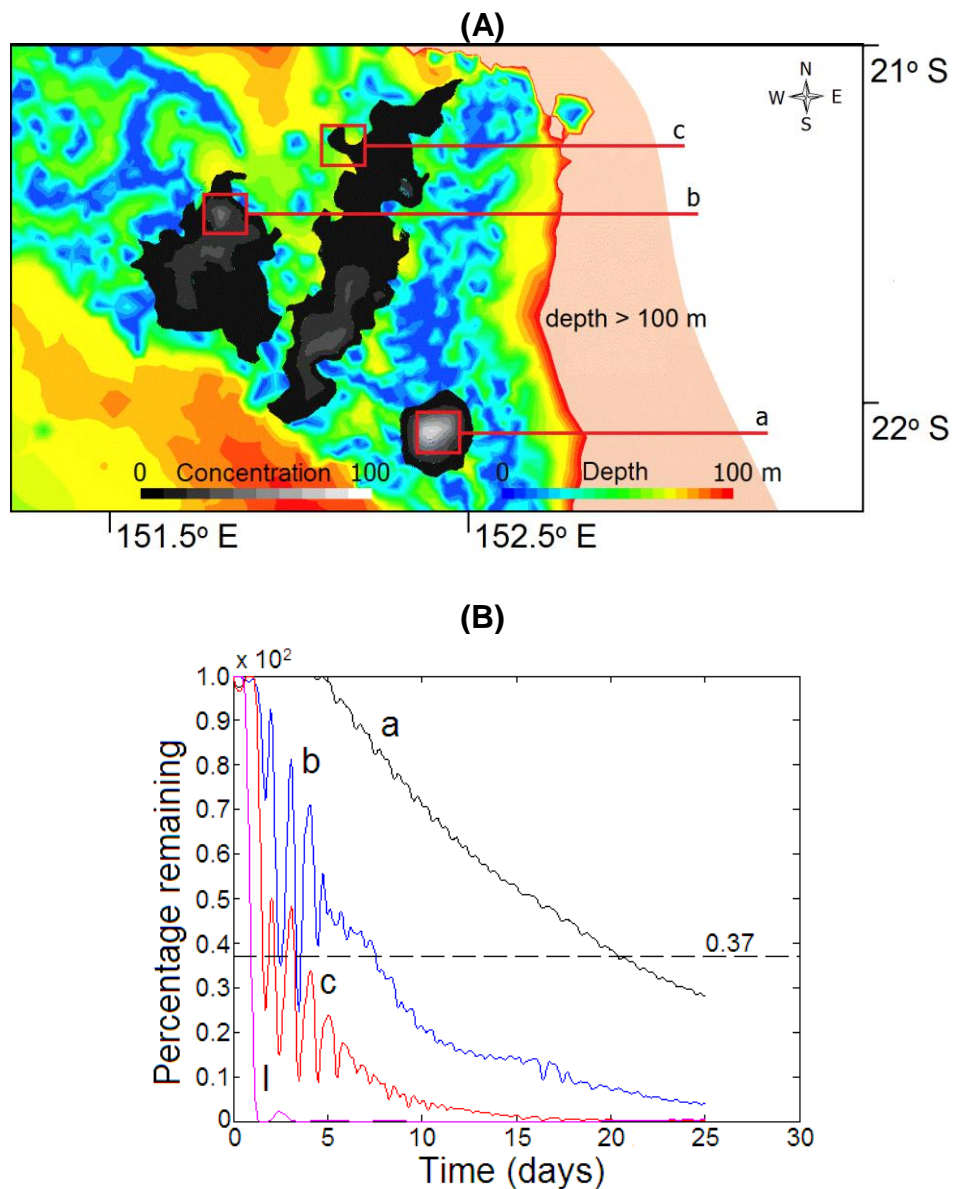


Figure 4.4 – (A) Distribution of the virtual larvae plume after 12 days originating from three spawning sites in the Swain reef area, namely, (a) high-density archipelago, (b) medium-density archipelago and (c) low-density archipelago. (B) Time-series plot of the percentage of larvae remaining in the (10 by 10 km box) of the areas a, b, c and l (area characteristics see Table 4.2), and the simulation started at 1st of August 2006. The mean residence time is the time needed for the number of larvae inside the box to decrease to 0.37 its initial value (Deleersnijder et al., 2001).

Table 2. Location, reef architecture characteristics, and the reef cover parameter A and the lagoon closure parameter B of the 10 x 10 km spawning sites shown in Figure 2. The exposure time T_1 (in days) under calm weather, is estimated for simulations starting and neap (1st of August 2006) and spring tides (8th of August 2006). During calm weather conditions and for a simulation starting under neap tides, the table shows the relative number N_1 and N_2 (in %) of larvae remaining in the spawning sites after 12 and 24 days respectively. During windy conditions and for a simulation starting at neap tides, the residence time T_2 (in days) of the spawning sites. U_{R1} and U_{R2} ($m s^{-1}$) are the residual currents in the spawning sites under calm weather and windy conditions, respectively. U_T ($m s^{-1}$) is the peak tidal current averaged spatially in the spawning sites.

Site	Lat. (° S)	Long. (° W)	Reef architecture	(A)	(B)	(neap) T_1	(spring) T_1	N_1 (12 d)	N_2 (24 d)	T_2	U_{R1}	U_T	U_{R2}
a	21.95	152.45	large dense archipelago	0.95	0	20.6	20.5	62.4	29.8	18.4	0.01	0.08	0.01
b	21.45	151.85	large medium density archipelago	0.55	0	7.5	5.4	16.1	4.3	8.7	0.06	0.55	0.04
c	21.25	152.15	large and low density archipelago	0.3	0	3.0	3.8	2.7	0.0	4.8	0.10	0.48	0.02
d	21.15	151.25	highly restricted lagoon	0.3	0.95	22.8	22.0	63.1	37.2	27	0.01	0.09	0.01
e	20.75	150.75	highly restricted lagoon	0.7	0.8	14.8	10.5	46.0	21.4	8	0.01	0.14	0.02
f	20.35	150.45	partially restricted lagoon	0.1	0.8	13.0	11.1	42.5	11.5	15	0.01	0.13	0.01
g	19.95	150.05	low restricted lagoon	0.1	0.6	5.2	2.8	7.5	0.0	5.3	0.02	0.23	0.02
h	19.85	149.30	reef cluster shielded but with swift tidal currents	0.1	0.3	1.5	2.3	3.8	0.0	2.2	0.04	0.30	0.04
i	19.55	149.15	cluster with small reefs	0.1	0.5	10.1	6.7	31.4	19.2	8.1	0.02	0.35	0.02
j	19.55	148.85	cluster of reefs with side shielded and swift tidal currents	0.1	0.3	1.8	0.8	0.0	0.0	1.9	0.01	0.55	0.01
k	19.25	148.65	cluster with large reef > 10 km	0.95	0.3	6.6	6.8	7.7	0.4	8.1	0.01	0.20	0.01
l	19.05	148.75	open area at shelf break	0	0	1.0	1.1	0.0	0.0	1.1	0.12	0.23	0.07
m	19.85	148.65	open inshore area	0	0	1.3	1.6	0.0	0.0	1.8	0.11	0.49	0.01
n	19.35	148.15	cluster with large reef, shielded upstream with moderate tidal currents	0.1	0.3	4.7	1.8	0.0	0.0	4.4	0.01	0.35	0.06
o	18.75	147.55	small low density archipelago	0.1	0	2.8	5.4	7.9	0.9	6.9	0.03	0.16	0.01
p	18.35	146.75	cluster with front and back areas of the small reef shielded	0.3	0.2	4.3	5.1	4.9	0.6	5.7	0.02	0.09	0.02
q	15.25	145.75	ribbon reef	0.1	0	1.1	2.0	0.3	0.0	1.0	0.03	0.14	0.04

A MODIS satellite image (Fig. 4.5) is shown to gain confidence in the model skills of capturing the retention of larvae, and to provide a real demonstration of the existence of the sticky water effect within high reef density zones. The MODIS chlorophyll-a image of the central and southern GBR shows oceanic water intruding in the central GBR and flowing southward inshore between the high reef density area and the coast. Therefore, the oceanic inflow from the Coral Sea is mostly deflected away from the high reef density matrix. High chlorophyll-a concentration within closely aggregated reefs evidence the high exposure time, and thus the sticky water effect.

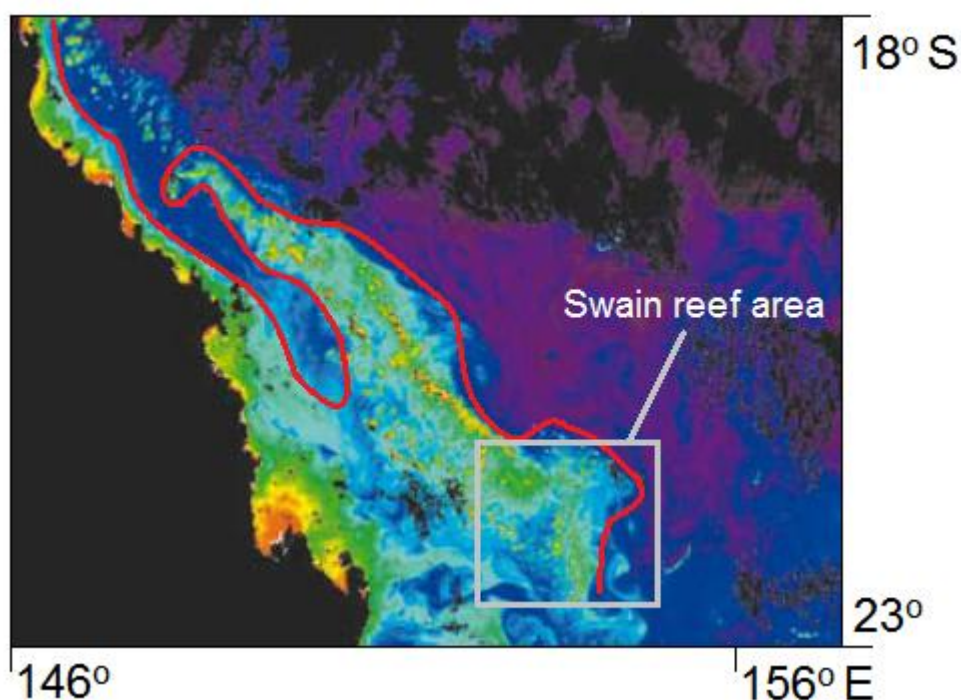


Figure 4.5 – MODIS chlorophyll-a image of the central and southern GBR showing oceanic (blue) water intruding in the central GBR and flowing southward inshore of the high reef density area. Red is high Chlorophyll-a or turbid water; blue is low Chlorophyll -a water; and black is land and cloud (Steinberg, 2007). The Swain reef area is indicated, and shows hot spots of high chlorophyll concentration in high reef density areas in agreement with our estimates of the sticky water effect.

There was a high degree of spatial variability in the exposure time in the GBR (Table 4.2); and, therefore this implies a high spatial variability of the self-seeding potential of various reef areas in the GBR. This variability is partly predictable as a function of the oceanography and the reef architecture. No oceanography field data or

models have so far been proposed to predict the self-seeding potential of a reef matrix. To provide such a predictive tool, two simple equations are proposed below to estimate the exposure time T of the 10 x 10 km spawning sites and thus by inference the self-seeding potential. If oceanographic data are available, we propose the simple empirical formula

$$T = \alpha / (U_R U_T), \text{ where } U_R \neq 0 \text{ and } U_T \neq 0, \quad (4.1)$$

where T is in days and U_R and U_T (in m s^{-1}) are respectively the residual and maximum tidal currents spatially averaged over the 10 x 10 km spawning site, and $\alpha \sim 1159 \text{ m}^2 \text{ s}^{-1}$. In Eq. (4.1) U_R is multiplied by U_T because both U_R and U_T need to be small for the sticky effect to prevail (Fig. 4.1a). If the tidal currents are large, the site will flush swiftly even if the residual current is small. If the residual current is large, the site will also flush swiftly even if the tidal currents are small. The resulting self-seeding potential is never 100% (i.e. $T = \infty$) because waterborn particles are dispersed out of the high reef density area by tidal diffusion. Eq. (4.1) fits the data in Table 4.2 under calm weather conditions with $r^2 = 0.69$ for simulations starting at neap tides under both calm weather and windy conditions. While for simulations starting at spring tides, $r^2 = 0.75$ and 0.69 under calm weather and windy conditions, respectively (Fig. 4.6). Eq. (4.1) could be used for predictions of connectivity at sites for which oceanographic data or a high resolution model is available to estimate both U_R and U_T .

The value of $\alpha \sim 1159 \text{ m}^2 \text{ s}^{-1}$ does not necessarily represent the value of the effective horizontal eddy diffusion coefficient K because in Eq. (4.1) T is proportional to α while in the classical diffusion theory T is proportional to K^{-1} following the formula (Fischer et al., 1979), i.e. $T = L^2/K$, where L is the domain length scale.

In most of the GBR matrix, however, and many other reef mosaics of the world, there are no field data or modelling to estimate U_R and U_T in Eq. (4.1). Then we propose the following simple, but less accurate, empirical formula that requires only a detailed bathymetry map,

$$T = 16 \text{ minimum}(A/(1-B), I) \quad (4.2)$$

where parameters A and B are defined in Fig. 4.1. Eq. (4.2) fits the data in Table 2 with $r^2 = 0.66$ and 0.63 for simulations under calm weather, and starting under neap and

spring tides, respectively. While under windy conditions $r^2 = 0.52$ and 0.48 for simulations starting at neap and spring tides, respectively (Fig. 4.6). It offers a simple way to estimate the likely degree of self-seeding of a reef matrix or an archipelago for which minimal oceanographic data are not available. The estimate is more robust for calm weather conditions than for windy conditions.

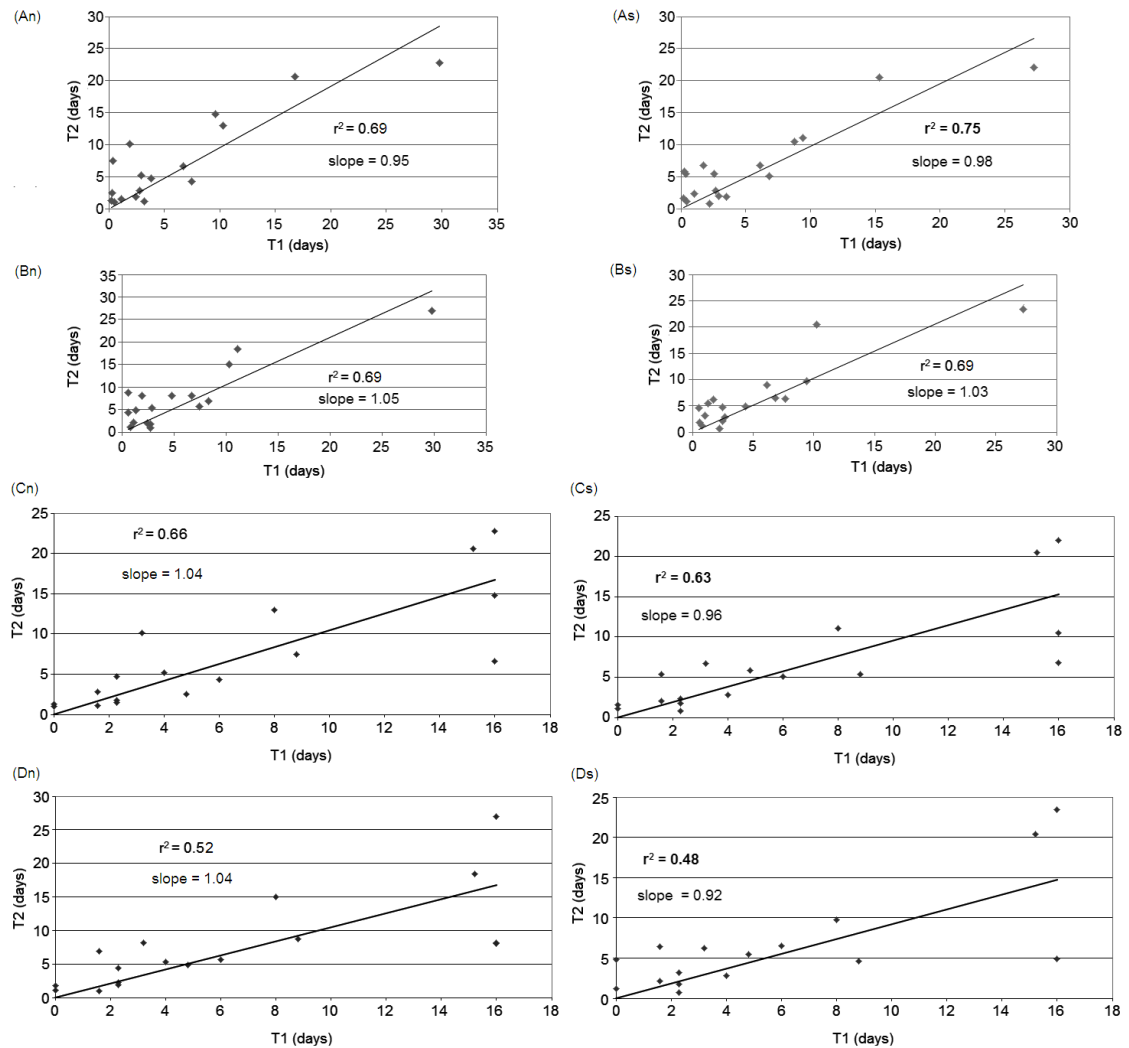


Figure 4.6 – Scatter plot of the residence time T_2 predicted by the SLIM model against the residence time T_1 predicted by Eq. (4.1) for (A) calm weather (no wind) and (B) southeasterly wind of 6.67 m s^{-1} . Residence time T_2 predicted by the SLIM model against the residence time T_1 predicted by Eq. (4.2) for (A) calm weather (no wind) and (B) southeasterly wind of 6.67 m s^{-1} . The figure indices (n) and (s) denotes simulations starting at neap (1st of August 2006) and spring tides (8th of August 2006), respectively.

4.4 Discussion

This study shows that although self-seeding of reefs appeared unlikely based on historical models of water movement (Williams et al., 1984; Jones et al., 2009), our resolution of near reef oceanography has improved and biological evidence indicates that at least at some locations and for some taxa a high percentage of larvae can return to their natal reef (Jones et al., 1999; Almany et al., 2007).

Our models would be conservative for predicting levels of self-recruitment where larvae actively seek home (e.g. Gerlach et al., 2007). Variable mesh-sized models allow for a high resolution understanding of mainstream and near reef currents. It is clear that some scenarios of reef topography and tidal currents facilitate a high level of retention for times that equate with the PLD (Planktonic Larval Duration) of many larvae. PLD of 100 species of Pacific and Atlantic damselfish family was investigated by Wellington and Victor (1989), and the PLD was observed to change between 13 and 35 days. High mobility and strong navigational abilities are not required for high levels of self-recruitment where the sticky water effect prevails.

Our study demonstrated the importance of small scale processes at a horizontal scale <1 km in generating the sticky water effect in regions of high reef density. We have shown that trapping efficiency (i.e. self-seeding potential) increased with reef density (Table 4.2). Most particles were retained within the high reef density spawning sites after 12 days – regardless of tidal and wind-related conditions.

The choice of models in determining the location of self-seeding areas is critical because the models must be able to merge both the large-scales and the small scales for the sticky water effect to be resolved (Wolanski et al., 2003). For a model to predict the self-seeding and connectivity potential within a large region such as the GBR, (1) the whole GBR (region) must be included in the model in order to include the correct forcing by the Coral Sea, and (2) a higher horizontal resolution is required because low resolution (cell size >1 km) erases small reefs and most reef passages and does not yield the correct shear distribution near the edges of the remaining reefs and thus does not simulate correctly the advection-dispersion processes in a reef matrix (Wolanski et al., 1996 and 2003). To meet these criteria, ~ 10 millions of cells would be needed for a high resolution, finite-difference model of the whole GBR. To avoid these numerical pitfalls a non-structured grid model is needed that requires only a few hundreds of

thousands of cells (Legrand et al., 2006). This is the reason why we used the non-structured finite-element model of Lambrechts et al. (2008).

The water circulation in the Great Barrier Reef (GBR) was faithfully reproduced by the model (Table 4.1). Superimposed on the residual currents were tidal currents which, away from the reef matrix, were oriented mainly cross-shelf in areas of low reef density and long-shelf in areas of high reef density. This concurs with other field and finite-difference models with a coarse resolution (King and Wolanski 1996; Brinkman et al., 2001; Dight et al., 1990; Luick et al., 2007).

Our finite-element model has the advantage that it also provides details of the water circulation in the reef matrix. The model shows (e.g. see Fig. 4.3) that the water circulation in areas of high reef density is quite different to that around an isolated reef or island, which is dominated by reef-induced eddies; it is instead controlled by the reef architecture and the prevailing currents in surrounding waters that can create a stagnation or near-stagnation zone.

The residual currents were minimal in the high reef density areas independent of their location on the mid- or outer-shelf. The tidal currents were also reduced in areas of very high reef density, even when tidal amplitude was high. As a result the sticky water effect prevailed in areas of very high reef density, which promoted retention of the waterborne larvae. Most (~ 62%) of the larvae remained in spawning sites with high reef density after 12 days, while less than 3% of the larvae remained after 12 days near isolated reefs (see sites l and m, Table 4.2, Fig. 4.4B).

The distribution of the high self-seeding zones is patchy in a reef matrix but appears predictable. The GBR, and reef archipelagos elsewhere in the world, comprise a number of hot spots of high self-seeding reefs imbedded within a network of reefs that are replenished mainly by long-distance connectivity.

Wind affects currents, especially in shallow water (Wolanski, 1994). For coral reefs on the GBR, many organisms spawn in November and December when light winds generally prevail. We have studied two wind conditions, namely calm weather conditions and a Southeasterly wind at 6.67 m s^{-1} , which is the mean value for those months in the southern region. Our predictions apply to such conditions. In some years however strong winds may apply, and at such times the wind may modify the spatial distribution of the self-seeding due to the influence of wave breaking over the reef crest, and this remains unknown and research is needed. Oceanographic research in the GBR

has historically focused on monitoring and modelling the circulation in the open waters of the GBR continental shelf and thus away from the dense reef matrix (Webster et al., 2008). However, reef ecological research is focused on reefs. Our findings call for a greater focus on the fine-scale circulation within the reef matrix itself.

This study has provided two simple analytical formulae for predicting the retention of passively drifting particles near reefs. These formulae can allow ecologists to make predictions of areas of high self-seeding. Knowledge of this kind can be used to make structured sampling designs where predictions can be made on connectivity in ecological and evolutionary time (e.g. Taylor and Hellberg, 2003; Jones et al., 2005). We predict that relatedness (i.e. genetic panmixis), will be high in areas of sticky water and ‘spill over’ from these source areas may provide larvae to downstream reefs (Carr and Reed, 1993). Reefs of low retention time may depend on occasional changes of residual currents (Williams et al., 1984; Wolanski, 1994; Bode et al., 2006) and winds that alter levels of larval-subsidy from other reefs. The topography, tides and residual currents were a good predictor of stickiness and retention even when a representative wind was included in the model.

Predictions on connectivity can assist in the planning of site and placement of MPA for sources and sink reefs as well as areas where retention is likely to be high (Palumbi, 2004). Cowen et al. (2006) used an oceanographic model of the Caribbean to identify areas with high and low potential for self-recruitment. Our study adds value to Cowen et al.’s conclusions in that we have made specific predictions on tide and topographic categories and metrics that facilitate retention as well as conditions where population subsidies from other reefs are likely.

Currents alone do not describe levels of connectivity as some larvae have excellent swimming ability and sensory systems that provide directionality, potentially allowing them to stay near or search for natal reefs (Kingsford et al., 2002); this capability has sometimes been included in models (e.g. Wolanski et al., 1997; Cowen et al., 2006). The larvae of some taxa have limited mobility and short larval duration (e.g. corals; Kingsford et al., 2002; Connolly and Baird, 2010). In this case, the larvae may behave similarly to as passive particles. In contrast, fishes and some invertebrates are capable of minimising dispersal from natal reefs through strong swimming, directionality and behaviourally altering depth of distribution. Despite this, even fishes have very limited mobility early in life. Many fishes only have strong swimming ability

during the last 0.25 of their planktonic larval duration (Fisher et al., 2000; Fisher, 2005); hence the levels of passive drift explained in our study are relevant.

CHAPTER 5

Review on estuarine hydrology and transport time scales

Eric Wolanski^{1,2}, Fernando P. Andutta¹, Eric Delhez³

¹ Engineering and Physical Sciences School and Australian Centre for Tropical Freshwater Research, James Cook University, Townsville, Queensland 4811, Australia.

² Australian Institute of Marine Science, Townsville, Queensland 4810, Australia.

³ Université de Liège, B-4000 Liège, Belgium.

This chapter reproduces the following book chapter:

Wolanski, E., Andutta, F., Delhez, E., 2012. Estuarine hydrology. In: Encyclopedia of Lakes and Reservoirs. Lars Bengtsson, Reginald Herschy, Rhodes Fairbridge (eds.), Springer, In press.

Keywords of this chapter: estuary; salt balance; classification; sediments dynamics, transport timescales.

5.1 Introduction

The word estuary is of 16th century origin and originated from the Latin *aestuarium*, which means marsh or channel, and this is derived from the Latin *aestus*, meaning tide or billowing movement. Estuaries are transitioning environments between the land and the ocean, where fresh water coming from the rivers mixes with saline oceanic water. This river inflow needs not be perennial. There are several definitions of estuaries. For freshwater scientists the main thing is to define the head of an estuary; in one definition this is the salinity limit; in another definition this is the tidal limit; and in still another definition it is the source of the fluvial sediment. For coastal scientists and oceanographers, the mouth of an estuary, i.e. the point where an estuary ends, is also ill-

defined. It can be a geographic feature or the seaward edge of a tidal plume in the open ocean.

Whatever the geographical definition, an estuary is a zone of transition with gradients in salinity, sediment characteristics, turbidity of the water column, chemical composition including nutrients, dissolved gases and trace metals and in diversity and productivity of species of animals and plants. Estuarine waters are commonly more biologically productive than the oceanic waters. In addition, estuaries are strategic locations for human development; nearly 69 % of the largest cities in the world are located on river estuaries. The scientific understanding of estuaries is thus of great practical importance.

An estuary is never at a steady state. Its bathymetry is continuously evolving. Forced by tides, waves and river inflows, estuarine water is continuously moving and with it its ecology is also continuously evolving. Some largest estuaries may have the additional direct influence of winds on the local circulation such as the Amazon River. The resulting physical and biological features of an estuary and its ecosystem health are determined by the time scales of the processes controlling the movements of water and sediments and the ecological processes in the water and on the bottom.

5.2 Genesis and geomorphologic time scales

The physical features of an estuary are determined firstly in a time scale of centuries from the recovery of the global mean sea level (MSL) from the last glaciation (i.e. eustatic variation) and the tectonic movements that resulted (i.e. isostatic variation), and secondly in a shorter time scale from human-induced changes in river discharge Q_f and riverine sediment inflow Q_s . Global MSL was 120-130 m lower 20,000 years ago than at present (Fig. 5.1a). The melting of the ice resulted in a rebound of the continental plates relieved of the pressure of ice glaciers. As a result the relative MSL varied spatially in three zones (Figure 5.1b) of, respectively, on-going decrease, relative stability, and on-going small increase (Figure 5.1c). The global MSL has been fairly constant the last 6,000 years. It is now at a high stand level that was last reached about 120,000 years ago. Old river and flood plains became flooded by rising seas; estuaries were formed as they filled with sediment originating from the watershed and from the

sea; watershed sediment were brought in by rivers and coastal sediment were brought in by tides and storms.

Thus most estuaries have not reached a steady state yet; they are still evolving. They have an age; they all started young, many have reached maturity though not the fjords, and some have reached old age meaning that they cannot accommodate any additional sediment. The extra sediment is carried seaward to be dispersed at sea or to form a delta. An old estuary can be rejuvenated when a major river flood creates a new river mouth.

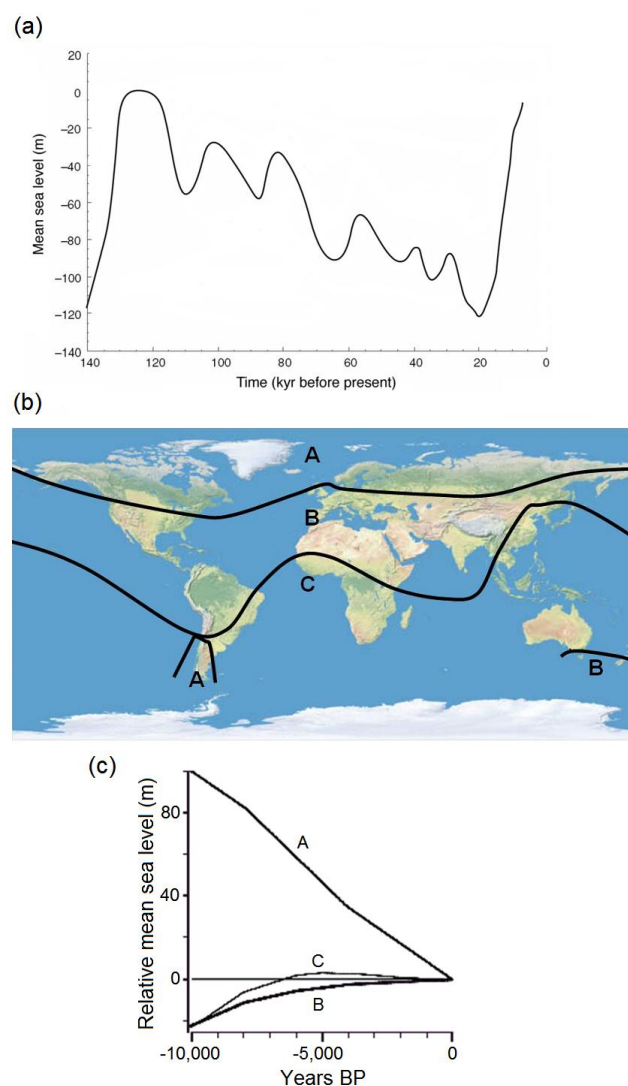


Figure 5.1 – (a) Time series plot of the global mean seal level over the last 140,000 years. (b)The approximate distribution of the coasts that followed one of the three typical relative mean sea-level curve types A, B and C as shown in (c). (Redrawn from Wolanski et al., 2009).

As sketched in Figure 5.2, the infilling of an estuary of volume V is controlled by the inflow of riverine sediment Q_s , the net balance ΔQ_s between seaward ocean flux $Q_{s,out}$ and the landward sediment flux from coastal water $Q_{s,in}$, and the sediment flux to lateral storage in the flood plains $Q_{s,storage}$. The geomorphologic age of an estuary is the time it takes for the net sediment flux to fill the volume V . The aging of an estuary can be greatly accelerated by human activities in the watershed, mainly land-clearing. As an example this geomorphologic age T was estimated for a number of macro-tidal muddy estuaries in the Pacific region (Figure 5.3); T varies between several thousand years for estuaries that are non-impacted by human activities (rank 1), to several hundreds of years for estuaries that are moderately impacted by land clearing in the watersheds (rank 2), to only several tens of years for estuaries that are severely impacted by land clearing in the watersheds (rank 3), illustrating the rapid acceleration of the aging of estuaries by siltation due to land-clearing in the watersheds.

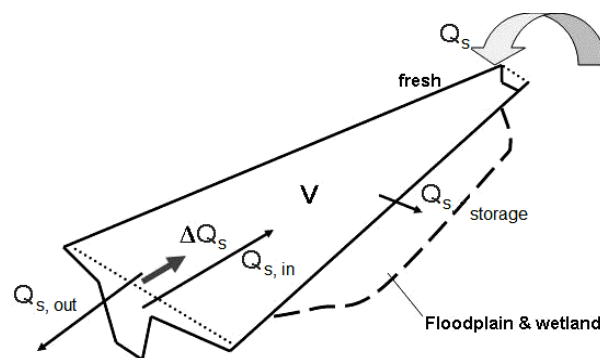


Figure 5.2 – A sketch of the net sediment budget in an estuary.

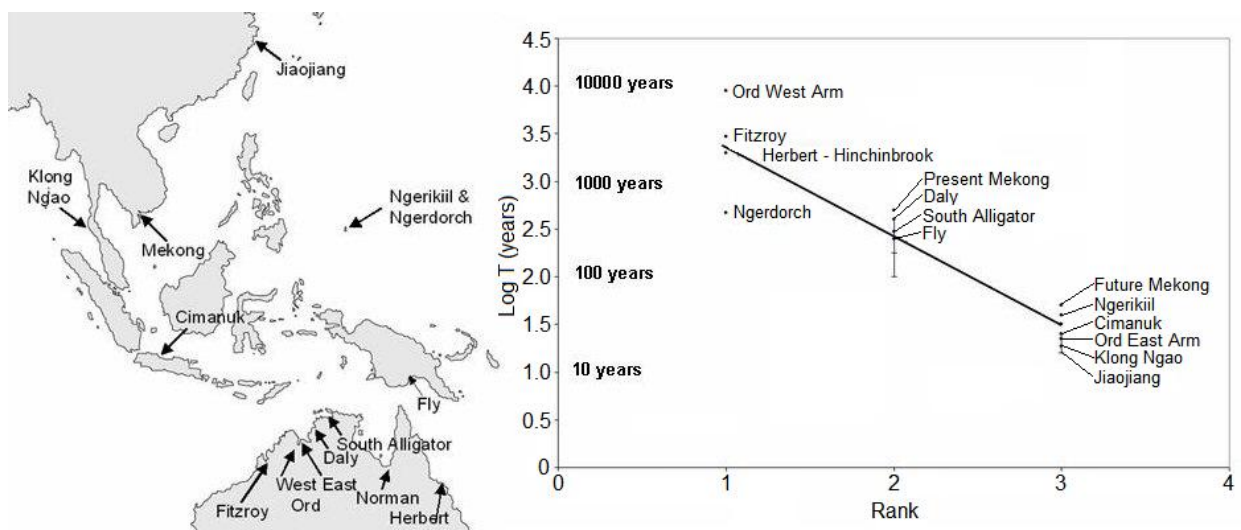


Figure 5.3 – The geomorphologic age of macro-tidal, muddy estuaries in the Pacific.

Dams on the other hand can trap sediment in reservoirs and thus prevent sediment to reach the estuary, which slows down the estuarine aging process. This is particularly the case for micro-tidal and tideless estuaries. Before the mega-dam was constructed some riverine sediment was trapped in the estuary that usually comprised a lagoon and a delta; the rest was exported to the sea (Figure 5.4a). The mega-dams in the Colorado and the Nile rivers have stopped all (most) river floods export of water and sediment to the sea (Figure 5.4b) and significantly decreased the inflow of sediment to the estuary. The channels are silting slower, i.e. aging slower, than before due to lesser sediment inflow from the dam, while the coast is eroding.

However in macro-tidal estuaries, large dams can accelerate the aging of estuaries. This is because they can decrease or even stop large river floods; this prevents seaward flushing of estuarine sediment and accelerates tidal pumping of coastal sediment landward into the estuary; these results in siltation and thus aging the estuary. At the same time however the coast becomes starved of sediments, which are exported by waves and currents in the open sea; as a result the coast erodes.

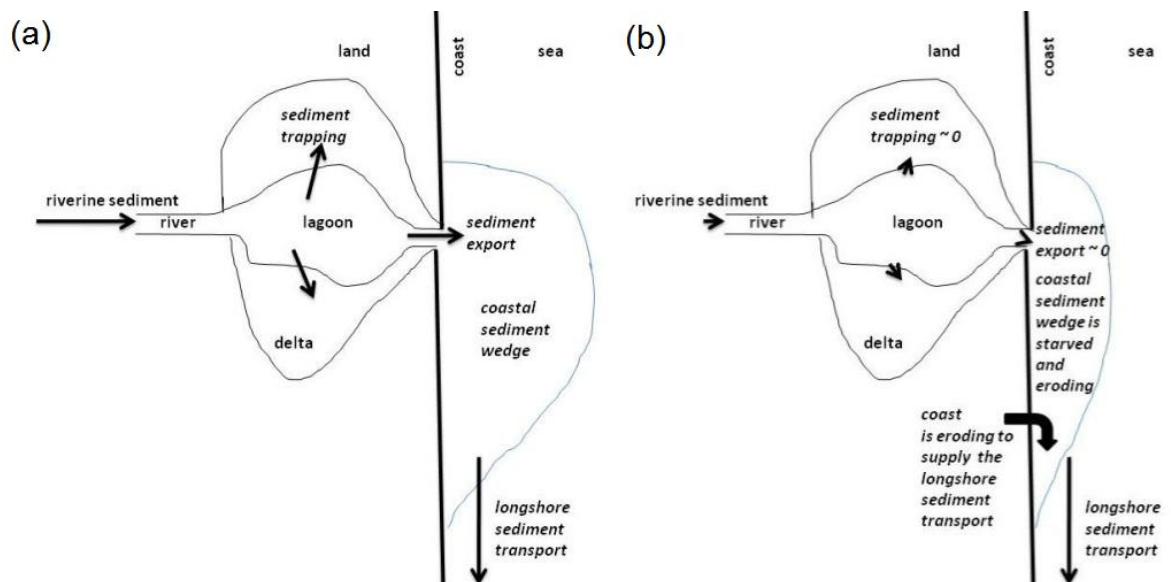


Figure 5.4 – A sketch of the sediment budget in the micro-tidal Nile and Colorado deltas (a) before and (b) after dam construction.

5.3 Sediment dynamics time scales

Estuarine sediments are of two types: cohesive sediment (also called mud or clay) have a mean particle size $d_{50} < 4 \mu\text{m}$; non-cohesive sediment (sand) has a $d_{50} > 64 \mu\text{m}$. Silt has a d_{50} in between those of mud and sand; it is weakly cohesive.

The sediment dynamics depend on the currents, the salinity, the type of sediment and the biology. Sand is mainly carried along the bottom and very close to the bottom. Mud is mainly carried in suspension within the water column.

There are several models, pioneered by engineers, to calculate the sand transport as bed load. The models generally assume either that the sand moves as a creeping movement of layers along the bottom or that the sand particles are rolled and tossed over the bottom in a process called saltation. The models are based on laboratory studies and estimate the bed load transport as a function of the mean particle size d_{50} , the current-induced stress, a threshold stress for bed load to commence, and the difference in density between the water and the sediment. They yield at best order-of-magnitude estimates and thus must be used with caution. Sand is often mixed with mud and even if the sand is the dominant fraction the clay particles modify the bed load by a factor of 2 to 4.

Cohesive sediment (mud) behaves differently than non-cohesive sediment (sand) because it forms flocs typically 100-200 micron in size. Flocculation is initiated by salinity ions that cause electronic forces between the small sediment particles and greatly enhanced by the bacteria and plankton that, through the production of transparent exopolymer particles (i.e. a mucus) aggregate flocs to form extremely large flocs (commonly 1000 micron in size) and called marine snow flocs. In very turbid waters the suspended sediment concentration SSC ($\text{SSC} > 500 \text{ mg l}^{-1}$), marine snow is scarce; in less turbid waters (typically $\text{SSC} < 100 \text{ mg/L}$), marine snow is common. The biology also controls the erodibility of the bottom sediment because algae mats stabilise the bottom sediment and animal burrows may loosen the sediment and facilitate erosion. There are models, pioneered by engineers, to calculate the mud transport as a suspended load. They are largely based on laboratory experiments and they generally fail in the field because the laboratory experiments cannot account for the biology in the field.

The vertical profile of SSC takes many shapes, from vertically nearly well-mixed (line **a** in Figure 5.5), to smoothly increasing with depth (line **b**), to a step

structure called the lutocline for $SSC > 5 \text{ kg m}^{-3}$ (line c). Because the suspended sediment increases the density of the water, the water density changes across the lutocline. This reduces the vertical diffusion coefficient K_z in the lutocline, in the same manner that a thermocline inhibits vertical mixing between the hypolimnion and the epilimnion. This helps preserve a fluid mud layer near the bottom.

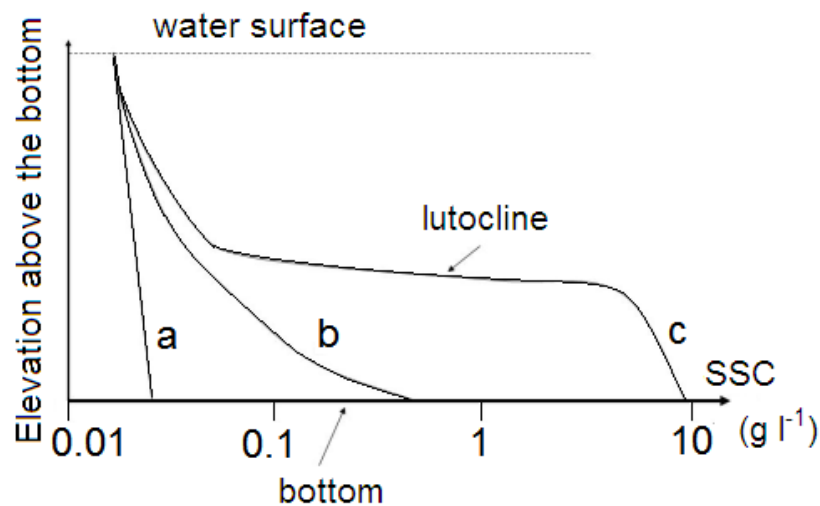


Figure 5.5 – Three typical vertical profiles of suspended sediment concentration in estuaries, where a, b, and c denote a nearly well-mixed profile, slightly mixed and a step structure (known as lutocline).

Riverine mud in suspension commonly reaches the estuary unflocculated. On reaching the estuary this mud flocculates as a result of the action of salinity and the biology (Figure 5.6a). Salinity-driven currents, tidal currents and weaker cohesive forces of silt floccs as opposed to mud floccs generate a physical filter that sorts the silt from the clay (Figure 5.5a) and that creates a turbidity maximum zone (Figure 5.5b). Marine muddy snow forms a biological filter that inhibits the export of mud from estuaries (Figure 5.6c). Finally the riverine mud mixes with, and is diluted by, the estuarine mud through erosion and sedimentation as a result of floods, waves, tides and storms (Figure 5.6d). In some estuaries the tidal currents are larger during the rising tide than during the falling tide; in those estuaries the tides pump the sediment landward. These processes greatly increase the residence time in the estuary of the riverine mud and its particulate pollutants and nutrients.

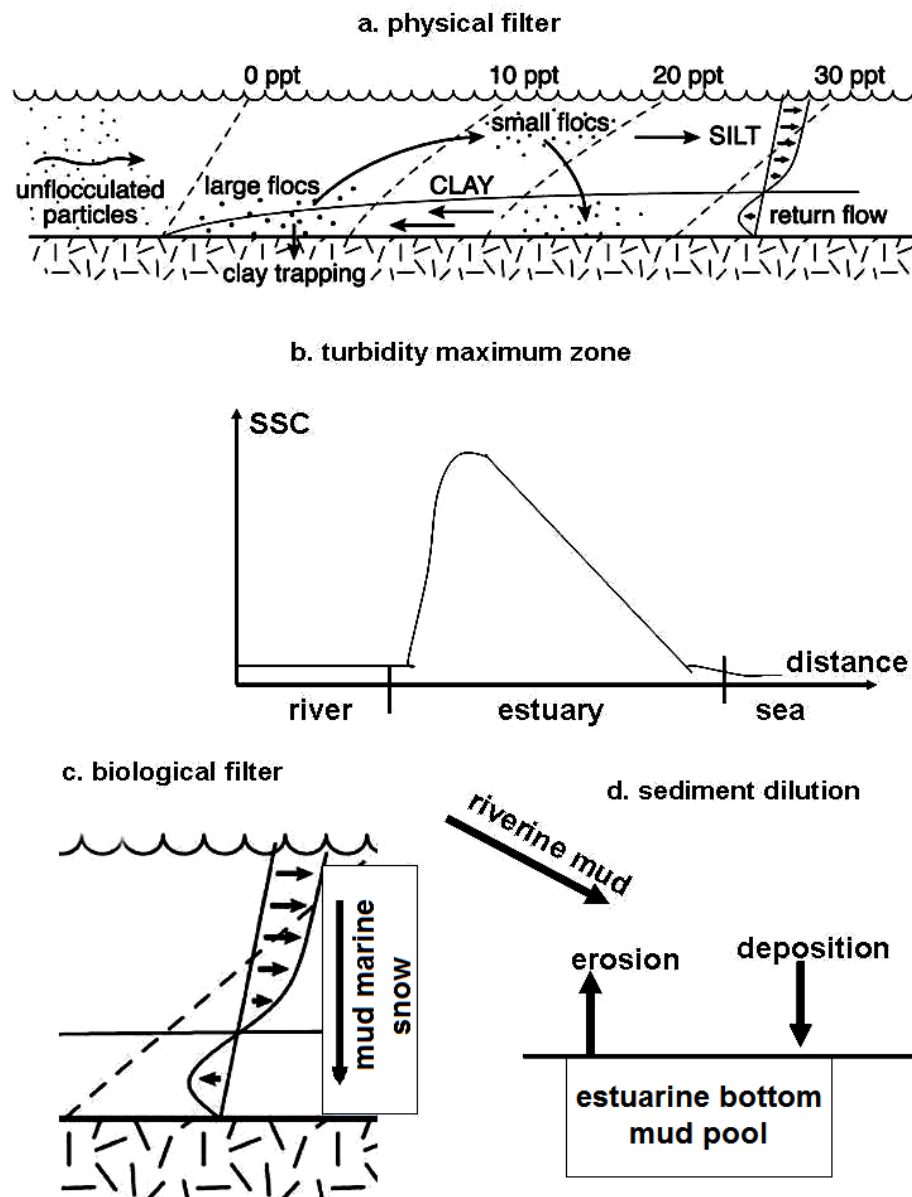


Figure 5.6 – (a) The physical filter of fine sediment that generates (b) a turbidity maximum zone, i.e. a zone with the highest suspended sediment concentration (SSC); the SSC curve varies with the tides. (c) Biologically-produced transparent exopolymer particles and fine sediment in suspension interact to produce muddy marine snow flocs that accelerate the settling of the mud and generate a biological filter inhibiting the export of fine sediment seaward. (d) Riverine mud is diluted by estuarine mud.

If the estuary is sandy, the sediment is also trapped in the estuary and the trap is also leaky, with sediment imported both from the sea and from the rivers and exported offshore during large river floods. The evolution of a sandy estuary geomorphology is difficult to predict because of the difficulties in measuring sandy sediment fluxes. Observations suggest that the dominant forcing functions controlling the movement and trapping on sandy sediments in estuaries are the oceanography (tidal dynamics and storms) and the hydrology (floods).

5.4 Classification based on geomorphology and on water circulation

Estuaries may be classified upon their geomorphology or physical oceanography. The estuarine types based on the geomorphology, are mainly 1) drowned river valleys, (2) lagoon-type or bar-built, (3) fjords. Most of the drowned river valleys were formed with the sea level rise on low and wide coastal plains (e.g. Chesapeake Bay, Tampa Bay and Delaware Bay). The lagoon types are semi-isolated from coastal waters by barrier beaches and some lagoons are extremely large (e.g. Lagoa dos Patos in Brazil that is 242 km long, and the Mirim Lagoon in the border between Brazil and Uruguay that is 290 km long, and the well-known Venice Lagoon, famous in human history). These estuaries have only a few narrow inlets allowing the interaction between the estuary and the coastal zone. The fjords were formed in deeply eroded valleys caused by the glaciers; many of them have shallow areas near the estuarine mouth, and thus restricting the water flow. Fjords often have lower temperatures than coastal waters (e.g. the deepest fjord is the Sognefjord in Norway with depths up to 1300 m, and the largest fjord is Scoresby Sund in Greenland that is 110 km long).

The classification based on the estuarine circulation is based on the vertical distribution of salinity in the estuary, and the types are (1) salt wedge, (2) partially mixed, (3) well-mixed, (4) fjord-type, and (5) salt plug (Figure 5.7). In salt wedge and fjord-type estuaries, the river inflow greatly exceeds tidal currents, freshwater moves as a distinct surface layer, and a sharp salinity interface separates the fresh/brackish water on top from the saline water underneath. In partially mixed estuaries the tidal currents only slightly exceed river inflow, and thus cause more vertical mixing, which reduces vertical salinity gradients. Well-mixed estuaries are dominated by tidal mixing, thus the vertical salinity stratification is negligible. Salt plug estuaries occur in the dry climates,

where evaporation greatly exceeds river inflow, resulting in higher salinity in the estuary than at the mouth.

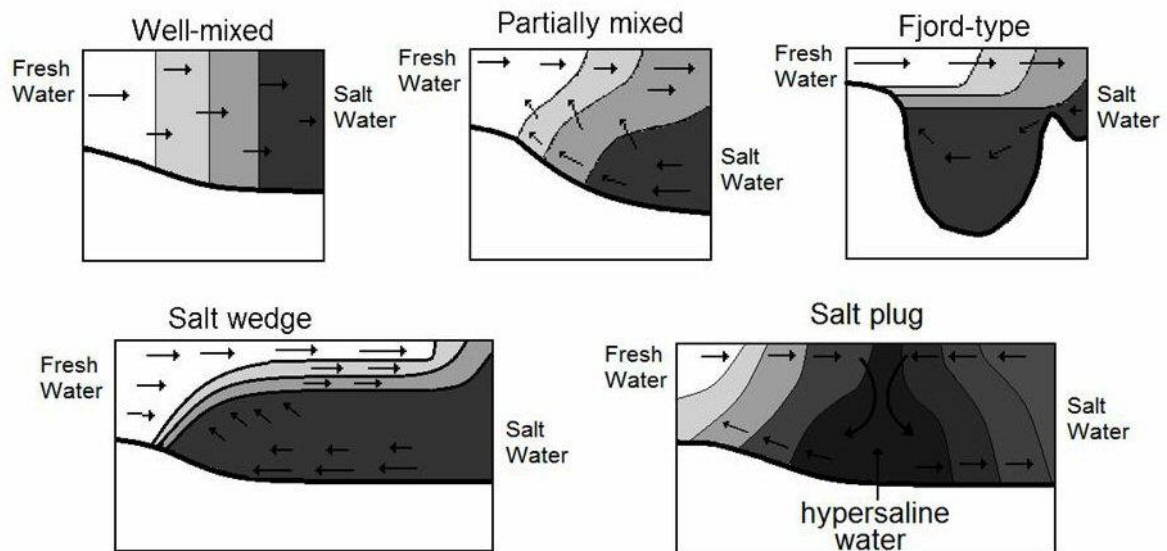


Figure 5.7 – Classification of estuaries based on the physical oceanography.

5.5 Biological implications of sediment transport

At high SSC (highly turbid), there is nearly complete darkness. Typically, for suspended sediment concentration (SSC) = 0.2 g l^{-1} , visibility < 30 cm; for SSC = 1 g l^{-1} , visibility < 1 cm. The plankton in these turbid waters can only photosynthesise for the short time that it is brought to the surface by turbulence. The benthos has no such opportunity; it stays in complete darkness as long as the water stays turbid. In addition even in the absence of suspended sediments, light is attenuated with depth depending on the plankton (shading effect) and on dissolved organic matter (DOM).

Mud also affects pollutants (such as Polychlorinated biphenyls PCBs and heavy metals) and nutrients (particularly Phosphorus, less so for Nitrogen) because these particles are readily absorbed on the mud due to the electric and colloidal forces on the clay particles. Thus pollutants can stay trapped hundreds of years on settled mud and are released when the mud is resuspended. Suspended mud is important in absorbing dissolved nutrients and largely making it unavailable by the plankton. This is quantified by the partition coefficient K_d

$$K_d = \text{mass absorbed on particulates} / \text{Total mass} \quad (5.1)$$

and this was quantified by Middelleburg and Herman for estuaries in Europe; they found at suspended particulate matter (SPM) of 10 mg/L about 10% of the organic Carbon may be present in particulate form, and this was about 50% at SPM of 100 mg/L and 80% at SPM of 400 mg/L. Phosphorus is also readily absorbed on suspended mud and Nitrogen less so. Thus in muddy estuaries the classical stoichiometry ratios for dissolved inorganic nutrients C:N:P=106:16:1 may not hold, and this invalidates the use of aquatic ecosystem models based on stoichiometry.

In muddy estuaries most heavy metals and a number of pollutants such as PCBs and Persistent Organic Pollutants POPs are nearly totally sequestered on mud particles; they are thus extremely slowly flushed out of polluted, muddy estuaries, and are thus a legacy of pollution that may last many decades, and even centuries, after the pollution source was stopped. This is the case for instance of Boston Harbour in the USA and the Elbe Estuary in Germany.

The impact of riverine nutrients on an estuary is very different for a sandy (clear water) estuary where the nutrient is readily bioavailable and light penetration allows photosynthesis, than for a muddy (turbid) estuary where much of the nutrient, especially phosphorus, is absorbed on the mud and photosynthesis is inhibited by the lack of light.

5.6 Tidal wetlands

The vegetation in tidal wetlands plays an important role in controlling the net sediment flux in or out of an estuary. These wetlands were originally non-vegetated intra-tidal mudflats are exposed at low tide and inundated at high tide. These mudflats commonly have a tidal creek that focuses the largest currents in the creek; the currents remain small in the surrounding flats where sediment can thus accumulate. These non-vegetated mudflats are often unstable and are readily modified by storms. All this changes drastically when the sediment accumulation results in the substrate rising above mean sea level. At that stage the vegetation establishes itself, consisting typically of salt marsh plants in temperate climate and mangroves in tropical climates. Through its roots below ground the vegetation helps stabilise the tidal creek; through its structure above ground the vegetation accelerates sedimentation by slowing down the water and thus

enabling the suspended sediment entering the intertidal areas at rising tide to deposit. The difference between the sediment that comes in at rising tide and the sediment that goes out at falling tide is the sediment trapped in the tidal wetlands. This role of vegetation is crucial in enhancing sediment trapping in estuaries; for instance a mangrove that covers 3.8% of the river drainage area traps 40% of the riverine mud inflow; a salt marsh where plant height exceeds 8 cm may enable sedimentation at a rate of up to 8.2 cm yr^{-1} ; the rate of sedimentation of British saltmarshes averages 4.3 mm yr^{-1} and a similar result is also found in U.S. saltmarshes. Storms may disturb this trend in the short-term.

Tidal wetlands comprise globally mainly mangroves and saltmarshes. Mangroves worldwide cover an area of about $240,000 \text{ km}^2$ and are the dominant coastal wetland in subtropical and tropical regions where frosts do not occur. Saltmarshes are distributed worldwide, mainly in areas subject to frosts where mangroves do not grow and in the higher grounds next to mangroves; thus they are most common in middle and high latitudes; their vegetation comprises mainly salt-tolerant grasses and rushes. Mangroves and saltmarshes vegetation exhibit zonation patterns whereby the vegetation is the thinnest in the areas of lowest elevation where sediment accretion occurs. A mild slope in the vegetated wetlands forms a drainage pattern toward the tidal creek.

The importance of tidal wetlands to the estuarine ecosystem is not limited to sequestering nutrients and pollutants. Tidal wetland vegetation converts excess nutrients in the flowing waters into plant biomass; in turn this plant biomass supports an ecosystem. Organic detritus such as plant litter is exported from the wetlands to the estuary. The wetlands also provide a nursery for fish and crustaceans that come in from the estuary – and the sea for migrating species - to feed and shelter within the saltmarsh and later return to the estuary or the sea; this forms an important exchange of organic nutrients between the tidal wetlands on the one hand and estuarine and coastal waters on the other hand. The nutrient outwelled from tidal wetlands increases the estuarine plankton community, which in turn support commercial fisheries of fish and shrimps, the success of which is closely linked to tidal wetlands.

5.7 The water transport time scales

The movement of water in an estuary is controlled by the tides, the river inflow, rainfall and evaporation, the wind, and events at sea such as storms. The multitude and variety of these factors, their interaction with the often shallow and highly irregular bathymetry, contribute to a complex non-linear and unsteady three-dimensional hydrodynamics.

Models of varying complexity can be used order to describe and quantify the transport of pollutants and the renewal of water.

Box models, in particular, are often used for a quick assessment of the flushing capability of an estuary. In the simplest approach, the estuary is modeled as a single box. Assuming steady-state, the turnover time or flushing time T of the estuary can then be estimated as

$$T = V / Q \quad (5.2)$$

where V is the water volume in the estuary and Q is the total freshwater input. In tidal estuaries, the amount of water exchanged at each tidal cycle is estimated as the difference of water volume between high and low tides, the so-called tidal prism V_p (Figure 5.8a). Using this tidal prism flushing model, a fraction

$$r = V_p / V \quad (5.3)$$

of the estuary water is assumed to be renewed by ocean water at each tidal cycle and the turnover/flushing time can be expressed as

$$T = \tau / r \quad (5.4)$$

where τ is the tidal period (e.g. 0.5 day for solar semi-diurnal tide and 1 day for solar diurnal tide).

The above models provide a very crude description of the exchange processes between the estuary and the coastal sea region. Very often, the net water exchange results from the difference between two opposite water fluxes corresponding to the inflowing sea water and the outflowing estuarine water. In the gravitational circulation model (Figure 5.8b), these water fluxes are associated with the two-layer baroclinic

circulation typical of partially mixed estuaries (Figure 5.7). In well-mixed broad estuaries, the two opposite fluxes can occur simultaneously in the horizontal plane (Figure 5.8c).

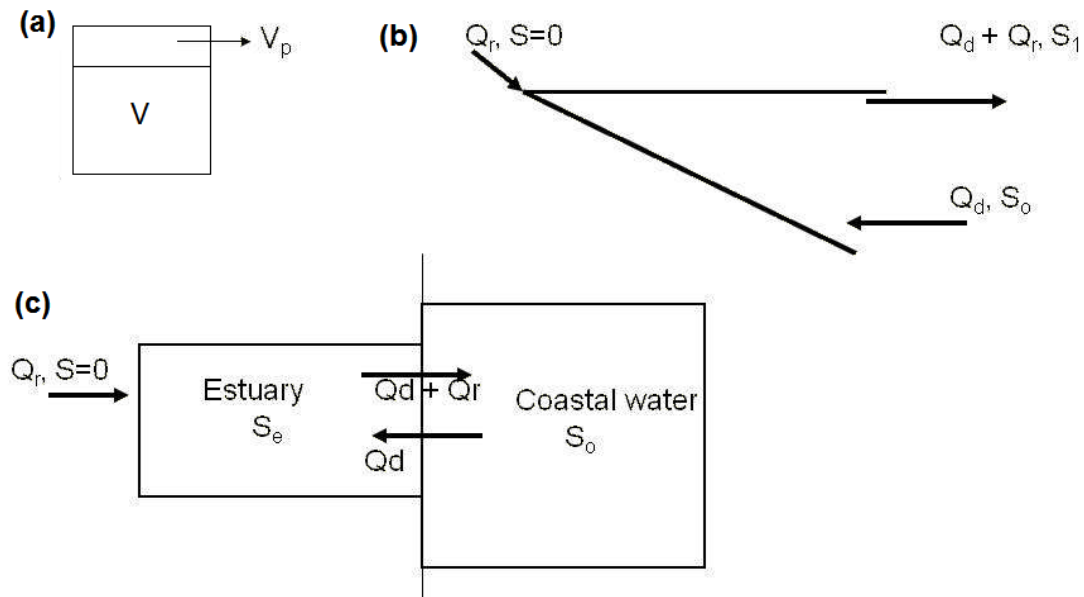


Figure 5.8 – (a) The tidal prism box model (side view); (b) the gravitational circulation box model (side view); (c) the LOICZ box model for a vertically well-mixed estuary (plan view).

Using the configuration of the LOICZ model (Land-Ocean Interaction in the Coastal Zone) shown in Figure 5.8c, the steady state water balance in the estuary requires that the outflowing flux be the sum of the freshwater input in the estuary Q_r and the seawater inflow Q_d . Expression (5.2) of the turnover time can then be generalized with $Q = Q_r + Q_d$.

As steady-state, the rate Q_d can be calculated from the salt balance

$$Q_d \Delta S = Q_r S_{out} \quad (5.6)$$

where S_{out} is the salinity of the estuarine outflow and ΔS is the excess salinity brought by the seawater, i.e.

$$\Delta S = S_o - S_e \quad (5.7)$$

where S_o is the salinity in coastal waters and S_e is the estuarine salinity. Setting $S_{out} = S_e$ leads to the

$$T_r = V/Q_r (1 - S_e/S_o) \quad (5.8)$$

The LOICZ method for the derivation of the renewal time is similar but S_{out} is taken as the mean salinity in the outer estuary, which is estimated as

$$S_{out} = 0.5 (S_o + S_e) \quad (5.9)$$

The LOICZ box model is simple and easy to use and has been used in about 200 estuaries worldwide. Rainfall, groundwater and evaporation can also be added if needed. If the system is not vertically well-mixed, a stacked box model can be used with a box on top representing the upper layer and a box on the bottom representing the lower layer and the vertical fluxes are calculated from salinity data.

The above box models, which can be further refined, are useful as a first approach but have serious limitations because they only capture some of the physics (e.g. Sheldon and Alber, 2006). they are all based on a steady state balance, assume complete and immediate mixing in the estuary, poorly account for the diffusive fluxes between the estuary and the coastal sea and ignore the spatial variations inside the estuary.

The flushing rate and the transport of pollutants also depend on the internal circulation within the estuary driven by the density difference generated by changes in salinity and temperature. This difference in density is determined by vertical mixing by the wind, by boundary-generated turbulence, and by turbulence in the water currents driven by tides, wind and river inflow. Vertical mixing is parameterized by the vertical eddy diffusion coefficient K_z , which is minimal at the level of the density interface (i.e. the pycnocline). Additional mixing also results from turbulence generated at the banks of the estuary and by secondary flows around shoals and islands, as well as 3-dimensional flows in meanders.

A proper description of estuarine dynamics and the assessment of the associated transport rates require therefore two-dimensional (either in the horizontal or in the

vertical plane) or even three-dimensional models. Such models are elegant but they still carry uncertainties in term of the hydrodynamic conditions and the fate of tracers at the open boundaries as well as in quantifying the turbulent diffusion. Also the influence of small scale features and the possible occurrence of *sandbanks* that fall *dry* at *low tide* require special numerical treatments. Unstructured grid models permitting local refinements of the computational mesh where necessary and taking into account external influences in a natural way are particularly suited for such studies.

The refined description of the water circulation provided by high resolution numerical models gives also access to more representative transport timescales, namely the age, the residence time, the exposure time and the transit time, superseding the poorly defined flushing time, turnover time and renewal time. These timescales are best introduced by considering the fate of a water parcel or of a tracer particle (Figure 5.9).

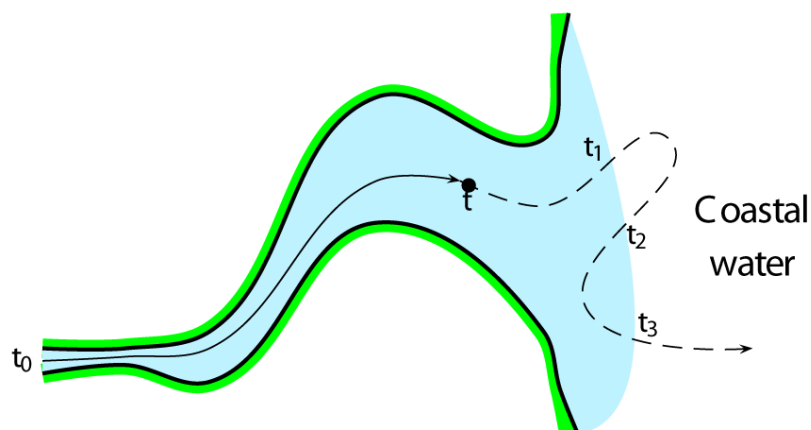


Figure 5.9 – Path followed by a particle in the estuary from the upstream boundary to the coastal sea. At time t , the age of the particle is $t-t_0$, its residence time is t_1-t , its transit time is (t_1-t_0) , its exposure time is $(t_1-t)+(t_3-t_2)$.

The age of a particle measures the time elapsed since it entered the estuary. The age reflects therefore the past history of the particle. With the residence time, one looks forward in time: the residence time is time necessary for a water parcel originally in the estuary to leave the domain for the first time. The exposure time is similar to the residence time but allows for particles to return into the estuary after leaving it (with reversing tidal currents, for instance) ; the exposure time of a particle originally in the

estuary is the total time that the particle will spent in the estuary. The transit time of a particle is defined as the sum of the age and the residence time.

Because of mixing, different particles introduced in the estuary at exactly the same location and at the same time will follow different trajectories and are therefore characterized by different timescales. Distributions of age, residence time, exposure time and transit time must therefore be considered, although one can usually content one-self with their average value in most cases.

The Constituent oriented Age and Residence time Theory provides the appropriate framework to compute the above timescales in an Eulerian framework, in a suitable form to be easily implemented in existing numerical models. The mean residence time \mathcal{G} , for instance, can be obtained as the solution of the advection-diffusion problem

$$\frac{\partial \mathcal{G}}{\partial t} + \nabla \cdot (v \mathcal{G}) + \nabla \cdot (K \cdot \nabla \mathcal{G}) \quad (5.10)$$

(where t is the time, v is the velocity and K is the diffusion tensor) with boundary conditions prescribing that \mathcal{G} vanishes at the open boundaries. To compute the exposure time, the same equation must be solved but the model domain must be extended offshore to describe the coastal circulation and describe the possible return path of tracers. Exact analytical solutions are available if the estuarine cross-section is constant along the channel, which is often a restrictive assumption.

Table 5.1 compares transport timescales computed using different approaches in various estuaries. Large differences between the various time scales exist for the same estuary, highlighting the importance of defining precisely the particular time scale needed for particular applications.

When the estuary is density-stratified, the residence time of water in an estuary also depends on the internal circulation within the estuary driven by the density difference generated by changes in salinity, temperature and suspended sediment concentration. This difference in density is determined by vertical mixing by the wind, by boundary-generated turbulence, and by turbulence in the water currents driven by tides, wind and river inflow. Vertical mixing is parameterized by the vertical eddy diffusion coefficient K_z , which is minimal at the level of the density interface (i.e. the

pycnocline). Additional mixing also results from turbulence generated at the banks of the estuary and by secondary flows around shoals and islands, as well as 3-dimensional flows in meanders.

When the bathymetry is complex, e.g. with meanders or shoals, the water circulation in estuaries also varies markedly across the width, forming regions of convergence (where floating matter accumulates) or divergence (where floating matter disperses swiftly). This also modifies the water transport time scales.

Table 5.1 – Example of the water transport times (in days) for various vertically fairly well-mixed estuaries.

	Renewal time (LOICZ box model)	Average residence time (CART, 1D)	Average exposure time (CART, 1D)	Average residence time (numerical model)
Curimataú Estuary (Brazil)				
Neap tides	0.5-0.9	0.1-0.6	1.2-1.7	-
Spring tides	0.5-1.4	0.02-0.1	1.4-2.2	-
Hudson Estuary (USA)				
Neap tides	4.3-5.3	1.2-2.3	6.2-6.7	8-10
Spring tides	4.2-5.2	1.3-2.3	10.1-11.2	8-9
Conwy Estuary (UK)				
Neap tides	31.8-35.3	10.2-12.8	74.6-81.1	-
Spring tides	28.1-31.2	6.0-7.7	109.5-120	-
Mersey Estuary (UK)				
Typical flow range	3.5-7.8	0.5-1.7	35.4-99.5	1-6.3
Sheldt Estuary (Belgium-The Netherlands)				
Average conditions	23.8-75.2	5.3-10.4	204.1-302.5	5-70

5.8 Ecological implications of the transport time scales

For a given estuary the geomorphologic time scale determines the estuarine bathymetry. The habitats, including tidal wetlands and rocky zones, are determined by the underlying geology as well as the geomorphologic time and sediment transport time scales. The fate of nutrients and pollutants is determined by the habitats, and the sediment and water transport time scales. In turn all of these parameters determine the ecology of the estuary.

In a vertically well-mixed estuary, the nutrient is cycled between phytoplankton and resuspended microphytobenthos, zooplankton, bivalves and crustacea, and fish (Figure 5.10). Dying organisms, excreta, and left-overs from messy eaters become detritus that is recycled, some through the microbial loop. As shown by the dotted lines, tidal wetlands provide detritus and juvenile fauna to the estuary. This ecosystem is not closed, in fact it is supported by an inflow of nutrients, fish and plankton from the sea and the watershed (the river and groundwater); some of that matter is also lost by export to the sea. The level of processing of these various inflows depends on a large number of parameters including the climate, the habitats, the intensity of the inflows, the water and sediment transport time scales, and the partitioning coefficient. In turn the estuarine ecosystem is determined by these physico-chemical attributes and the ecological niches.

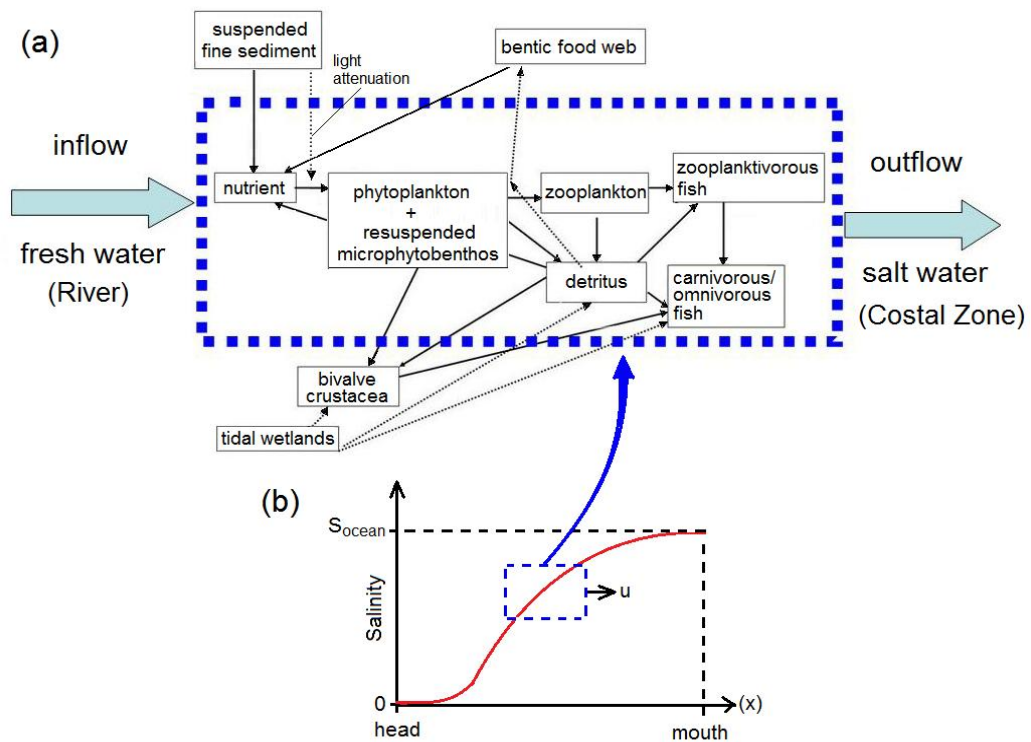


Figure 5.10 – (a) A typical pelagic food web in a vertically well-mixed estuary. It comprises a waterborne ecosystem (the blue box) that is moving with the water currents, thus comprising an inflow into the estuary and an outflow from the estuary; it is flushed at a rate determined by the water transport time scales. It comprises also suspended sediment that is also varying in time at a rate determined by the sediment transport time scales. It comprises also a benthos and bottom dwelling animals living in habitats that are varying in time at a rate determined by the geomorphologic time scale.

(b) Typical salinity distribution increasing from the head to the mouth. The waterborne ecosystem (blue box) is advected seaward, thus remaining only in transient contact with the substrate and the tidal wetlands, and at the same time it is subject to increasing salinity as a result of mixing. As it moves towards the head of the estuary, the waterborne ecosystem also encounters different habitats.

The same nutrient cycling may prevail in the top layer of a salt wedge estuary (Figure 5.11). However the situation is very different in the bottom layer, which is enriched by organic matter falling down from the top layer especially if the top layer supports an algal or plankton bloom. This organic matter decays in the bottom layer and extracts dissolved oxygen from the water column. As the bottom layer is not in contact with the water surface and the salinity stratification completely shuts down the turbulence at the salinity interface, oxygen cannot be supplied from the top layer. Oxygen can only be supplied by ventilation, i.e. the import of oxygen by currents bringing in oceanic waters in the bottom layer. This bottom layer becomes anoxic if the oxygen consumption rate is larger than the rate of import of oxygen from oceanic water.

Partially mixed estuaries may suffer less from bottom water anoxia than salt wedge estuaries because the salinity stratification is less intense and does not completely shut down the turbulence; some vertical mixing remains and as a result additional oxygen is provided to the bottom layer by vertical diffusion of oxygen from surface waters.

Each of these physico-ecological relationships is affected by the human impact. A most common indicator of a severe human impact is that the bottom layer of vertically stratified estuaries – which has the largest water transport time scales - becomes anoxic or hypoxic. Estuaries with a small value of the water transport time scales have less time for the dissolved oxygen to be depleted and for sediments to accumulate in the estuary; such estuaries are thus intrinsically more robust than poorly flushed estuaries.

Another indicator of the human impact is the increasing frequency of harmful algae blooms. High riverine loads of Nitrogen and Phosphorus into an estuary initially lead to a bloom of phytoplankton or diatoms because their rate of uptake of nutrients is much larger than that by cyanobacteria. In nutrient-enriched estuaries located downstream of large dams that preferentially trap the fine sandy sediment, the

phytoplankton or diatoms can exhaust the Silicate but not Nitrogen and Phosphorus; when that happens, cyanobacteria take over and harmful algae blooms can result. This situation is becoming common for many estuaries worldwide with a large water transport time scale and a large input of nutrients from sewage and fertilisers.

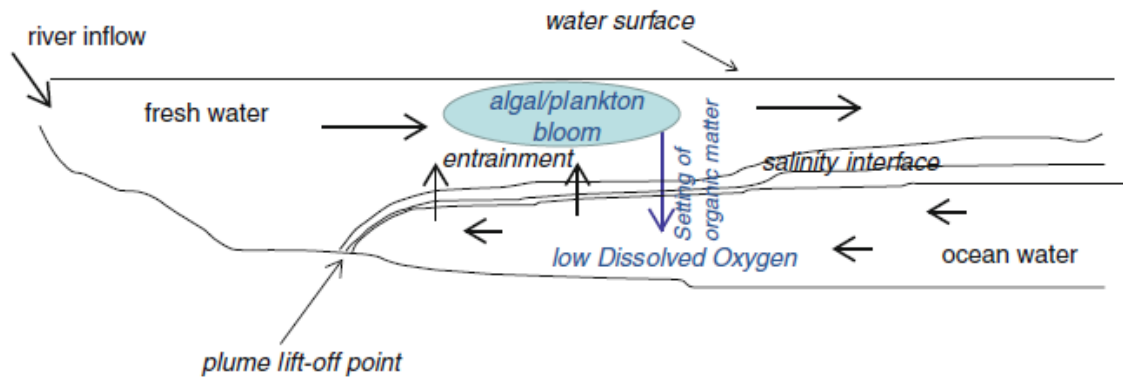


Figure 5.11 – A sketch of the water circulation in a salt wedge estuary. Organic detritus settles from the top layer where it is produced by an algal/plankton bloom. By decaying in the bottom layer this material extracts dissolved oxygen from the water column. Low dissolved oxygen commonly results in the bottom layer. If the inflow rate of dissolved oxygen by oceanic inflow in the bottom layer is smaller than the consumption rate of dissolved oxygen by the decay of organic matter in suspension and on the bottom, anoxia can result.

CHAPTER 6

Using field data for estimating estuarine water transport timescales and the associated return coefficient

Fernando P. Andutta¹, Peter V. Ridd¹, Eric Deleersnijder², David Prandle³

¹ School of Engineering and Physical sciences, James Cook University, Townsville QLD 4811, Australia.

² Université catholique de Louvain, Earth and Life Institute (ELI), Georges Lemaître Centre for Earth and Climate Research (TECLIM), Bte L7.01.11, 2 Chemin du Cyclotron, B-1348 Louvain-la-Neuve, Belgium.

³ National Oceanography Centre, Joseph Proudman Building, 6 Brownlow Street, Liverpool L3 5DA, UK.

This chapter reproduces the following paper:

Andutta, F.P., Ridd, P.V., Deleersnijder, E., Prandle, D. (Submitted). A note on estimating the transport timescales namely water renewal, residence time, exposure time and return coefficient.

Keywords of this chapter: LOICZ model; CART model; water renewal, residence time; exposure time; return coefficient.

The transport timescales of water in an estuary are important quantities to monitor pollution threats to the estuarine ecosystem; we have therefore re-evaluated the application of simple analytical solutions to estimate these time scales. Three transport time scales namely water renewal, residence time and exposure time were calculated using analytical solutions for a range of estuaries worldwide. The analytical results were compared with residence time results from numerical models where estimates were available. The theoretical formulation from the Land Ocean Interaction Coastal Zone model (LOICZ), and a newly proposed modified LOICZ model were used to calculate the water renewal. The residence time and the exposure time were calculated using the Constituent-oriented Age and Residence time Theory (CART). The modified LOICZ

model resulted in the best fit compared to residence time from numerical models, with $r^2 \sim 0.7$. In addition to the proposed modified LOICZ model, a graphic conceptual model, the advection/diffusion timescale diagram was developed, which was used to visualize where different estuaries lie in the advective/diffusive time scale space diagram. Estuaries can be divided into those which are dominated by diffusion, those which are dominated by advection and those where diffusion and advection are of similar magnitude.

6.1 Introduction

The transport timescales of water in an estuary are important quantities to analyse and estimate pollution threats to the estuarine ecosystem (Lucas et al., 2009; McLusky and Elliott, 2004; Wolanski, 2007). There are a number of definitions of transport timescales, namely (1) the flushing time, (2) the age, (3) the residence time, (4) the exposure time, and (5) the renewal time. The flushing time is the time it takes for the passive tracer particles concentration to decrease to $1/e$ (~ 0.37) of its initial value, i.e. the time necessary for $\sim 63\%$ of a concentration to cross the open boundary (Ketchum, 1951; Dyer, 1973; Monsen et al., 2002; Deleersnijder et al., 2006; Valle-Levinson, 2010; Wolanski et al., 2011). The age is the time necessary for a water parcel to move from a defined inlet boundary (e.g. the salinity intrusion limit or the tidal intrusion limit) to another specific location (e.g. the mouth; Monsen et al., 2002). The residence time is generally defined as the time needed for a water particle to first leave the domain of interest (Bolin and Rodhe 1973, Zimmerman 1976, Takeoka 1984). In other words, it is the time necessary for a parcel of fluid to exit a domain for the first time. The residence time therefore varies spatially depending on the starting point and time. In such calculations, once water particles leave the estuary, they are disregarded. In practice however some of those particles may return to the estuary with reversing tidal currents after first exiting the estuary (Monsen et al., 2002). To incorporate this process in a timescale, the exposure time is used, which is the total time spent by a particle inside the aquatic environment (Delhez, 2006; de Brye et al. 2012). The difference between the exposure time and the residence time depends on the circulation in coastal waters; for instance swift longshore currents decrease the difference between the exposure and residence times (Wolanski, 2007). The residence time was earlier

defined as the time needed to replace the volume of the estuary by new water coming both from the ocean and the river (e.g. Dyer, 1973); we propose to call this the renewal time because the definition of residence time has now changed.

These transport timescales (Fig. 6.1) are determined by the hydrodynamics (Monsen et al., 2002; Delhez, 2006; Delhez and Deleersnijder, 2006; Lowe et al., 2009; Wolanski et al. 2011) but their precise values remain elusive because the hydrodynamics comprise both the water circulation, which is generally well known and can usually be modeled reliably, and all of the unresolved process which are generally assumed to amount to turbulent mixing, which are much less known.

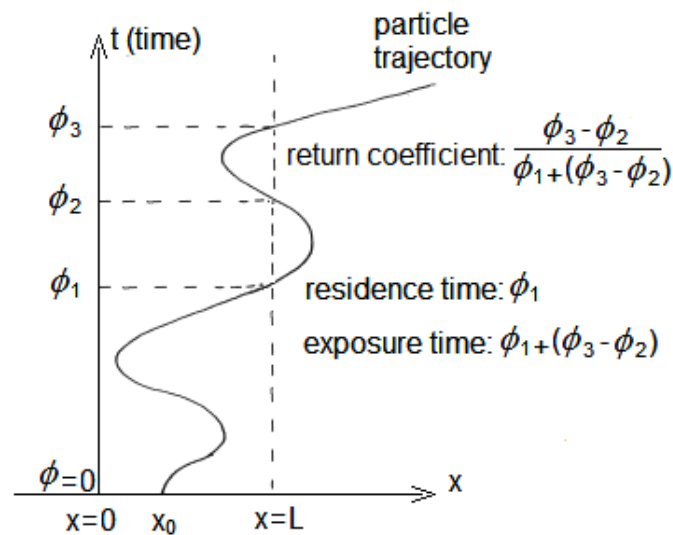


Figure 6.1 – Illustration of the concept of residence and exposure times for a single water particle in the domain between the upstream and downstream open boundaries that are respectively denoted by $x = 0$ and $x = L$. For the particle under consideration, the residence time and exposure time are $\bar{\phi} = t_1$ and $\bar{\Theta} = t_1 + (t_3 - t_2)$, respectively. Timescales related to a single particle are introduced for pedagogical purposes only and actually are physically meaningless.

Estimating these transport timescales in even the simplest 1-D estuarine models has proven to be a challenge to modelers. Considering an estuary located between $x = 0$ (the upstream limit) and $x = L$ (the estuary mouth), the residence time can be estimated from models of the fate of tracers tagging water particles. In the simplest case of cross-

sectional homogeneity and the absence of baroclinic currents, a 1-D model may be sufficient; in that case these tracers have a concentration C that follows the equation

$$\frac{\partial(AC)}{\partial t} + \frac{\partial}{\partial x}(QC) = \frac{\partial}{\partial x}\left(AK \frac{\partial C}{\partial x}\right), \quad (6.1)$$

where $A(x)$ (in m^2) is the cross-sectional area of the estuary, t is the time, x the distance along-channel, Q is the flow rate and K is the along-channel eddy diffusion coefficient. To calculate the residence time the modeler seeds the model with tracers so that $C = 1$ at $t = 0$ everywhere at $0 < x < L$, and solves Equation (6.1) to calculate C as a function of x and t ; from such a solution the various timescales can be calculated. None of these steps however are straightforward. Firstly a hydrodynamic model is needed to provide the data on Q as a function of x and t . Secondly the modeler must also provide a closed-form formula or a model to estimate K as a function of x and t . Thirdly the modeler must specify the open boundary conditions for C at $x = 0$ and $x = L$. To calculate the residence time, the open boundary conditions are simplest, namely $C=0$ at $x = 0$ and $x = L$ (e.g. Delhez and Deleersnijder 2006); to compute the exposure time, the open boundary conditions for C at $x = 0$ and $x = L$ are unknown a priori; the usual practice then is for the modeler to extend the model domain offshore ($x > L$) in 2-D or 3-D at a distance far enough that the estuary does not influence the circulation; the model should also be extended upstream into the river (see e.g. de Brye et al. 2012). In turn this requires knowledge of the coastal circulation, which in turn requires knowledge of the oceanic circulation offshore. In the simplest case, three independent parameters control the transport timescale, the residual velocity $u = Q_R / A$, where Q_R is the river discharge and A the cross-sectional area), the estuarine length L , and the along-channel eddy diffusion coefficient K . Two timescales result therefrom (Fischer et al., 1979), namely an advective timescale $T_1 = L/u = V/Q_R$, and a diffusion timescale $T_2 = L^2/K$. The relative importance of these two timescales is determined by their ratio, which is the Peclet number $P_E = T_2/T_1 = uL/K$. While P_E is used in estuarine classification schemes (Prandle, 2009), so far no formula has been proposed to estimate the residence time of an estuary as a function of P_E . The diffusive timescale T_2 might be expressed as, $T_2 = P_E V/Q_R$, and thus taking into consideration the estuarine volume.

In view of these complexities, modelers have moved away from analytical solutions and have increasingly used numerical models in 2-D and 3-D. Such models are elegant, but they still carry uncertainties in term of the hydrodynamic conditions and the fate of tracers at the open boundaries as well as in quantifying the turbulent diffusion. Although there are an increasing number of physical oceanographers modelling estuaries, only for a few estuaries have the residence time been estimated using calibrated numerical models, while simple box modes have been applied to over 200 estuaries.

In view of this we propose to re-evaluate the usefulness of 1-D and box estuarine models. Historically, simple zero-dimension box models were proposed to estimate what used to be called the residence time (Swaney et al., 2011), and which is now termed the renewal time defined as the replacement time of the estuarine volume V . Probably the two best known such models are the tidal flushing model and the gravitational circulation model. The tidal flushing box model assumes that the estuary is flushed at each tidal cycle by the tidal prism V_p , i.e. the amount of water that exits the estuary at ebb tide (Ketchum, 1951; Figure 6.2b). Thus, a fraction r of the estuary water is renewed by ocean water at each tidal cycle,

$$r = V_p / V. \quad (6.2)$$

The renewal time T was calculated as

$$T = \tau / r, \quad (6.3)$$

where τ is the tidal period (e.g. 0.5 d for solar semi-diurnal tide and 1 d for solar diurnal tide).

In an attempt to provide information on the along-channel variation of the renewal time, this model was later improved by segmenting the estuary and assuming that the water volume exiting a segment at ebb tide completely replaces the water in the downstream segment (Wood, 1979). Such models do not account for the baroclinic circulation typical of partially mixed estuaries (Figure 6.2c). The gravitational circulation model focused on this baroclinic circulation and calculated the renewal time as the ratio between the volume of water and the inflow rate, this inflow rate being the

sum of the oceanic inflow of water plus the riverine inflow (Figure 6.2c; Dyer, 1973); tidal mixing was neglected and the oceanic inflow was calculated from the continuity equations for water and salt. This solution leads to an estimate of the renewal time T (Hansen and Rattray, 1965; Dyer, 1973; Wolanski, 2007)

$$T = V / \{ Q_R (1 - S_R / S_o) \}, \quad (6.4)$$

where Q_R is the river discharge, S_R is the salinity of the estuarine outflow, and S_o is the salinity of the oceanic inflow in the estuary. Field data suggest that T decreases with increasing tide range and increase with increasing length of the estuary (Uncles et al., 2002).

Both these box models suffer from neglect of either the baroclinic circulation or the tidal mixing. To avoid this pitfall, the LOICZ model (Smith et al., 2005 and 2010; Crossland et al., 2005; Swaney et al., 2011) includes both advective and diffusive transports (Figure 6.2d); rainfall, groundwater and evaporation can also be added if needed. For a vertically well-mixed estuary, oceanic waters enter the estuary at a rate Q_D that is calculated from a salt balance as follows. This oceanic inflow brings salinity that exceeds the estuarine salinity S_R by an amount ΔS ; there is a balance between the advection and diffusion of salt, so that at steady-state from salt-balance equation (Fisher et al., 1979),

$$Q_D \Delta S = Q_R S_R, \quad (6.5)$$

where Q_D is defined as the exchange flux between the estuary and the coastal areas. The LOICZ method assumes that

$$S_R = 0.5 (S_O + S_E) \quad (6.6)$$

is the mean salinity in the outer estuary, and

$$\Delta S = (S_O - S_E) \quad (6.7)$$

Where S_O and S_E are the salinity in coastal waters and the estuary respectively.

The water inflow rate in the estuary is thus equal to $Q_R + Q_D$; this same water flux leaves the estuary; thus the renewal time T_{LOICZ} is,

$$T_{LOICZ} = V / (Q_R + Q_D). \quad (6.8)$$

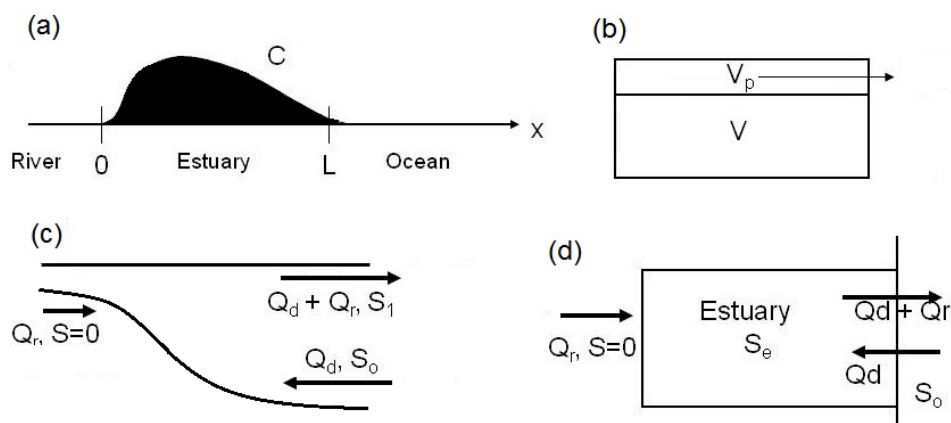


Figure 6.2 – (a) A 1-D estuary model; (b) the tidal prism box model (side view); (c) the gravitational circulation box model (side view); (d) the LOICZ box model for a vertically well-mixed estuary (plan view).

The LOICZ box model is simple and easy to use and has been applied to about 200 estuaries worldwide (Swaney et al., 2011). However box models only capture part of the physics and they give no information on the spatial distribution of the renewal time in the estuary. To obtain such spatial information, it is necessary to use numerical models, but a drawback of this approach is that it quite commonly requires the modeller to assume values of the turbulent diffusion coefficient, which is often unknown *a priori*.

In this paper, results of a few timescales definitions were calculated using simple formulations, and then compared against residence time results calculated using numerical models for a few estuaries where data was available. The estimated times of water renewal calculated using a modified LOICZ were compared with results from the LOICZ model (Gordon et al., 1996; Yanagi, 2000; Smith et al., 2005; Breitburg et al., 2009; Smith et al., 2010; Swaney et al., in press). The LOICZ model has very similar assumptions to derive the modified LOICZ model, which include the representation of the estuarine concentration by a single value. The mean residence time and the mean exposure time were calculated using CART's theory (Constituent-oriented Age and

Residence time Theory). In addition to the comparison of these methods to estimate timescales, we have also applied a new advection/diffusion diagram that quantifies the relative contribution to water from the advective and diffusive timescales.

6.2 The LOICZ model

The LOICZ model includes both advective and diffusive transport. The diffusive transport is calculated as an exchange flow between the estuary and coastal waters. This exchange flow is calculated by assuming the salinity gradient in the seaward half of the estuary, i.e. from the estuarine mouth ($x = L$) to $x = L/2$, and considering geometric features of the estuary, sewage, groundwater, rainfall, evaporation, freshwater runoff, and the salinity in the estuary and in coastal waters. Neglecting rainfall, evaporation, sewage and groundwater inflows, the LOICZ box model calculates the average residence time T_{LOICZ} as

$$T_{LOICZ} = V/(Q_R + Q_D) = V/(Q_R + Q_R S_R/(S_O - S_E)), \quad (6.9)$$

Using Eqs.6.5 and 6.6, Eq. 6.9 becomes

$$T_{LOICZ} = \frac{V}{Q_R + Q_R \underbrace{\frac{0.5(S_E + S_O)}{S_O - S_E}}_{\text{exchange flow}}}. \quad (6.10)$$

The LOICZ model depends on good measurements of the salinity at the boundaries to estimate properly the exchange flow (Q_D). The basic assumptions associating Q_D with the salinity balance may be invalid if the salinity gradient is too small (Swaney et al., in press).

Eq. 6.10 may be written as,

$$T_{LOICZ} = \frac{VL}{Q_R L + \left(\frac{0.5(S_E + S_O)}{S_O - S_E} \right) Q_R L}. \quad (6.11)$$

From the salinity balance equation of Fisher et al. (1979) and assuming the salinity at the mouth $S(L)$ to be $S(L) \approx S_O$,

$$Q_R L = AK^{LOICZ} \frac{(S_O - S_E)}{0.5(S_O + S_E)} \quad (6.12)$$

where K^{LOICZ} is the diffusion coefficient applied in the salinity balance in the LOICZ model, and A is the mean cross-sectional area. From Eqs.6.11 and 6.12

$$T_{LOICZ} = \frac{VL}{Q_R L + AK^{LOICZ}}. \quad (6.13)$$

In Eq. 6.11 the influence of the diffusive timescale to the water renewal is parameterized by γ_{LOICZ} , which is defined as

$$\gamma_{LOICZ} = \left[\frac{0.5(S_E + S_O)}{S_O - S_E} \right]. \quad (6.14)$$

Defining the advective and diffusive timescales, Fisher et al. 1979, as before, i.e.

$$T_1 = \frac{V}{Q_R}, \quad \text{and} \quad T_2^{LOICZ} = \frac{L^2}{K^{LOICZ}}. \quad (6.15)$$

Eqs.6.13 and 6.15 become

$$\frac{1}{T_{LOICZ}} = \frac{1}{T_1} + \frac{1}{T_2^{LOICZ}}. \quad (6.16)$$

To our knowledge, Eq. 6.16 has not been previously derived for the LOICZ model.

6.3 The modified LOICZ model

For the modified LOICZ model, we are proposing a modified exchange flow that takes into consideration the Fisher's formula to estimate the mixing rate between the estuary and the coastal zone. The along-channel eddy diffusion coefficient K can be estimated from salinity data using along the whole estuary L (Fischer et al., 1979). K can be estimated from the salinity equation balance because all the other terms in that equation can be measured. There are other methods to estimate K from salinity measurements, e.g. that of Hansen and Rattray (1965) that involves choosing values of K to fit to the observed distribution of salinity with the analytical solution.

It results that

$$Q_d = KA/L, \quad (6.17)$$

and thus,

$$Q_d (S_O - S') = Q_R S_E, \quad (6.18)$$

where S' is in the range $0 \leq S' < S_E$, and here S' is defined at the upstream end of domain under consideration, which depends upon the estuarine segment length L . The length L might be shorter than the length of the maximum salinity intrusion, but cannot exceed the maximum salinity intrusion, otherwise it would lead to a misapplication of the model. It can be shown from the comparison between Eqts. (6.5-6.6) and Eq (6.18) that the LOICZ method uses a larger exchange flow than the modified LOICZ model. It is thus proposed to use Eq. (6.18) as the basis of the modified LOICZ model. The proposed water renewal time T_P is,

$$T_P = \frac{VL}{(Q_R L + AK)} = \frac{VL}{Q_R L + \left(\frac{S_E}{S_O - S'}\right) Q_R L} = \frac{V P_E}{Q_R (1 + P_E)}, \quad (6.19)$$

where $P_E = u L/K$ is the Peclet number, and

$$\gamma_P = S_E / (S_O - S'), \quad (6.20)$$

γ_p determines the contribution to water renewal from the diffusive timescale, which is calculated differently from γ_{LOICZ} in the LOICZ model (Eq. 6.14). Using the diffusive and advective timescales, Equation 6.19 thus becomes,

$$\frac{1}{T_p} = \frac{1}{T_a} + \frac{1}{T_b}, \quad (6.21)$$

Where $T_a = V/Q_R$ and $T_b = VP_E/Q_R$ are the advective and diffusive timescales calculated using the river flow Q ($\text{m}^3 \text{s}^{-1}$). The contribution of advection to the total water renewal, θ ($0 \leq \theta \leq 1$), and defined as

$$\theta = T_p/T_a = Q_R/(Q_R + Q_d) \quad (6.22)$$

6.4 The difference between the water renewal time calculated from the LOICZ model and the modified LOICZ model

It can be seen that there are some differences between the original formula used in the LOICZ model and the newly modified LOICZ model. This is parameterized by $\gamma = \gamma_{LOICZ} / \gamma_p$ that determines ratio between the exchange flow in the LOICZ model (Officer, 1980; Swaney et al., in press) and the suggested new method. From a linear salinity gradient along an estuary, the salinity at the mouth and at the maximum salinity intrusion obeys $S_o = 2S_E$ and $S' = 0$, and thus the ratio $\gamma / \gamma_p = 3$. Therefore, for a nearly linear salinity distribution along an estuary, the diffusive timescales for the LOICZ model is expected to be three times larger than the modified LOICZ model. The description of the salinity balance used to calculate the so called exchange flow in the LOICZ model is described in (Fig. 6.3).

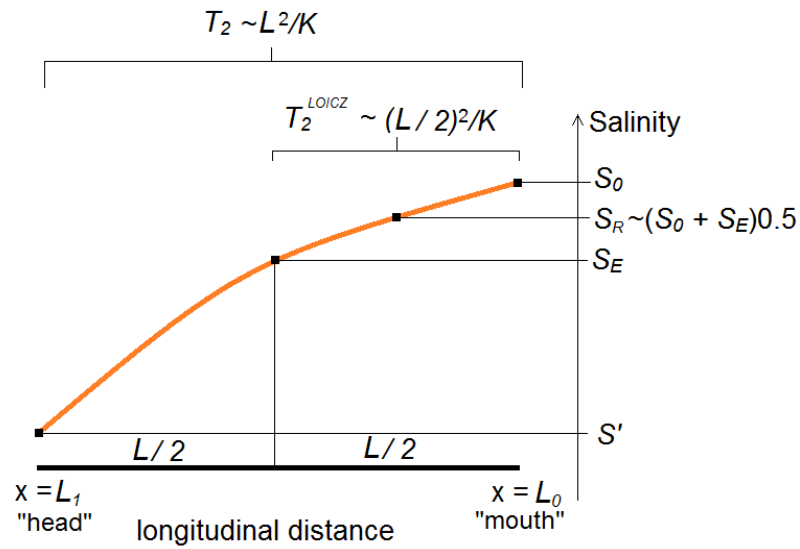


Figure 6.3 – Conceptual description of a generic salinity distribution along an estuary from ($x = L_1$) to the mouth ($S = L_0$). The salinity S' at $x = 0$ where ($0 \leq S' < S_E$).

In the LOICZ model the exchange flux is calculated slightly differently from what has been proposed by Fisher et al. (1979), see Figure 6.3. The exchange flow from the LOICZ model is calculated using the salinity balance from $x = L/2$ to the mouth. It is suggested in this paper the application of the Fisher's formula, i.e. $Q_d = AK/L$ ($m^3 s^{-1}$) that is used in our approach, which can be calculated using measurements of the salinity in the estuary. This exchange flux Q_d is now accounting for the diffusive process at steady state along the whole estuarine segment of length L .

To compare the contribution to water renewal from the river discharge and the exchange flow, we assume a linear variation of the along channel salinity gradient, $S_E = 0.5S_0$ and $S' = 0$, then equations 6.11 and 6.19 become respectively,

$$T_{LOICZ} = \frac{V}{Q_R + \underbrace{1.5Q_R}_{\text{exchange flow}}}, \quad (6.23)$$

and

$$T_P = \frac{V}{Q_R + \underbrace{0.5Q_R}_{\text{exchange flow}}}, \quad (6.24)$$

From Eq. 6.23 the exchange flow in the LOICZ formulation is much larger than the exchange flow for the modified models (Eq. 6.24), and comparing with the advective term we observe that for the LOICZ, the exchange flow contribution to water renewal is 50% larger than river discharge contribution. Conversely, Eq. 6.24 gives an exchange flow contribution that is half of the advective term.

6.5 The CART analytical model

The time scales namely residence time and the exposure time are provided by the Constituent oriented Age and Residence time Theory (CART, www.climate.be/cart), these time scales will be applied hereinafter to a one-dimensional flow, and then compared to the water renewal timescale and compared to results of the residence time for estuaries where estimates were available.

Consider an infinite pipe ($-\infty < x < \infty$) in which there is a steady-state, one-dimensional flow whose river inflow is Q_R . For the problem under consideration, CART's residence time $\phi(x)$ is the average time that an arbitrarily large number of water particles originally located at a distance x from the upstream boundary of the domain of interest ($x=0$) need to hit for the first time one of the open boundaries of the domain of interest, i.e. $x = 0$ or $x = L$, Figure 6.1).

Hydrodynamic timescales

The dimensional parameters characterizing the problem under consideration are L , U and K . From these, only two independent timescales can be built. They are usually taken to be the T_1 and T_2 . They represent the time needed to travel the distance L at velocity U and the time needed for diffusive processes characterized by diffusivity K to alter significantly the concentration field of a passive tracer over the distance L . The advective T_1 and diffusive T_2 time scales are not by themselves a water renewal or residence time timescale. Nonetheless, in accordance with Buckingham's π -theorem (Hanche-Olsen, 2004), a transport time scale for characterizing the rate at which water mass or a tracer concentration is renewed in an estuary the segment under consideration is necessarily a function of these timescales (i.e. T_1 and T_2). This theorem, i.e. Vaschy–

Buckingham π , demonstrates how to compute dimensionless parameters from the given variables, even for an equation whose form is unknown.

CART's pointwise timescales and return coefficient

For the problem under consideration, CART's residence time $\phi(x)$ is the average time that an arbitrarily large number of water particles to firstly exit the system under consideration (Figure 6.1). According to Delhez et al. (2004) and Delhez and Deleersnijder (2006), the residence time defined in such a way obeys,

$$\phi(x) = \frac{V}{Q_R} \left(1 - \frac{x}{L}\right) + \frac{V}{Q_R} \left(\frac{e^{-P_E} - e^{-P_E x/L}}{1 - e^{-P_E}} \right) \quad (6.25)$$

After hitting an open boundary of the domain, a particle may re-enter the domain at a later stage (e.g. Spivakovskaya, et al. 2007, Delhez and Deleersnijder, 2010). This is not accounted for by the residence time defined above, for every water particle is disregarded as soon as it hits an open boundary of the domain of interest. To address this issue, the concept of exposure time has been introduced (Monsen, et al. 2002, Delhez, et al. 2004, Delhez, 2006).

CART's exposure time $\Theta(x)$ is the average time that an arbitrarily large number of water particles initially located at coordinate x spend in the domain of interest (Figure 6.1). While the residence time is defined in the domain of interest only, the exposure may be estimated both in the domain of interest and its environment — because one cannot rule out that particles originally located outside the domain of interest eventually spend some time in it. CART's exposure time satisfies (Figure 6.4):

$$-\infty < x \leq 0 \quad : \quad \Theta(x) = \frac{V}{Q_R} \quad (6.26a)$$

$$0 \leq x \leq L \quad : \quad \Theta(x) = \frac{V}{Q_R} \left(1 - \frac{x}{L}\right) + \frac{V}{Q_R} \left(\frac{1 - e^{-P_E x/L}}{P_E} \right) \quad (6.26b)$$

$$L \leq x < \infty \quad : \quad \Theta(x) = \frac{V}{Q_R} \left(\frac{e^{P_E} - 1}{P_E} e^{-P_E x/L} \right) \quad (6.26c)$$

Figure 6.4 displays the profile of the residence and exposure time for various values of the Peclet number. For high values of the latter, the boundary layer for the concentration C is developed in the vicinity of the upstream boundary of the domain (Delhez and Deleersnijder 2006, Blaise et al. 2010). The cause thereof may be summarized as follows: the greater the relative importance of advection, the less likely it is for diffusion to cause a water particle to hit the upstream boundary of the domain ($x = L$). In accordance with elementary physical intuition, the exposure time defined previously is larger than the residence time in the domain of interest ($0 \leq x \leq L$).

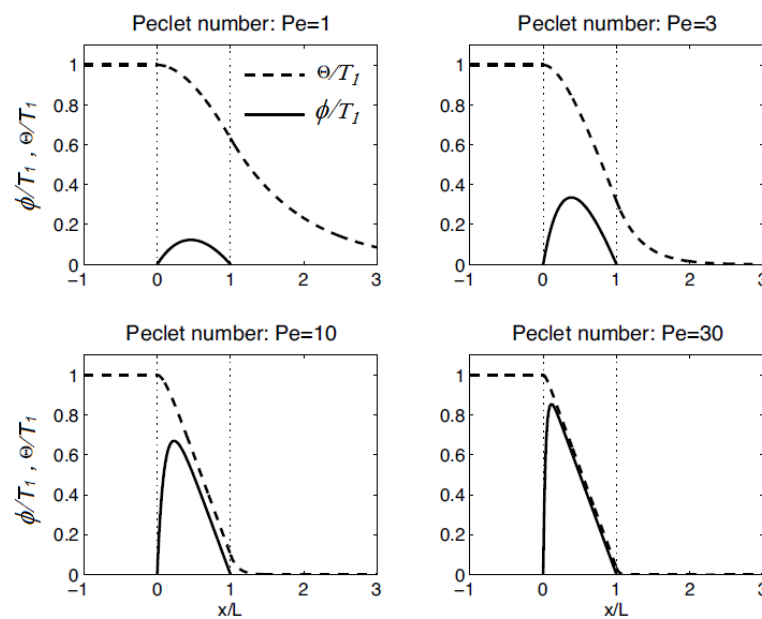


Figure 6.4 – Representation of the residence time ϕ (solid curve; Eq. 6.25) and the exposure time Θ (dashed curve; Eq. 26a,b,c) as a function of the distance x to the upstream boundary of the domain of interest. The timescales are normalised by means of the advective timescale T_I . Various values of the Peclet number are considered: the larger this number, the larger the relative importance of advection and, hence, the smaller the difference between the exposure time and the residence time. It is noteworthy that the exposure time, as opposed to the residence time, is defined outside the domain of interest ($0 \leq x \leq L$).

It is appropriate to assess the propensity of water particles to return into the domain of interest after hitting for the first time one of its open boundaries. For doing so, the approach of Arega et al. (2008) and de Brauwere et al. (2010) is selected. It leads

to an appealing dimensionless number that is termed herein “return coefficient” and is defined to be

$$r(x) = \frac{\Theta(x) - \phi(x)}{\Theta(x)}. \quad (6.27)$$

The values of this coefficient (Eq. 6.26) lies in the interval [0,1]: the larger its value, the more likely it is for water particles to re-enter the domain of interest after hitting for the first time one of its open boundaries. Accordingly, particles that never return into the domain are characterized by a zero return coefficient, while particle returning very, very often are associated with a value of r that is close to unity (Fig 6.5).

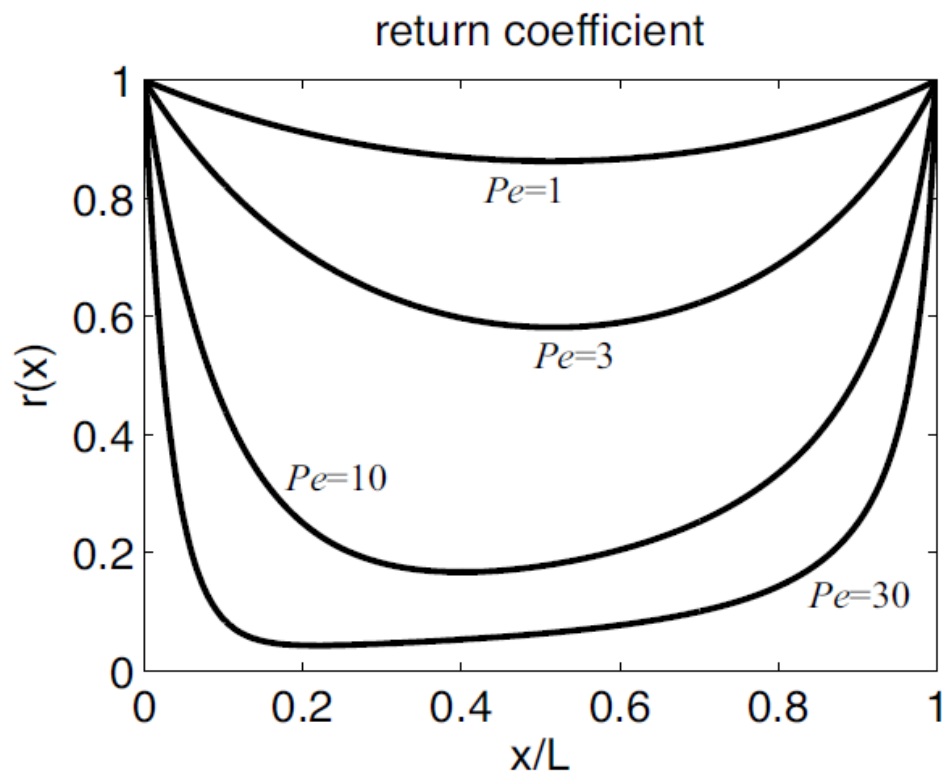


Figure 6.5 – Representation for various values of the Peclet number of the return coefficient as defined by formula (6.26).

From Eqts.6.24 and 6.25, the domain-averaged residence time and exposure times obey the relations,

$$\bar{\phi} = \frac{V}{Q_R} \left(\frac{1}{2} \right) + \frac{V}{Q_R} \left(\frac{1}{e^{P_E} - 1} - \frac{1}{P_E} \right) \quad (6.28)$$

and

$$\bar{\Theta} = \frac{V}{Q_R} \left(\frac{1}{2} \right) + \frac{V}{Q_R} \left(\frac{1}{P_E} - \frac{1 - e^{-P_E}}{P_E^2} \right). \quad (6.29)$$

These global timescales can also be regarded as the residence and exposure times of an arbitrarily large number of water particles that initially are uniformly distributed over the domain of interest. $V/2Q_R$ in Eqts. 6.27 and 6.28 is the mean advective timescales $\bar{\phi}_a$ and $\bar{\Theta}_a$, while the second term $\bar{\phi}_b$ and $\bar{\Theta}_b$ causes respectively the decrease and increase to the final residence time and exposure time.

6.6 Results and discussions

The CART model, the LOICZ model and a newly modified LOICZ model were applied to the estuaries (Appendix 1 to 7), namely the Curimataú, Caravelas and Peruípe estuaries in Brazil (Miranda et al., 2005 and 2006; Andutta et al., 2006), the York River and Hudson estuaries in the USA (Sandifer, 1973; Haas, 1977; Shen and Haas, 2004; Warner et al., 2005 and 2010), the Conwy and Mersey estuaries in the UK (Bowden, 1971; Turrell et al., 1996; Wu et al., 2005), and the Scheldt in France-Belgium-Netherlands (de Brauwere et al., 2011). The results water renewal time were estimated using the LOICZ model and the modified LOICZ model, while the CART theory was applied to estimate the mean residence time and exposure time.

From Table 6.1 it can be seen that the water renewal calculated by the LOICZ method are always shorter compared to results from the modified LOICZ model T_p , and the latter usually compare well with the exposure times calculated by the CART analytical model (see Table 6.2). Results from the LOICZ model are shorter than the

modified LOICZ model because of the larger diffusion coefficient applied in this model (explained in section 6.4).

In the Hudson River the water renewal at neap tides ranges between 6.3 and 7.8 days for T_P , and ranges between 4.3 and 5.3 days using the LOICZ model. This difference for T comes from the diffusion timescale component which for the Hudson estuary at neap tides, ranges from 31.4 – 43.0 days for the modified LOICZ, and ranges between 9.4 – 12.1 days using the LOICZ model. This difference in the diffusion timescales depends upon on the diffusive coefficient K , which was estimated for the Hudson Estuary in the range between 1880 to 2404 m s^{-2} , and 545 to 828 m s^{-2} for the LOICZ and the modified LOICZ, respectively. Results of water renewal and the exposure time from CART formula compare favourably, though are slightly underestimating, with the numerical results for the Hudson Estuary (Warner et al., 2010), namely a mean residence time for neap tides of ~ 8 -10 days and for spring tides ~ 8 -9 days.

The water renewal time is a combination of the advective and diffusive timescales, and the difference between T_P and T_{LOICZ} depends on the factor γ (see Eqts. 6.14 and 6.20), especially when the advective timescale is relatively large compared to the diffusive timescale, and thus the diffusive timescales dominates the renewal time. For the Mersey estuary, the advective timescale is very long compared with the diffusive timescale, and the water renewal calculated by the LOICZ model is considerably reduced compared to the modified LOICZ model (see in Table 6.1, T_{LOICZ}/T_P). Conversely, for the Hudson estuary during neap tides the fresh water discharge is important and thus the advective timescale is smaller compared to the diffusion timescale, T_{LOICZ} approaches T_P (see in Table 6.1, T_{LOICZ}/T_P).

The CART's residence time resulted in values mostly smaller than the results of water renewal calculated using the LOICZ model and our method. In contrast, CART's exposure time always is larger than the residence time; this is due to the way the timescales are defined/constructed). CART's exposure time is however more comparable to the water renewal time. Larger exposure times result from the small values of the Peclet number (Table 6.2). Therefore, high values of Peclet number indicate that although particles may reach the open boundary quickly, they may return to the system for long period (e.g. Curimataú, Caravelas, Peruípe and Mersey estuaries).

The results of those three different approaches (i.e. T_P , T_{LOICZ} and CART's formula) were compared against available numerical results (Table 6.2) for the Hudson Estuary (Warner et al., 2010), Caravelas and Peruípe estuaries (Andutta, 2011, Andutta and Miranda 2011, submitted), the Mersey Estuary (Yuan et al., 2007), the Scheldt Estuary (de Brauwere et al., 2011; de Brye et al., 2012), and the York River Estuary (Shen and Haas, 2004). The models had been previously calibrated/validated with salinity measurements and, hence, may be assumed to reproduce rather well advective and diffusive transport phenomena in the domains in which they were used.

The numerical results from (Warner et al., 2010) showed that for the Hudson Estuary (within 45 km of the mouth) a mean residence time for neap tides was ~8-10 days and for spring tides was ~8-9 days. The results calculated for T_P (see Table 6.1) are slightly lower than the numerical model results for neap tides and relatively close for spring tides (i.e 6.3-7.8 days for neaps and 7.9-9.8 for springs). As mentioned previously the LOICZ model for the Hudson Estuary yields a water renewal (~5 days) *ca.* 40% lower. For the Caravelas and Peruípe estuaries in Brazil, the residence time calculated from numerical models varied in the ranges 4.2-10.3 and 1.5-2.5 days, respectively. For the Mersey and Scheldt estuaries the residence time varies between 0.7-4 and 5-70 days, respectively. For the York River Estuary, the residence time varies between 11.3-33.3 and 18.1-59.3 days for high and mean flow, respectively. Aside from results from the Mersey Estuary, these results from numerical models were compared well with the water renewal estimates using the modified LOICZ, and slightly higher than the results of water renewal using the original LOICZ model, and the residence time calculated by the CART's formula.

Table 6.1 – Water renewal timescale (days) of the Curimataú, Caravelas, Peruípe, Hudson, Conwy, Scheldt and York estuaries. For the Curimataú Estuary, A denotes the diffusion timescale using horizontal diffusion calculated from Fisher’s formula while B uses Hansen-Rattray’s formula. The advection contribution to water renewal is $\theta = T_p / T_a$ and $\theta_{LOICZ} = T_{LOICZ} / T_2^{LOICZ}$. The diffusion coefficient k^{LOICZ} was estimated using Eq. 6.12, i.e. $K^{LOICZ} = L Q_R 0.5(S_O + S_E) / A(S_O - S_E)$, and k was estimated using equations 6.17 and 6.18 combined, i.e. $K = L Q_R S_E / A(S_O - S')$.

Curimataú Estuary (C)										
Conditions	T_2	T_2^{LOICZ}	T_1	T_p	T_{LOICZ}	T_{LOICZ} / T_p	Θ	Θ_{LOICZ}	$k (m^2 s^{-1})$	$k^{LOICZ} (m^2 s^{-1})$
(A) neap tides	2.4-4.7	0.5-1.0	1.4-2.4	0.9-1.6	0.5-0.9	0.55-0.56	0.64-0.67	0.36-0.38	245-480	735-1600
(B) neap tides	2.3-4.6	0.5-1.0	1.4-2.4	0.9-1.6	0.5-0.9	0.55-0.56	0.50-0.67	0.36-0.38	250-500	-
(A) spring tides	1.8-3.3	0.5-1.4	4.3-7.1	1.2-2.2	0.5-1.4	0.38-0.64	0.30-0.31	0.11-0.20	352-656	653-2267
(B) spring tides	1.7-2.7	0.5-1.4	4.3-7.1	1.2-2.0	0.5-1.4	0.42-0.70	0.27-0.28	0.11-0.20	435-700	-
Caravelas Estuary (CA)										
neap tides	9.5-70.5	3.2-45.8	55.6-388.9	8.1-59.7	3.0-40.9	0.37-0.69	0.14-0.15	0.05-0.11	24-179	37-552
spring tides	7.2-51.9	3.0-32.7	55.6-388.9	6.4-45.8	2.9-30.2	0.45-0.66	0.11-0.12	0.05-0.08	31-227	49-525
Peruípe Estuary (PE)										
neap tides	1.8-4.4	0.3-2.7	2.3-13.9	0.5-3.3	0.3-2.3	0.60-0.70	0.22-0.24	0.13-0.17	66-427	107-1035
spring tides	0.3-1.7	0.1-1.4	2.3-13.9	0.2-1.5	0.1-1.2	0.50-0.80	0.09-0.11	0.04-0.09	173-1071	212-1938
Hudson Estuary (H)										
neap tides	31.4-43.0	9.4-12.1	7.9-9.5	6.3-7.8	4.3-5.3	0.68-0.71	0.80-0.82	0.53-0.54	545-745	1935-2484
spring tides	36.8-28.3	9.7-12.5	11.0-13.3	7.9-9.8	4.2-5.2	0.53-0.54	0.72-0.74	0.38-0.39	637-828	1880-2419
Conwy Estuary (CY)										
neap tides	157.5-175	49.5-54.9	89.9-98.7	56.8-63.1	31.8-35.3	0.55-0.56	0.63-0.64	0.35-0.36	9.5-10.4	30.25-32.95
spring tides	100-111.2	36.7-40.7	120.7-134	54.8-60.8	28.1-31.2	0.51-0.52	0.45-0.46	0.23-0.24	14.9-16.3	40.63-44.27
Mersey Estuary (M)										
Average conditions	4.9-13.4	1.9-7.6	27.4-72.4	4.2-11.3	1.8-6.9	0.43-0.61	0.16-0.17	0.07-0.10	304-1070	534-2771
Scheldt Estuary (S)										
Average conditions	146-207	9.7-26.8	161-214.4	76.4-105.4	9.2-23.8	0.12-0.23	0.47-0.49	0.06-0.11	581-826	2996-9268
York River Estuary										
high flow	45.0-81.0	17.7-36.0	109.3-161.9	31.9-54.0	15.2-29.9	0.48-0.55	0.28-0.33	0.14-0.18	316-568	974-1053
mean flow	112.2-201.9	44.2-89.8	272.6-403.9	79.5-134.6	38.0-73.4	0.48-0.54	0.29-0.33	0.14-0.18	127-228	390-422

Table 6.2 – The mean residence time ($\bar{\phi}_{CART}$ in days), mean exposure time ($\bar{\Theta}_{CART}$ in days), and the return coefficient of the Curimataú, Caravelas, Peruípe, Hudson, Conwy, Mersey, Scheldt and York estuaries. The Peclet number $P_E = u L/K$ was calculated using the diffusion coefficient K from Fisher's formula (see caption of Table 6.1), which was used in our method. $\bar{\phi}_a$ and $\bar{\Theta}_a$ correspond to the mean advective timescale in the residence time and exposure time, respectively.

Curimataú Estuary (C)								
Conditions	P_E	$\bar{\phi}_a$ and $\bar{\Theta}_a$	$\bar{\phi}_b$	$\bar{\Theta}_b$	$\bar{\phi}_{CART}$	$\bar{\Theta}_{CART}$	Return coefficient	Residence time from Numerical Model
neap tides	1.02-3.27	0.7-1.2	-0.6	0.5	0.1-0.6	1.2-1.7	0.65-0.92	-
spring tides	0.25-0.76	2.2-3.6	-2.1 to -3.1	2.0-2.8	0.1-0.5	4.1-6.4	0.92-0.98	-
Caravelas Estuary (CA)								
neap tides	0.02-1.25	27.8-194.5	-158.0 to -27.7	27.6-137.2	0.1-36.3	55.4-331.7	0.89-0.99	4.2-10.3
spring tides	0.02-0.98	27.8-194.5	-163.2 to -27.7	27.6-143.9	0.1-21.3	55.4-338.3	0.89-0.99	
Peruípe Estuary (PE)								
neap tides	0.04-1.47	1.7-7.0	-5.3 to -1.1	1.1-4.5	0.1-1.6	2.3-11.5	0.86-0.96	1.5-2.5
spring tides	0.02-0.56	1.7-7.0	-6.3 to -1.2	1.1-5.8	0.1-0.7	2.3-12.8	0.86-0.95	
Hudson Estuary (H)								
neap tides	3.32-5.47	4.0-4.8	-2.1 to -1.6	1.4-1.7	1.9-3.1	5.4-6.2	0.50-0.65	8-10
spring tides	2.13-3.34	5.5-6.7	-3.5 to -3.7	2.9-3.0	1.8-3.2	8.5-9.6	0.67-0.79	8-9
Conwy Estuary (CY)								
neap tides	1.62-1.93	45.0-49.4	-34.4 to -33.3	28.0-28.5	11.6-15.0	73.0-77.9	0.81-0.84	-
spring tides	0.76-0.91	60.4-67.0	-57.0 to -52.8	47.6-50.6	7.6-10.0	107.9-117.6	0.92-0.93	-
Mersey Estuary (M)								
Average conditions	0.16-0.21	13.7-36.2	-20.0 to -43.7	19.5-63.9	0.6-1.6	40.0-109.2	0.98-0.99	1-6.3
Scheldt Estuary (S)								
Average conditions	0.91-0.97	80.5-107.2	-90.1 to -68.5	60.8-79.5	12.0-17.1	141.3-186.7	0.91-0.92	5-70
York River Estuary								
high flow	0.28-0.74	54.7-81.0	-52.1 to -71.1	49.9-64.2	2.5-9.9	104.5-145.1	0.93-0.98	11.3-33.3
mean flow	0.28-0.74	136.4-201.9	-130 to -177.3	124.4-160.1	6.3-24.7	260.7-362.1	0.93-0.98	18.1-59.3

The modified LOICZ model resulted in the best fit against results of the average maximum residence time from numerical models (Fig. 6.6a), with $r^2 \sim 0.7$. The slope calculated is 0.52, and thus indicating that the modified LOICZ model yields timescales slightly larger than residence time from numerical models. Although the compared results have a slightly different definition, this method offers a simple way to estimate easily the residence time for which minimal oceanographic data is available (i.e. geometry, river discharge and salinity measurements).

The scatter plot of the original LOICZ model plotted against the results from numerical models (not shown), resulted the $r^2 \sim 0.20$, while the residence time and the time of exposure from CART's formulation resulted in the r^2 smaller than 0.20.

The diffusive contribution to water renewal (i.e. $1 - \theta$) has shown a good exponential correlation against results of the return coefficient (Fig. 6.6b), with $r^2 = 0.85$. Thus indicating that estuaries dominated by diffusion may have long period of return of water particles.

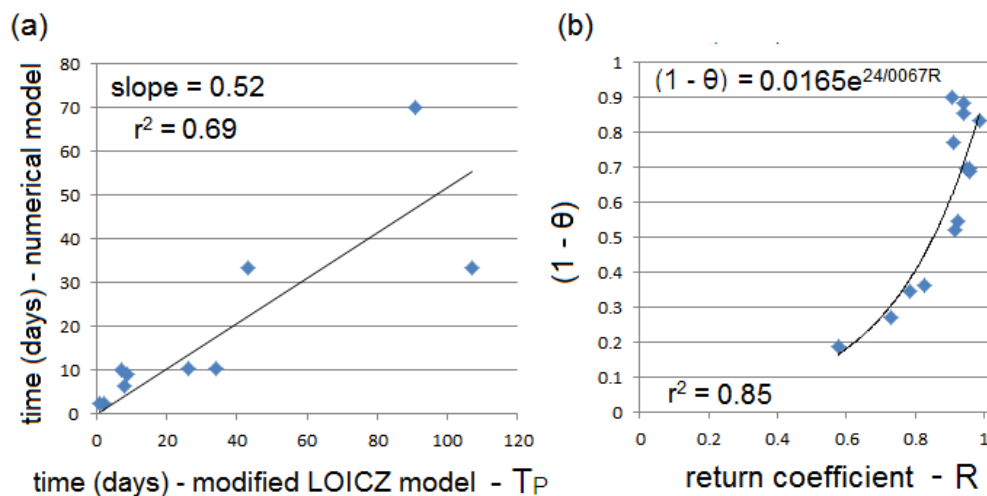


Figure 6.6 – (a) Scatter plot of the water renewal timescale T_p against the maximum residence time from hydrodynamic numerical models. (b) Scatter plot of the diffusive contribution to water renewal $(1 - \theta)$ against the return coefficient calculated using CART's formula. Data from all estuaries in table 6.2 aside from Curimataú and Conwy estuaries.

The relative contribution to water renewal; from the advective and diffusive processes for a particular estuary can be visualized in the Advection-Diffusion Diagram

(Figure 6.7) which is generated using equations 6.21 and 6.22. It can be seen that for the Curimataú Estuary diffusion dominated over advection at spring tides, while advection dominated over diffusion at neap tides. The absolute, but not the relative, estimates of these timescales varied somewhat depending on which of the two methods of estimating K was used (e.g. Hansen-Rattray's or Fisher's formula). For the Hudson Estuary, during both tides neap and spring tides the water renewal was predominantly caused by advection, $0.72 < \theta < 0.82$. In the Conwy Estuary there was a slight dominance of advection during neap tides $\theta \sim 0.63$ and of diffusion during spring tides $\theta \sim 0.45$. For the Mersey, York, Caravelas and Perúípe estuaries diffusion dominated over advection (*ca* $\theta < 0.50$), while for the Scheldt Estuary advection and diffusion contributes nearly the same for water renewal $\theta \sim 0.50$.

In the Conwy Estuary where the river inflow was nearly constant, from neap to spring tides the relative contribution of diffusion increased at spring tide, as diffusion increases with increasing values of the ratio of the tidal oscillation (R) over the mean depth (h), i.e. R/h (Uncles et al., 2002). This effect might be more apparent if the advective timescale due to river discharge is large, i.e. during low river discharge rates. Estuaries such as the Curimataú Estuary ($R \sim 2.5$ m and $h \sim 6$ m) with high ratio values R/h may have a greater diffusion contribution, the Caravelas ($h \sim 6.5$ m) and Perúípe ($h \sim 7.5$ m) estuaries with the maximum tidal range (R) of ~ 2.5 meters, and the Mersey estuary ($h \sim 16$ m) forced by a tidal range (R) of up to ~ 10.5 meters. Therefore, a larger diffusion contribution may result in a larger time of exposure (see Table 6.2), and thus a return coefficient close to unit.

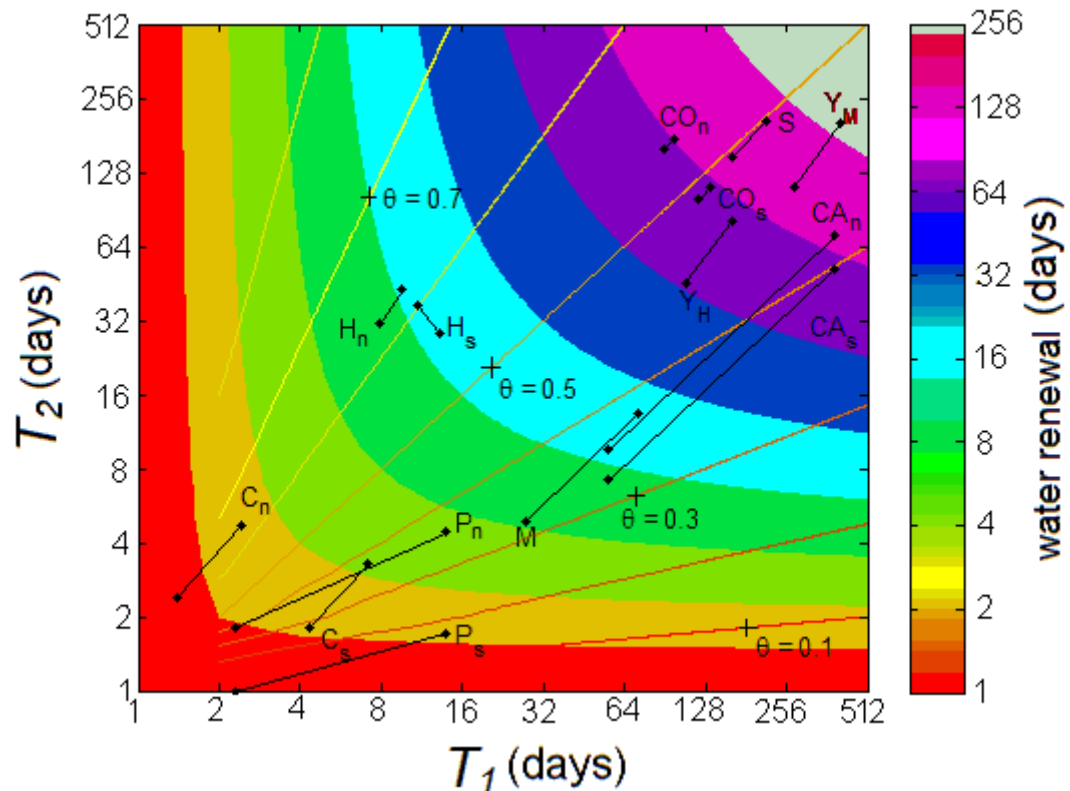


Figure 6.7 – The position of estuaries on the advection-diffusion diagram to indicate the relative contribution to the water renewal T_p by the advective (T_1) and dispersive (T_2) timescales using a logarithmic scale. Subscript (n) and (s) indicate neap and spring tide conditions. For the Curimataú Estuary (C), K was estimated from Hansen-Rattray's formula. Hudson, Caravelas, Peruípe, and Conwy estuaries are denoted (H), (CA), (P), and (C), respectively. For the Mersey (M), and Scheldt (S) estuaries, results are from an average range. For the York River Estuary the conditions are for high river flow (Y_H), and mean river flow (Y_M). The parameter θ , represented by straight lines, indicates the relative advective contribution to water renewal varying in the range $0 \leq \theta \leq 1$. The diagonal line $\theta = 0.5$, separates the areas where transport is dominated by dispersion (diagram lower zone, $\theta < 0.5$) and advection (diagram upper zone, $\theta > 0.5$).

6.8 Summary and Conclusions

A new method has been developed that quantifies the relative contribution of advection and diffusion to water renewal in estuaries using simple measurements of the river flow Q_r ($\text{m}^3 \text{s}^{-1}$), the estuary volume V (m^3) and length L (m), estimates of the mean salinity S_E , and the salinity at the inflow S' (at, $x = 0$) and outflow S_O (at, $x = L$) boundaries. Such data are usually available for most estuaries worldwide. From this method estuaries may be categorized using the Advection-Diffusion diagram, and estuaries can be divided into those which are dominated by diffusion (e.g. Mersey Estuary), those dominated by advection (e.g. Hudson Estuary), and those where diffusion and advection are of similar magnitude (e.g. Conwy Estuary). The model is applicable to estuaries of simple geometries and without significant baroclinic circulation.

The method can be used to study the impact on water renewal of spring-neap tidal fluctuations and seasonal variations of river flow and tides. For example, in the Curimataú, high river flows occur mostly in summer during the wet season, whereas low flows occur mainly in winter. For such systems, the river discharge may remain nearly constant for several weeks and the relative contribution of diffusion and advection on the estuarine residence time would change along the spring-neap tide cycle. In contrast, results of the Conwy estuary have shown a nearly equal contribution of the advection and diffusion terms at neap and spring tides. In the Hudson estuary the residence time was dominated by advection, while in the Caravelas, Peruípe, Mersey and Scheldt estuaries the diffusion term prevails over water renewal.

Results calculated using the LOICZ model were always smaller than the modified LOICZ model and also the results of hydrodynamic models. The reason is the method of calculation of the exchange flow used in the LOICZ method. The difference in the exchange flow between the LOICZ model and our proposed method depends upon the factor γ , which determines the diffusion contribution the water renewal time (see Eqts. 6.14 and 6.20). By using the equation of salt balance proposed by Fisher et al. (1979) we have proposed a new exchange flow that may be used in the LOICZ model, and which reduces the diffusion coefficient applied to the estuary.

Results from the CART's theory have shown that the exposure time was more comparable to the residence time estimated using numerical models, while the results of the mean residence time calculated using the CART's formula were usually reduced. For most cases the water renewal estimated using the newly proposed modified LOICZ model was more comparable to the mean maximum residence time from hydrodynamic models, with $r^2 = 0.70$. The return coefficient calculated from CART's theory has shown good correlation with the diffusion contribution, with $r^2 = 0.66$. Our study adds value to the LOICZ formulation in that we have made improvements to estimate the water renewal timescales.

Acknowledgements

This study was supported by the IPRS fellowship to FPA. The authors greatly acknowledge kind assistance of Dr. E. Wolanski, Dr. L. de Miranda, Dr. L. Lucas and Dr. D. Prandle. Eric Deleersnijder is an honorary research associate with the Belgian Fund for Scientific Research (FNRS) and his contribution to the present study was achieved in the framework of the Interuniversity Attraction Pole TIMOTHY, which was funded by BELSPO (www.belspo.be) under contract IAP6.13.

7 CONCLUSIONS

The finite element unstructured model SLIM was successfully applied to simulate the water circulation and to analyse some physical oceanographic features of the Great Barrier Reef. The model was well calibrated using current measurements from up to twenty mooring sites. Moreover, this is the first numerical model applied to the Great Barrier Reef that was previously calibrated to accurately model mixing processes. This calibration was achieved by comparing model results with measurements of salinity during the dry season (i.e. typically between August and November). The SLIM model adequately simulated the mean slope of the salinity rise, the magnitude of salinity achieved at steady-state, and the time scale for reaching steady state (Andutta et al., 2011). The model was successfully used to estimate a few different transport timescales for coastal areas and bays in the central GBR, and the model was used to analyse the influence from reef density on water renewal within many reef configurations and cluster of reefs. Also, a further variation of simple methods to estimate transport timescales was developed and applied to many estuaries worldwide. In summary, objectives previously mentioned were all satisfied.

For the SLIM model a high resolution mesh (i.e. ~150 to ~ 20000 meters) was applied efficiently over the reef matrix, around islands and near the coastline. This high mesh resolution allowed the model to account for a proper dispersion due to tidal currents and other effects from bathymetry, oceanic inflow in the GBR and wind conditions. This unstructured model was more efficient compared to previous structured models applied to the GBR (King and Wolanski, 1996, Brinkman et al., 2001, Luick, et al., 2007), and models that required the application of a reef parameterization to account for the through flow within the reef matrix (Luick, et al. 2007), while the applied model resolution in this thesis, allowed simulation of tidal jet streams even between small reef passages.

The specific conclusions for each chapter are summarized as follows:

The hypersaline waters in the GBR

The NCJ inflow from the Coral Sea combined with the wind conditions and tidal mixing control the dynamic of hypersaline water in the dry season in the GBR. From

the numerical results it was observed that the salinity gradient was more sensitive to changes in the NCJ inflow than for change in the diffusion coefficient K . Therefore, the adjustments for the right residual circulation are important for the model validation.

The dynamics of the hypersaline coastal boundary layer in the GBR differs from other hypersaline systems world-wide. In some hypersaline bays such as in Shark Bay and Hervey Bay, the bathymetry is relatively shallow (e.g. average depth < 10 meters), and vertical mixing thereupon inhibits the hypersaline waters from sinking and escaping along the bottom. In contrast to shallow systems, in the deeper Spencer Gulf, with average depth 40-50 m, during conditions of neap tides the vertical mixing reduces and allows for the vertical stratification of the salinity. This results in the hypersaline waters sinking along the seabed by the resultant baroclinic flow (Nunes Vaz et al., 1990). Nevertheless, during spring tides the vertical mixing increases and thus inhibits vertical stratification, and hypersaline waters are thus trapped for short periods.

In the GBR different dynamics prevail because the bays are much more open and as a result hypersaline water is exported sideways and transferred from bay to bay by the longshore currents as well as cross-shelf by tidal diffusion. The width of this hypersaline coastal boundary layer increases southwards and is mainly controlled by advection by the southward residual current due the Coral Sea inflow. This boundary layer demonstrates connectivity between bays.

The Flushing time and age of water in the GBR

The flushing time for the central GBR was estimated to be between 1.5 and 9 months. For the real wind conditions it was ~ 67 days. The maximum flushing time was 9 months, and was obtained for zero wind and zero Coral Sea inflow. The flushing time varied between the zones in the GBR, and thus shows a potential deficiency of 1D cross-shelf models (Hancock et al., 2006, Wang, et al., 2007). The flushing time for the bays varied in the range of 0.5 to 6 weeks, and the effect of the wind and the NCJ inflow was to reduce the flushing time.

The numerical results have shown that the main mechanism for the flushing of waters within the GBR is the NCJ intruding water in the GBR. This inflow generates a residual current that replaces the water in the lagoon, however, processes such as the tidal mixing and the wind driven currents are added to that. An important finding here was the effect of the unsteadiness of the wind. Fluctuating southeasterly wind results in

the wind-driven current opposing the mean current by the NCJ inflow, thereupon, this inflow is deflected seaward away from the inner shelf to make room for the opposite wind-driven current over the inner shelf. The NCJ inflow combined with the wind driven currents may increase the flushing times in inner shelf waters because of the reversing wind driven currents may transport some water back to source. The water may be transported back to source even after a few weeks, and this process is parameterized by the return coefficient, which may be as large as ~ 0.7 .

The Sticky water effect

The SLIM model used an improved resolution within the reef matrix, and this resolution has improved results of water circulation for the reef areas in the GBR and has shown that for a few locations over the reefs a high percentage of larvae may return to their natal reef (Jones et al., 1999; Almany et al., 2007). The hydrodynamic results showed that some structures of reefs leads to a time of retention of larvae that equates to the PLD of many larvae. Besides, in areas where sticky water effect prevails the fish larvae are not required to have strong swimming abilities to remain in natal reefs.

For the GBR it has been shown that the model needs to be capable of merging both large scales and small scales processes for the sticky water effect to be simulated. Furthermore, the model needs to account for the correct forcing by the NCJ inflow and a high resolution that does not erase small reefs. Results of the exposure time have shown that the distribution of the high self-seeding zones is patchy in a reef matrix, and thus the GBR comprises a number of hot spots of high self-seeding reefs imbedded within a network of reefs that are replenished mainly by long-distance connectivity.

Results of the exposure time include conditions where the wind affects the circulation. However, for coral reefs on the GBR, many organisms spawn in November and December when light winds prevail. These results were for two wind conditions, namely calm weather conditions and a southeasterly wind at 6.67 m s^{-1} (the mean value for those months in the GBR). In some years however strong winds may apply, and at such times the wind may modify our predictions due to the influence of wave breaking over shallow areas. This remains unknown and further research is needed.

This study of the sticky water effect has provided two formulae for predicting the exposure time of passively drifting particles near reefs. These formulae may help ecologists to make predictions on levels of connectivity among reefs and clusters of

reefs for which the detailed oceanography is unknown. This knowledge may be used for sampling designs for areas where predictions may be made on connectivity in ecological and evolutionary time (e.g. Taylor and Hellberg, 2003; Jones et al., 2005). These formulae may assist predictions on connectivity, and thus help the planning of site and placement of MPA for sources and sink reefs as well as areas where retention is likely to be high (Palumbi, 2004).

It is important to know that currents alone do not describe levels of connectivity as some larvae have excellent swimming ability and sensory systems that provide directionality, potentially allowing them to stay near or search for natal reefs (Kingsford et al., 2002). Despite this, even fishes have very limited mobility early in life. Many fishes only have strong swimming ability during the last 0.25 of their PLD (Fisher et al., 2000; Fisher, 2005); hence the levels of passive drift explained in this study are relevant.

Estuarine hydrology

It was shown that estuarine waters are commonly more biologically productive than the oceanic waters. Therefore it is extremely important to understand how such environment evolves in order to promote a sustainable development in areas around estuaries. Many definitions of estuaries were well explained in terms of the water circulation, geological aspects and so on, and the transport time scales namely flushing time, residence time and age, have been well described with the related implications on local ecology.

Transport time scales

The new LOICZ model resulted in the best fit compared to residence time from numerical models, with $r^2 \sim 0.70$. A graphic conceptual model, the advection/diffusion timescale diagram was also developed, which was used to visualize where different estuaries lie in the advective/diffusive timescale space diagram. Estuaries can now be divided into those which are dominated by diffusion, those which are dominated by advection and those where diffusion and advection are of similar magnitude.

Appendix 1

Features of the Curimataú Estuary, Brazil (Miranda et al., 2005; Miranda et al., 2006; Andutta et al., 2006).

Feature	Curumataú Estuary
mean estuary depth h (m)	6-7
mean estuary width l (m)	250-350
mean estuary cross-sectional area A (m ²)	1500-2450
longitudinal distance L (m)	10000
estuary volume V (m ³) x10 ⁶	15-24.5
river discharge Q (m ³ s ⁻¹)	120 (measured in neap tides) 40 (measured in spring tides)
gradient of salinity dS/L (psu m ⁻¹)	neap tides 3.0×10^{-3} spring tides 1.3×10^{-3}
estuarine salinity S_E	$S_{E(neap)}$ 15-18 $S_{E(spring)}$ 28-32
salinity at mouth S_O	$S_{O(neap)}$ 30 $S_{O(spring)}$ 36
salinity at 10 km away from the mouth; S'	$S'_{(neap)}$ 0 $S'_{(spring)}$ 23
diffusion K (m ² s ⁻¹) Hansen-Rattray's formula	$K_{(neap)}$ 250-800 $K_{(spring)}$ 435-1400
diffusion K (m ² s ⁻¹) Fisher's formula	$K_{(neap)}$ 490-960 $K_{(spring)}$ 703-1313

Estimative of horizontal diffusion K to the Curimataú Estuary using Hansen-Rattray formula and vertical steady state salinity profiles of Miranda et al., 2005				
Parameters	Neap tide		Spring tide	
residual velocity- u (m s ⁻¹)	0.057		0.016	
salinity at ($x = 10$ km) - S'	0		23	
salinity at mouth - S_O	30		36	
longitudinal distance - L (m)	10000		10000	
position of the vertical profile x (m)	5000		5000	
non-dimensional number (v)	0.65		1	
vertical viscosity - N_z (m ² s ⁻¹)	1×10^{-4}		5×10^{-4}	
vertical difusivity - K_z (m ² s ⁻¹)	1×10^{-3}		1×10^{-3}	
wind stress - (Nm ⁻²)	0		0	
average depth - h (m)	6	7	6	7
estuarine salinity - S_E	17.0-19	20.3-23.5	29.0-30.0	30.3-32.5
horizontal difusivity - K (m ² s ⁻¹)	250-330	500-800	435-550	800-1400

Appendix 2

Features of the Caravelas Estuary, Brazil (Andutta 2011, Andutta and Miranda, submitted).

Feature	Caravelas Estuary
mean estuary depth h (m)	6-7
mean estuary width l (m)	600-800
mean estuary cross-sectional area A (m ²)	3.6-5.6 x10 ³
longitudinal distance L (m)	~12000
estuary volume V (m ³) x10 ⁶	43.2-67.2
river discharge Q (m ³ s ⁻¹)	Q ~ 2-9
gradient of salinity dS/L (psu m ⁻¹)	neap tides 4.75x10 ⁻⁴
	spring tides 3.75 x10 ⁻⁴
estuarine salinity S_E	$S_{E (neap)}$ 32-34
	$S_{E (spring)}$ 33-34
salinity at mouth S_O	$S_{O (neap)}$ 35.9
	$S_{O (spring)}$ 36.0
salinity at 10 km away from the mouth; S'	$S'_{(neap)}$ 30.2
	$S'_{(spring)}$ 31.5

Appendix 3

Features of the Peruípe Estuary, Brazil (Andutta 2011, Andutta and Miranda, submitted).

Feature	Peruípe Estuary
mean estuary depth h (m)	7-8
mean estuary width l (m)	400-600
mean estuary cross-sectional area A (m ²)	2.8-4.8 $\times 10^3$
longitudinal distance L (m)	~5000
estuary volume V (m ³) $\times 10^6$	14-24
river discharge Q (m ³ s ⁻¹)	$Q \sim 20-70$
gradient of salinity dS/L (psu m ⁻¹)	neap tides 1.6×10^{-3}
	spring tides 3.6×10^{-4}
estuarine salinity S_E	$S_{E (neap)}$ 26-28
	$S_{E (spring)}$ 29-30
salinity at mouth S_O	$S_{O (neap)}$ 31.6
	$S_{O (spring)}$ 32.0
salinity at 10 km away from the mouth; S'	$S'_{(neap)}$ 23.4
	$S'_{(spring)}$ 28.5

Appendix 4

Features of the Hudson Estuary, USA (Warner et al., 2005).

Feature	Hudson Estuary
mean estuary depth h (m)	7.5-8.5
mean estuary width l (m) $\times 10^3$	1.55-1.65
mean estuary cross-sectional area A (m^2) $\times 10^3$	11.625-14.025
longitudinal distance L (m)	45000
estuary volume V (m^3) $\times 10^6$	523-631
river discharge Q ($\text{m}^3 \text{s}^{-1}$)	770 (measured in neap tides) 550 (measured in spring tides)
gradient of salinity dS/L (psu m^{-1})	neap tides 4.7×10^{-4} spring tides 4.9×10^{-4}
estuarine salinity S_E	$S_{E(\text{neap})}$ 7.5-8.5 $S_{E(\text{spring})}$ 13-14
salinity at mouth S_O	$S_{O(\text{neap})}$ 34 $S_{O(\text{spring})}$ 36
salinity at 45 km away from the mouth; S'	$S'_{(\text{neap})}$ 0 $S'_{(\text{spring})}$ 0

Appendix 5

Features of the Conwy Estuary, UK (Turrell et al., 1996).

Geometry features by segments						
segment	distance from Deganwy Narrows (km)	length L (km)	width l (m)	depth h (m)	area $\times 10^3 A$ (m ²)	volume $\times 10^6 V$ (m ³)
a)	2.44-3.93	1.5	530	5.0-5.5	2.7-2.9	$V_a = 4.0-4.3$
b)	3.93-7.86	3.9	430	4.5-5.0	1.9-2.2	$V_b = 7.6-8.4$
c)	7.86-9.51	1.7	225	4.0-4.5	900-1013	$V_c = 1.5-1.7$
d)	9.51-11.14	1.6	120	3.5-4.0	420-480	$V_d = 0.7-0.8$
e)	11.14-14.32	3.2	90	3.0-3.5	270-315	$V_e = 0.9-1.0$
total	2.44-14.32	11.9	246-274	5.0	1228-1368	$V_{total} = 14.6-16.2$
Features of salinity by segments						
segment	Volume normalized	ΔS (neap)	S_o (neap)	ΔS (spring)	S_o (spring)	
a)	$V_e/V_{total} \sim 0.27$	26.5-28.0	$S_a \sim 27.3$	30.0-32.0	$S_a \sim 31.0$	
b)	$V_b/V_{total} \sim 0.52$	15.0-26.5	$S_b \sim 20.8$	24.2-30.0	$S_b \sim 27.1$	
c)	$V_c/V_{total} \sim 0.10$	10.5-15.0	$S_c \sim 12.8$	20.5-24.2	$S_c \sim 22.4$	
d)	$V_d/V_{total} \sim 0.05$	5.0-10.5	$S_d \sim 7.8$	19.0-20.5	$S_d \sim 19.8$	
e)	$V_e/V_{total} \sim 0.06$	0.0-5.0	$S_e \sim 2.5$	13.9-19.0	$S_e \sim 16.5$	
total	$V_{total}/V_{total} = 1$	0.0-28.0	$S_{total} \sim 20.0$	13.9-32.0	$S_{total} \sim 26.7$	
<p>Notes: To estimate each segment mean width it was used the ruler tool from Google Earth. The mean salinity of the entire system was calculated from the volume normalizer expression:</p> $S_{total} = S_a \cdot \frac{V_a}{V_{total}} + S_b \cdot \frac{V_b}{V_{total}} + \dots + S_f \cdot \frac{V_f}{V_{total}}.$						

Feature	Conwy Estuary
mean estuary depth h (m)	5.0
mean estuary width l (m)	246-274
mean estuary cross-sectional area A (m ²) $\times 10^3$	1.23-1.34
longitudinal distance L (m)	11880
estuary volume V (m ³) $\times 10^6$	14.6-16.2
river discharge Q (m ³ s ⁻¹)	1.9 (measured in neap tides) 1.4 (measured in spring tides)
gradient of salinity dS/L (psu m ⁻¹)	neap tides 2.4×10^{-3} spring tides 1.5×10^{-3}
estuarine salinity S_E	$S_{(neap)}$ 19.19 $S_{(spring)}$ 26.46
salinity at mouth S_O	$S_{O(neap)}$ 34 $S_{O(spring)}$ 36
salinity at 11.88 km away from the mouth; S'	$S'_{(neap)}$ 0 $S'_{(spring)}$ 14

Appendix 6

Features of the Mersey Estuary, UK (Bowden and Gilligan, 1971; Wu et al., 2005; Yuan et al., 2007).

Geometry features by segments						
Segment	Distance from Mersey entrance (km)	Length L (km)	Width l (m)	Depth h (m)	Area $\times 10^3 A$ (m ²)	Volume $V \times 10^6$ (m ³)
a)	0-4.4	4.4	1200	15-17	18.7-21.2	V_a 233-264
b)	4.41-7.86	3.7	1200	15-17	17.9-20.3	V_b 214-243
c)	7.86-12.83	5	2400	15-17	35.7-40.5	V_c 850-963
d)	12.83-20	7.2	3500	15-17	52.5-59.5	V_d 184-208
total	0-20	20	1400	15-17	15.7-17.7	V_{total} 313-355
Features of salinity by segments						
Segment	Volume normalized		ΔS		S_o	
a)	$V_a/V_{total} \sim 0.07$		29.4-30.1		$S_a \sim 29.75$	
b)	$V_b/V_{total} \sim 0.07$		28.7-29.4		$S_b \sim 29.05$	
c)	$V_c/V_{total} \sim 0.27$		27.8-28.7		$S_c \sim 28.25$	
d)	$V_d/V_{total} \sim 0.59$		24.9-27.8		$S_d \sim 26.35$	
total	$V_{total}/V_{total} = 1$		24.9-30.1		$S_{total} \sim 27.29$	
<p>Notes: To estimate each segment mean width it was used the ruler tool from Google Earth. The mean salinity of the entire system was calculated from the volume normalizer expression:</p> $S_{total} = S_a \cdot \frac{V_a}{V_{total}} + S_b \cdot \frac{V_b}{V_{total}} + \dots + S_f \cdot \frac{V_f}{V_{total}}.$						

Feature	Mersey Estuary
mean estuary depth h (m)	15-17
mean estuary width l (m)	1445
mean estuary cross-sectional area A (m ²) $\times 10^3$	15.7-17.8
longitudinal distance L (m)	20000
estuary volume V (m ³) $\times 10^6$	313-355
river discharge Q (m ³ s ⁻¹)	50-150 (range)
gradient of salinity dS/dx (psu m ⁻¹)	2.6×10^{-4}
estuarine salinity S_E	27-28
salinity at mouth S_O	30
salinity at 20 km upstream from the mouth; S'	25

Appendix 7

Features of the Scheldt Estuary, (de Brauwere et al., 2011; de Brye et al., 2012).

Geometry features by segments					
Segment	Length L (km)	Width l (m)	Depth h (m)	Cross-sectional Area $A \cdot 10^3$ (m ²)	Volume $V \cdot 10^3$ (m ³)
1	7950	372.5	9.0	3.35	$V_1 = 26649$
2	8300	370.2	10.4	3.85	$V_2 = 31957$
3	9600	666.0	9.3	6.19	$V_3 = 59460$
4	5100	559.3	10.1	5.65	$V_4 = 28807$
5	9700	779.9	9.0	7.02	$V_5 = 69830$
6	5950	2754.8	8.0	22.04	$V_6 = 131128$
7	5700	2533.2	6.0	15.20	$V_7 = 86636$
8	5300	2702.9	7.4	20.00	$V_8 = 106008$
9	5900	2257.2	11.9	26.86	$V_9 = 158476$
10	6900	5033.6	9.0	45.30	$V_{10} = 312588$
11	6200	4889.5	9.9	48.41	$V_{11} = 300120$
12	12100	4088.7	12.0	49.06	$V_{12} = 593684$
13	13300	4791.6	13.7	65.65	$V_{13} = 873080$
Total	102000	2808.2	9.7	27.24	2778423

Feature	Scheldt Estuary
mean estuary depth h (m)	9.7
mean estuary width l (m)	2808.2
mean estuary cross-sectional area A (m ²) $\times 10^3$	27.24
longitudinal distance L (m)	102000
estuary volume V (m ³) $\times 10^6$	2778
river discharge Q (m ³ s ⁻¹)	150-200 (average range)
gradient of salinity dS/L (psu m ⁻¹)	1.0×10^{-4}
estuarine salinity S_E	30-32
salinity at mouth S_O	34
salinity at 102 km away from the mouth; S'	5

Appendix 8

Features of the York River Estuary, (Sandifer, 1973; Haas, 1977; Shen and Haas, 2004).

Feature	York River Estuary
mean estuary depth h (m)	8-10
mean estuary width l (m)	2700-3200
mean estuary cross-sectional area A (m ²) x10 ³	21.6-32.0
longitudinal distance L (m)	47000
estuary volume V (m ³) x10 ⁶	1015-1504
river discharge (Mattaponi and Pamunkey rivers) Q (m ³ s ⁻¹)	43.1 (average)
river discharge (Mattaponi and Pamunkey rivers) Q (m ³ s ⁻¹)	107.5 (high)
estuarine salinity S_E	16-17
salinity at mouth S_O	20
salinity at 47 km away from the mouth; S'	12-13

References

- Almany, G.R., Berumen, M.L., Thorrold, S.R., Planes, S., Jones, G.P., 2007. Local replenishment of coral reef fish populations in a marine reserve. *Science* 316, 742–744.
- Andrews, J.C., 1983. Water masses, nutrient levels and seasonal drift on the outer central Queensland shelf (Great Barrier Reef). *Australian Journal of Marine and Freshwater Research* 33, 717–722.
- Andrews, J.C., Furnas, M.J., 1986. Subsurface intrusions of Coral Sea Water into the central Great Barrier Reef—I. Structures and shelf-scale dynamics. *Continental Shelf Research* 6, 491–514.
- Andrews, J. C., Bode, L., 1988. The tides of the Central Great Barrier Reef. *Continental Shelf Research* 8, 1057–1085.
- Andrews, J. C., Clegg, S., 1989. Coral Sea circulation and transport from modal information models. *Deep-Sea Research* 36, 957–974.
- Andutta, F., Miranda, L. (submitted). Transport time scales in a well and partially mixed tropical estuary.
- Andutta, F., Kingsford, M., Wolanski, E., 2012. ‘Sticky water’ enables the retention of larvae in a reef mosaic. *Estuarine Coastal and Shelf Science* 101, 54–63.
- Andutta, F.P., Ridd, P.V., Wolanski E., 2011. Dynamics of hypersaline coastal waters in the Great Barrier Reef. *Estuarine, Coastal and Shelf Science* 94, 299–305.
- Andutta, Fernando P., 2011. The estuarine system of the Caravelas and Peruípe rivers (Bahia): Observations, simulations, residence time, and advective and diffusive processes, PhD Thesis. IO-USP, Oceanography Institute of the University of São Paulo, 121p.
- Andutta, F.P, Miranda, L.B., Castro, B.M., Fontes, R.F.C., 2006. Numerical Simulation of the Hydrodynamic in the Curimataú Estuary, RN Brazil. *Oceanography and Global Changes, SP-Brazil*, 545–558.
- Arega, F., Armstrong, S., Badr, A.W., 2008. Modeling of residence time in the East Scott Creek Estuary, South Carolina, USA, *Journal of Hydro-environment Research* 2, 99–108.
- Ayre, D.J., Hughes, T.P., 2000. Genotypic diversity and gene flow in brooding and spawning corals along the Great Barrier Reef, Australia. *Evolution* 54, 1590–1605.

- Babcock, R.C., Bull, G.D., Harrison, P.L., Heyward, A.J., Oliver, J.L., Wallace, C.C., Willis, B.L., 1986. Synchronous spawning of 105 scleractinian coral species on the Great Barrier Reef. *Mar. Biol.* 90, 379–394.
- Black, K.P., Gay, S.L., 1987. Eddy formation in unsteady flows, *Journal of Geophysical Research* 92(C9), 9514–9522.
- Black, K.P., Gay, S.L., Andrews, J.C., 1990. Residence times of neutrally-buoyant matter such as larvae, sewage or nutrients on coral reefs. *Coral Reefs* 9, 105–114.
- Black, K.P., 1993. The relative importance of local retention and inter-reef dispersal of neutrally buoyant material on coral reefs. *Coral Reefs* 12, 43–53.
- Bode, M., Bode, L., Armsworth, P., 2006. Larval dispersal reveals regional sources and sinks in the Great Barrier Reef. *Marine Ecology Progress Series* 308, 17–25.
- Bolin, B., H. Rodhe, 1973. A note on the concepts of age distribution and transit time in natural reservoirs, *Tellus* 25, 58–62.
- Bowden, K.F. and Gilligan, R.M., 1971. Characteristic features of estuarine circulation as represented in the Mersey Estuary. *Limnology and Oceanography* 16(3), 490–502.
- Brandon, D. E., 1973. Waters of the Great Barrier Reef province. In: O. A. Jones and R. Endean (Eds.), *Biology and Geology of Coral Reefs* vol. 1, Geology 1, 187–232, Academic Press, New York.
- Bray, N. A., Rubles, J. M., 1991. Physical oceanography of the Gulf of California. In: J. P. Dauphin and B. R. T. Simoneit (Eds.), *The Gulf and Peninsular Province of the Californias*. AAPG Mem. 47, 511–533.
- Breitburg, D.L., L.A. Davias, K.E. Limburg, and D. P. Swaney., 2009. Linking Nutrients, Hypoxia, Fisheries, and Fishes: Interim Report from a Workshop supported by LOICZ. LOICZ Inprint 2009/2, 13–14.
- Brinkman, R., Wolanski, E., Deleersnijder, E., McAllister, F., Skirving, W., 2001. Oceanic inflow from the Coral Sea into the Great Barrier Reef. *Estuarine, Coastal and Shelf Science* 54, 655–668.
- Burgess, S.C., Kingsford, M.J., Black, K.P. 2007. Influence of tidal eddies and wind on the distribution of presettlement fishes around One Tree Island, Great Barrier Reef. *Marine Ecology Progress Series* 341, 233–242.

- Burrage, D., Steinberg, C., Bode, L., Black, K., 1997. Long-term current observations in the Great Barrier Reef. In State of the GBR World Heritage Area Workshop, Proceedings of a Technical Workshop, Townsville, Australia, D. Wachenfeld et al. (Eds.), pp. 21–45 (Great Barrier Reef Marine Park Authority), 561 pp.
- Burrage, D.M., Church, J.A., Steinberg, C.R., 1991. Linear systems analysis of momentum on the continental shelf slope of the Central Great Barrier Reef. *Journal of Geophysical Research* 96, 22169–22190.
- Carleton, J.H., Brinkman, R., Doherty, P.J., 2001. The effect of water flow around coral reefs on the distribution of pre-settlement fish (Great Barrier Reef, Australia).pp. 209–230 in Wolanski E (Editor), *Oceanographic Processes of Coral Reefs. Physical and Biological Links in the Great Barrier Reef*. CRC Press, Boca Raton, Florida.
- Carr, M.H., Reed, D.C., 1993. Conceptual issues to marine harvest refuges: examples from temperate reef fishes. *Canadian Journal of Fisheries and Aquatic Science* 50, 2019–2028.
- Chadwick, D. B., Largier, J.L., 1999. Tidal exchange at the bay-ocean boundary. *Journal of Geophysical Research* 104 (C12), 29901–29924.
- Choukroun, S., Ridd, P.V., Brinkman, R., McKinna, L.I.W., 2010. On the surface circulation in the western Coral Sea and residence times in the Great Barrier Reef. *Journal of Geophysical Research* 115, C06013, 13 pp.
- Christie, M.R., Johnson, D.W., Stallings, C.D., Hixon, M.A., 2010. Self-recruitment and sweepstakes reproduction amid extensive gene flow in a coral-reef fish. *Molecular Ecology* 19, 1042–1057.
- Christie, M.R., Tissot, B.N., Albins, M.A., Beets, J.P., Jia, Y., Ortiz, D.M., Thompson, S.E., Hixon, M.A., 2010. Larval connectivity in an effective network of Marine Protected Areas. *Plos One* 5, e15715.
- Church, J. A., Andrews, J. C., Boland, F. M., 1985. Tidal currents in the central Great Barrier Reef. *Continental Shelf Research* 4, 515–531.
- Church, J.A., 1987. East Australian Current adjacent to the Great Barrier Reef. *Australian Journal of Marine and Freshwater Research* 38, 671–683.
- Connolly, S.R., Baird, A., 2010. Estimating dispersal potential for marine larvae: dynamic models applied to scleractinian corals. *Ecology* 91, 3572–3583.

- Cowen, R.K., Paris, C.B., Srinivasan, A., 2006. Scaling of connectivity in marine populations. *Science* 311, 522–527.
- Crawford, W.R., Tyler, A.V., Thomson, R.E., 1990. A possible eddy retention mechanism for ichthyoplankton in Hecate Strait. *Canadian Journal of Fisheries and Aquatic Sciences* 47, 1356–1363.
- Crossland, C.J., Kremer, H.H., Lindeboom, H.J., Marshall Crossland, J.I., Le Tissier, M.D.A., 2005. *Coastal Fluxes in the Anthropocene*. Springer-Verlag, Berlin, 231 pp.
- Das, P., Marchesiello, P., Middleton, J.H., 2000. Numerical modelling of tide-induced residual circulation in Sydney Harbour. *Marine and Freshwater Research* 51, 97–112.
- Deleersnijder E., Norro, A., Wolanski, E., 1992. A three-dimensional model of the water circulation around an island in shallow water, *Continental Shelf Research* 12, 891–906.
- Deleersnijder, E., Campin, J.M., Delhez, E.J.M., 2001. The concept of age in marine modeling. I. Theory and preliminary model results. *Journal of Marine Systems* 28, 229–267.
- Deleersnijder, R., Beckers, J. M., Delhez, E. J. M., 2006. On the behavior of the residence time at the bottom of the mixed layer. *Environmental Fluid Mechanics* 6, 541–547.
- Delhez, E.J.M., Heemink, A.W., Deleersnijder, E., 2004. Residence time in a semi-enclosed domain from the solution of an adjoint problem, *Estuarine, Coastal and Shelf Science* 61, 691–702.
- Delhez, E. J. M., 2006. Transient residence and exposure times. *Ocean Science* 2, 1–9.
- Delhez, E.J.M. and Deleersnijder, E., 2006. The boundary layer of the residence time field, *Ocean Dynamics* 56, 139–150.
- Delhez, E.J.M., Deleersnijder, E., 2010. Residence time and exposure time of sinking phytoplankton in the euphotic layer, *Journal of Theoretical Biology* 262, 505–516.
- de Brauwere, A., de Brye, B., Blaise, S., Deleersniider, E., 2011. Residence time, exposure time and connectivity in the Scheldt Estuary. *Journal of Marine Systems* 84, 85–95.

- de Brye, B., de Brauwere, A., Gourgue, O., Delhez, E.J.M., Deleersnijder, E., 2012. Water renewal timescales in the Scheldt Estuary. *Journal of Marine Systems* 94, 74–86.
- Dight, I.J., James, M.K., Bode, L. 1990. Modelling the larval dispersal of *Acanthaster planci*. II. Patterns of reef connectivity. *Coral Reefs* 9, 125–134.
- Diop, E. S., Soumare, A., Diallo, N., Guisse, A., 1997. Recent change of mangroves of the Saloum River Estuary, Senegal. *Mangroves and Salt Marshes* 1, 163–172.
- Dyer, K.R., 1973. *Estuaries: A physical Introduction*. 2nd Edition. John Wiley, 195 pp.
- Fischer, H.B., List, J.E., Koh, C.R., Imberger J., Brooks, N.H., 1979. *Mixing in inland and coastal waters*. Elsevier, Amsterdam, 302 pp.
- Fisher, R., Bellwood, D.R., Job, S.D., 2000. Development of swimming abilities in reef fish larvae. *Marine Ecology Progress Series* 202, 163–173.
- Fisher, R., 2005. Swimming speeds of larval coral reef fishes: impacts on self-recruitment and dispersal. *Marine Ecology Progress Series* 285, 223–232.
- Furnas, M., 2003. *Catchments and Corals: Terrestrial runoff to the Great Barrier Reef*. Australian Institute of Marine Science, Townsville, Australia.
- Furukawa, K., Wolanski, E., 1997. Shallow water frictional effects in island wakes, *Estuarine, Coastal and Shelf Science* 46: 599–608.
- Ganachaud, A., Gourdeau, L., 2008. Bifurcation of the subtropical south equatorial current against New Caledonia in December 2004 from a hydrographic inverse box model. *Journal of Physical Oceanography* 38, 2072–2084.
- Ganachaud, A., Kessler, W., Wijffels, S., Ridgway, K, Cai, W., Holbrook, N., Bowen, M., Sutton, P., Qiu, B., Timmermann, A., Roemmich, D., Sprintall, J., Cravatte, S., Gourdeau, L., Aung, T., 2007. Southwest Pacific Ocean Circulation and Climate Experiment. Part I. Scientific Background. NOAA OAR Special Report / International CLIVAR Project Office. C. P. S. N. 111.
- Gerlach, G., Atema, J., Kingsford, M.J., Black, K.P., Miller-Sims, V., 2007. Smelling home can prevent dispersal of reef fish larvae. *PNAS* 104, 858–863.
- Gladstone, W., Westoby, M., 1988. Growth and reproduction in *Canthigaster valentini* (Pisces, Tetradontidae): a comparison of a toxic reef fish with other reef fishes. *Environ. Biol. Fishes.* 21, 207–221.
- Gordon, D. C., Jr., P. R. Boudreau, K. H. Mann, J.E. Ong, W. L. Silvert, S. V. Smith, G. Wattayakorn, F. Wulff, and T. Yanagi., 1996. LOICZ Biogeochemical

- Modelling Guidelines. Land-Ocean Interactions in the Coastal Zone, LOICZ Reports & Studies 5. Texel, The Netherlands.
- Graber, H.C., Limouzy-Paris, C.B., 1997. Transport patterns of tropical reef fish larvae by spin-off eddies in the straits of Florida. *Oceanography* 10, 68–71.
- Gutierrez de Velasco, G., Winant, C. D., 2004. Wind- and density-driven circulation in a well mixed inverse estuary. *Journal of Physical Oceanography* 34, 1103–1116.
- Haas, L.W., 1977. The effect of the spring-neap tidal cycle on the vertical salinity structure of the James, York and Rappahannock Rivers, Virginia, U.S.A. *Estuarine and Coastal Marine Science* 5, 485–496.
- Haley Jr., P.J., Lermusiaux, P.F.J., 2010. Multiscale two-way embedding schemes for free-surface primitive equations in the “Multidisciplinary simulation, estimation and assimilation system”. *Ocean Dynamics* 60, 1497–1537.
- Haley Jr., P.J., Lermusiaux, P.F.J., Robinson, A.R., Leslie, W.G., Logoutov, O., Cossarini, G. Liang, X.S., Moreno, P., Ramp, S.R., Doyle, J.D., Bellingham, J., Chavez, F., Johnston, S., 2009. Forecasting and reanalysis in the Monterey Bay/California Current region for the Autonomous Ocean Sampling Network-II experiment. *Deep-Sea Research II* 56, 127–148.
- Hamann, M., Grech, A., Wolanski, E., Lambrechts, J., 2011. Modeling the fate of marine turtle hatchlings. *Ecological modeling* 222, 1515–1521.
- Hancock, G.J, Webster, I.T., Stieglitz, T.C., 2006. Horizontal mixing of Great Barrier Reef waters: Offshore diffusivity determined from radium isotope distribution. *Journal of Geophysical Research* 111(C12019), 14pp.
- Hansen, D.V. and Rattray, Jr.M., 1965. Gravitational circulation in straits and estuaries. *Journal of Marine Research* 23(1), 102–122.
- Haynes, D., Ralph, P., Prange, J., Dennison, W., 2000a. The impact of the herbicide diuron on photosynthesis in three species of tropical seagrass. *Marine Pollution Bulletin* 41, 288–293.
- Haynes, D., Müller, J., Carter, S., 2000b. Pesticide and herbicide residues in sediments and seagrass from the Great Barrier Reef World Heritage Area and Queensland coast. *Marine Pollution Bulletin* 41, 279–287.
- Hunter, C.L., Evans, C.W., 1995. Coral reefs in Kaneohe Bay, Hawaii: two centuries of western influence and two decades of data. *Bulletin of Marine Science* 57, 501–515.

- Hutchings, P., Kingsford, M., Hoegh-Guldberg, O., 2008. The Great Barrier Reef. CSIRO Publishing and Springer, Collingwood and Dordrecht, 392 pp.
- Jones, G.P., Milicich, M.J., Emslie, M.J., Lunow, C., 1999. Self-recruitment in a coral reef fish population. *Nature* 402,802–804.
- Jones, G.P., Planes, S., Thorrold, S.R., 2005. Coral reef fish larvae settle close to home. *Current Biology* 15, 1314–1318.
- Jones, G.P., Almany, G.R., Russ, G.R., Sale, P.F., Steneck, R.S., van Oppen, M.J.H., Willis, B.L., 2009. Larval retention and connectivity among populations of corals and reef fishes: history, advances and challenges. *Coral Reefs* 28, 307–325.
- Ketchum, B.H., 1950. Hydrographic factors involved in the dispersion of pollutants introduced into tidal waters. *Journal of the Boston Society of Civil Engineers* 37, 296–314.
- Ketchum, B.H., 1951. The exchanges of fresh and salt water in tidal estuaries. *Journal of Marine Research* 10, 18–38.
- King, B.A., Wolanski, E., 1996. Tidal current variability in the Central Great Barrier Reef. *Journal of Marine Systems* 9, 187–202.
- Kingsford, M.J., Leis, J., Shanks, A., Lindeman, K., Morgan, S., Pineda, J., 2002. Sensory environments, larval abilities and local self-recruitment. *Bull Mar Sci. Suppl.* 70, 309–340.
- Kremling, K., Wilhelm, G., 1997. Recent increase of the calcium concentrations in Baltic Sea waters. *Marine Pollution Bulletin* 34(10), 763–767.
- Lacombe, H., Richez, C., 1982. The regime of the Strait of Gibraltar. Elsevier Oceanography Series 34, 13–73.
- Lambrechts, J., Harnet, E., Deleersnijder, E., Bernard, P. E., Legat, V., Remacle, J. F., Wolanki, E., 2008. A multi-scale model of the hydrodynamics of the whole Great Barrier Reef. *Estuarine, Coastal and Shelf Science* 79, 143–151.
- Largier, J. L., Hollibaugh, J. T., Smith, S. V., 1997. Seasonally hypersaline estuaries in Mediterranean-climate regions. *Estuarine, Coastal and Shelf Science* 45, 789–797.
- Lavin, M. F., Godinez, V. M., Alvarez, L. G., 1998. Inverse-estuarine features of the Upper Gulf of California. *Estuarine, Coastal and Shelf Science* 47, 769–795.

- Lee, T.N., Rooth, C., Williams, E., McGowan, M., Smant, A.F., Clarke, M.E. 2002. Influence of the Florida Current, gyres and wind-driven circulation on transport of larvae and recruitment in the Florida Keys coral reefs. *Continental Shelf Research* 12, 971–1002.
- Legrand, S., Deleersnijder, E., Hanert, E., Legat, V., Wolanski, E., 2006. High-resolution unstructured meshes for hydrodynamics models of the Great Barrier Reef, Australia. *Estuarine, Coastal and Shelf Science* 68, 36–46.
- Lennon, G. W., Bowers, D., Nunes, R. A., Scott, B. D., Ali, M., Boyle, J., Wenju C., Herzfeld, M., Johansson, G., Nield, S., Petrusevics, P., Stephenson, P., Suskin, A. A., Wuffels, S. E. A., 1987. Gravity currents and the release of salt from an inverse estuary. *Nature* 327, 695–697.
- Lermusiaux, P.F.J., 2001. Evolving the subspace of the three-dimensional multiscale ocean variability: Massachusetts Bay. *Journal of Marine Systems* 29, 385–422.
- Lewis, S.E., Brodie, J.E., Bainbridge, Z.T., Rohde, K.W., Davis, A.M., Masters, B.L., Maugham, M. Devlin, M.J., Mueller, J.F., and Schaffelke, B., 2009. Herbicides: A new threat to the Great Barrier Reef. *Environmental Pollution* 157, 2470–2484.
- Lobel, P.S., Robinson, A.R., 1986. Transport and entrapment of fish larvae by mesoscale eddies and currents in Hawaiian waters. *Deep Sea Research* 33, 483–500.
- Lowe, R. J., Falter, J. L., Monismith, S. G., Atkinson, M. J., 2009. A numerical study of circulation in a coastal reef lagoon system, *Journal of Geophysical Research* 114(C06022), 1–18.
- Lucas, L.V., Thompson, J.K., Brown, L.R., 2009. Why are diverse relationships observed between phytoplankton biomass and transport time? *Limnology and Oceanography* 54, 381–390.
- Luick, J.L., Mason, L., Hardy, T., Furnas, M.J., 2007. Circulation in the Great Reef Barrier Lagoon using numerical tracers and in situ data. *Continental Shelf Research* 27, 757–778.
- McLusky, D.S., Elliott, M., 2004. *The Estuarine Ecosystem: Ecology, Threats and Management*. OUP, Oxford, 214 pp.
- Middleton, J.H., Cunningham, A., 1984. Wind-forced continental shelf waves from a geographical origin. *Continental Shelf Research* 3, 215–232.

- Miranda, L.B., Bérigamo, A.L., Castro, B.M., 2005. Interactions of river discharge and tidal modulation in a tropical estuary, NE, Brazil. *Ocean Dynamics* 55, 430–440.
- Miranda, L.B., Bérigamo, A.L., Silva, C.A.R., 2006. Dynamics of a Tropical Estuary: Curimataú River, NE Brazil. *Journal of Coastal Research* SI 39, 697–701.
- Monsen, N.E., Cloern, J.E., Lucas, L.V., Monismith, S.G., 2002. A Comment on the Use of Flushing Time, Residence Time, and Age as Transport Time Scales. *Limnology and Oceanography* 47, 1545–1553.
- Munday, P.L., Leis, J.M., Lough, J.M., Paris, C.B., Kingsford, M.J., Berumen, M.L., Lambrechts, J., 2009. Climate change and coral reef connectivity. *Coral Reefs* 28, 379–395.
- Nahas, E. L., Pattiaratchi, C. B., Ivey, G. N., 2005. Dynamics of frontal systems in Shark Bay, Western Australia. *Estuarine and Coastal Shelf Science* 65, 463–474.
- Nunes Vaz, R. A., Lennon, G. W., Bowers, D. G., 1990. Physical behaviour of a large, negative or inverse estuary. *Continental Shelf Research* 10, 277–304.
- Officer, C. B., 1980. Box models revisited, p. 65–114. In P. Hamilton and K. B. Macdonald (eds.), *Estuarine and Wetland Processes with Emphasis on Modeling*. Plenum Press, New York.
- Oliver, J., King, B., Willis, B., Babcock, R., Wolanski, E., 1992. Dispersal of coral larvae from a coral reef. Comparison between model predictions and observed concentrations. *Continental Shelf Research* 12, 873–891.
- Okubo, A., 1971. Diffusion diagrams. *Deep-Sea Research* 18, 789–802.
- Orr, A. P., 1933. Physical and chemical conditions in the sea in the neighbourhood of the Great Barrier Reef. In: *Scientific Report, Great Barrier Reef Expedition 1928-29 vol. II(3)*, 37–86, British Museum (Natural History), London.
- Palumbi, S.R., 2004. Marine reserves and ocean neighborhoods: The spatial scale of marine populations and their management. *Annual Review of Environment and Resources* 29, 31–68.
- Paris, C.B., Chérubin, L.M., Cowen, R.K., 2007. Surfing, spinning or diving from reef to reef: effects of population connectivity. *Marine Ecology Progress Series* 347, 285–300.
- Phillips, O. M., 1966. On the turbulent convection currents and the circulation in the Red Sea. *Deep-Sea Research* 13, 1149–1160.

- Pickard, G. L., 1977. A Review of the Physical Oceanography of the Great Barrier Reef and Western Coral Sea. AIMS Monography Series vol. 2, Australian Government Printer, Canberra.
- Prandle, D., 2009. Estuaries: Dynamics, Mixing, Sedimentation and Morphology. Cambridge University Press, Cambridge, 236 pp.
- Ramp, S.R., Lermusiaux, P.F.J., Shulman I., Chao, Y., Wolf, R.E., Bahr, F.L., 2011. Oceanographic and atmospheric conditions on the continental shelf north of the Monterey Bay during August 2006. *Dynamics of Atmospheres and Oceans* 52, 192–223.
- Reyns, N., Sponaugle, S., 1999. Patterns and processes of brachyuran crab settlement to Caribbean coral reefs. *Marine Ecology Progress Series* 185, 155–170.
- Ribbe, J., 2006. A study into the export of saline water from Hervey Bay, Australia. *Estuarine, Coastal and Shelf Science* 66, 550–558.
- Robertson, D.R., Petersen, C.W., Brawn, J.D., 1990. Lunar reproductive cycles of benthic brooding reef fishes: reflections of larval biology or adult biology? *Ecological Monographs* 60, 311–329.
- Sandifer, P.A., 1973. Distribution and abundance of Decapod Crustacean larvae in the York. *Chesapeake Science* 14(4), 235–257.
- Sheaves, M., 2006. Scale-dependent variation in composition of fish fauna among sandy tropical estuarine embayments. *Marine Ecology Progress Series* 310, 173–184.
- Shen, J., Haas, L., 2004. Calculating age and residence time in the tidal York River using three-dimensional model experiments. *Estuarine, Coastal and Shelf Science* 61, 449–461.
- Smagorinsky, I., 1963. General Circulation Experiment with Primitive Equations. *Monthly Weather Review* 91, 91–164.
- Smith, S.V., Buddemeier, R.W., Wulff, F., Swaney, D.P., 2005. C, N, P Fluxes in the Coastal Zone. Chapter 3 in: Crossland, C.J.; Kremer, H.H.; Lindeboom, H.J.; Marshall Crossland, J.I.; Le Tissier, M.D.A. (eds). *Coastal Fluxes in the Anthropocene. The Land-Ocean Interactions in the Coastal Zone Project of the International Geosphere-Biosphere Programme*. Springer-Verlag, Berlin Heidelberg.
- Spagnol, S., Wolanski, E., Deleersnijder, E., 2001. Steering by coral reef assemblages. pp. 145-160 in Wolanski E (Editor), *Oceanographic Processes of Coral Reefs*:

- Physical and Biological Links in the Great Barrier Reef. CRC Press, Boca Raton, Florida.
- Spagnol, S., Wolanski, E., Deleersnijder, E., Brinkman, R., McAllister, F., Cushman-Roisin, B., Hanert, E., 2002. An error frequently made in the evaluation of advective transport in two-dimensional Lagrangian models of advection-diffusion in coral reef waters. *Marine Ecology Progress Series* 235, 299–302.
- Spivakovskaya, D., Heemink, A.W., Deleersnijder, E., 2007. The backward Ito method for the Lagrangian simulation of transport processes with large space variations of the diffusivity, *Ocean Science* 3, 525–535.
- Sponaugle, S., Cowen, R.K., Shanks, A., Morgan, S.G., Leis, J.M., Pineda, J., Boehlert, G.W., Kingsford, M.J., Lindeman, K.C., Grimes, C., Munro, J.L., 2002. Predicting Self-recruitment in marine populations: biophysical correlated and mechanisms. *Bulletin of Marine Science* 70, 341–375.
- Steinberg, C., 2007. Impacts of climate change on the physical oceanography of the Great Barrier Reef. In: Johnson JE, Marshall PA (eds) *Climate change and the Great Barrier Reef*. Great Barrier Reef Marine Park Authority and Australian Greenhouse Office, Townsville, 51–74.
- Swaney, D.P., Smith, S.V., Wulff, F. 2011. The LOICZ Biogeochemical modeling protocol and its application to estuarine ecosystems. Chapter 8 in Volume 9: *Estuarine and Coastal Ecosystem modelling*, (eds., D. Baird and A. Mehta) in the *Treatise on Estuarine and Coastal Science* (Series eds., E. Wolanski, and D. McLusky), Elsevier. In press.
- Swearer, S.E., Caselle, J.E., Lea, D.W., Warner, R.R., 1999. Larval retention and recruitment in an island population of coral-reef fish. *Nature* 402, 799–802.
- Takeoka, H., 1984. Fundamental concepts of exchange and transport timescales in a coastal sea, *Continental Shelf Research* 3, 311-326.
- Taylor, M.S., Hellberg, M.E., 2003. Genetic evidence for local retention of pelagic larvae in a Caribbean reef fish. *Science* 299, 107–109.
- Turrell, W.R., Brown, J., Simpson, J.H., 1996. Salt Intrusion and Secondary Flow in a Shallow, Well-mixed Estuary. *Estuarine, Coastal and Shelf Science* 42, 153–169.
- Uncles, R.J., Stephens, J.A., Smith, R.E., 2002. The dependence of estuarine turbidity on tidal intrusion length, tidal range and residence time. *Continental Shelf Research* 22, 1835–1856.

- Valle-Levinson, A., 2010. *Contemporary Issues in Estuarine Physics*. Cambridge University Press, United Kingdom, 315pp.
- Valle-Levinson, A., Delgado, J. A., Atkinson, L. P., 2001. Reversing water exchange patterns at the entrance to a semiarid coastal lagoon. *Estuarine, Coastal and Shelf Science* 53, 825–838.
- van Oppen, N.J.H., Lutz, A., De'ath, G., Peplow, L., Kininmonth, S., 2008. Genetic traces of recent long-distance dispersal in a predominantly self-recruiting coral, *PLoS One* 3(10), E3401.
- Vethamony, P., Babu, M., Ramanamurty, M., Saran, A., Joseph, A., Sudheesh, K., Padgaonkar, R., Jayakumar, S., 2007. Thermohaline structure of an inverse estuary: the Gulf of Kachchh: measurements and model simulations. *Marine Pollution Bulletin* 54, 697–707.
- Wu, Y., Falconer, R.A, Lin, B., 2005. Modelling tracer metal concentration distribution in estuarine waters. *Estuarine, Coastal and Shelf Science* 64, 699–709.
- Yanagi, T., 2000 Simple method for estimating V_x from mixing equations in a 1-dimensional, steady-state system for LOICZ biogeochemical modelling. Pages 108-110 in Dupra, V., Smith, S.V., Marshall Crossland, J.I. and Crossland, C.J. 2000. *Estuarine systems of the East Asia region: carbon, nitrogen and phosphorus fluxes*. LOICZ Reports and Studies 16, LOICZ, Texel, The Netherlands, 127 pp.
- Yuan, D., Lin, B., Falconer, R.A., 2007. A modelling study of residence time in a macro-tidal estuary. *Estuarine Coastal and Shelf Sciences* 71, 401–411.
- Walker, T., 1981. Seasonal salinity variations in Cleveland Bay, Northern Queensland. *Australian Journal of Marine and Freshwater Research* 32, 143–149.
- Walker, T., 1982. Lack of evidence for evaporation-driven circulation in the Great Barrier Reef Lagoon. *Australian Journal of Marine and Freshwater Research* 33, 717–722.
- Wang, Y., Ridd, P. V., Heron, M. L., Stieglitz, T. C., Orpin, A. R., 2007. Residence time of solutes and pollutants in the central Great Barrier Reef lagoon, Australia. *Marine and Freshwater Research* 58, 778–791.
- Warner, J.C., Geyer, W.R., Lerczak, J.A., 2005. Numerical modeling of an estuary: A comprehensive skill assessment. *Journal of Geophysical Research* 110(C05001), 1–13.

- Warner, J.C., Geyer, R.W. and Arango, H.G., 2010. Using a composite grid approach in a complex coastal domain to estimate estuarine residence time. *Computers and Geosciences* 36, 921–935.
- Webster, M. A., Petkovic, P., 2005. Australian Bathymetry and Topography Grid, June 2005. Record 2005/12.
- Webster, I., Brinkman, R., Parslow, J., Prange, J., Steven, A., Waterhouse, J., 2008. Review and Gap Analysis of Receiving-Water. Water Quality Modelling in the Great Barrier Reef. Report to Environment and Water Resources. Water for a Healthy Country Flagship, Canberra, 146 pp.
- Webster, I. T., 2010. The hydrodynamics and salinity regime of a coastal lagoon – The Coorong Australia – Seasonal to multi-decadal timescales. *Estuarine Coastal and Shelf Science* 90, 264–274.
- Wellington, G.M., Victor, B.C., 1989. Planktonic larval duration of one hundred species of Pacific and Atlantic damselfishes (Pomacentridae). *Marine Biology* 101, 557–567.
- Williams, D.M., Wolanski, E., Andrews, J.C., 1984. Transport mechanisms and the potential movement of planktonic larvae in the central region of the Great Barrier Reef. *Coral Reefs* 3, 229–236.
- Winant, C. D. and de Velasco, G. G., 2011. Dynamics of hypersaline estuaries: Laguna San Ignacio, Mexico. Chapter 12 in Volume 2: Water and fine sediment circulation, (eds., R.J. Uncles and S.G. Monismith) in the *Treatise on Estuarine and Coastal Science* (Series eds., E. Wolanski, and D. McLusky), Elsevier.
- Wolanski, E., Jones, M., 1979. Biological, chemical and physical observations in inshore waters of the Great Barrier Reef, North Queensland, 1979. Australian Institute of Marine Science, Data Report, Oceanography Series No.2.
- Wolanski, E., Jones, M., Williams, W. T., 1981. Physical properties of Great Barrier Reef lagoon waters near Townsville. II Seasonal variations. *Australian Journal of Marine and Freshwater Research* 32, 321–34.
- Wolanski, E., van Senden, D., 1983. Mixing of Burdekin River flood waters in the Great Barrier Reef. *Australian Journal Marine Freshwater Research* 34, 49–63.
- Wolanski, E., Pickard, G. L., Jupp, D. L. B., 1984. River plumes, coral reefs and mixing in the Gulf of Papua and the northern Great Barrier Reef. *Estuarine Coastal and Shelf Science* 18, 291–314.

- Wolanski, E., Pickard, G. L., 1985. Long-term observations of currents on the central Great Barrier Reef continental shelf. *Coral Reefs* 4, 47–57.
- Wolanski, E., 1986. An evaporation-driven salinity maximum zone in Australian tropical estuaries. *Estuarine Coastal Shelf Science* 22, 415–24.
- Wolanski, E., Burrage, D., King, B., 1989. Trapping and diffusion of coral eggs near Bowden Reef, Great Barrier Reef following mass coral spawning. *Continental Shelf Research* 9, 479–496.
- Wolanski, E., Ridd, P., 1990. Mixing and trapping in Australian tropical coastal waters. pp. 165–183 in Cheng, R.T. (Editor), *Residual Currents and Long-term Transport, Coastal and Estuarine Studies* vol. 38, Springer-Verlag, New York.
- Wolanski, E., 1994. *Physical oceanographic processes of the Great Barrier Reef*. CRC Press, Boca Raton, Florida, 194 pp.
- Wolanski, E., Asaeda, T., Tanaka, A., Deleersnijder, E., 1996. Three-dimensional island wakes in the field, laboratory and numerical models. *Continental Shelf Research* 16, 1437–1452.
- Wolanski, E., Doherty, P., Carleton, J., 1997. Directional swimming of fish larvae determines connectivity of fish populations on the Great Barrier Reef. *Naturwissenschaften* 84, 262–268.
- Wolanski, E., Spagnol, S., 2000. Sticky waters in the Great Barrier Reef. *Estuarine, Coastal and Shelf Science* 50, 27–32.
- Wolanski, E., Brinkman, R., Spagnol, S., McAllister, F., Steinberg, C., Skirving, E., Deleersnijder, E., 2003. Merging scales in models of water circulation: Perspectives from the Great Barrier Reef. pp. 411–427 in Lakhan, V.C. (Editor), *Advances in Coastal Modeling*. Elsevier, Amsterdam.
- Wolanski, E., 2007. *Estuarine Ecohydrology*. Elsevier, Amsterdam, 157 pp.
- Wolanski, E., Andutta, F., Delhez, E., 2012. Estuarine hydrology. In: *Encyclopedia of Lakes and Reservoirs*. Lars Bengtsson, Reginald Herschy, Rhodes Fairbridge (eds.), Springer, In press.
- Wood, T.J., 1979. A modification of existing simple segmented tidal prism models of mixing in estuaries. *Estuarine, Coastal and Shelf Science* 8, 339–347.
- Wu, Y., Falconer, R.A., Lin, B., 2005. Modelling tracer metal concentration distribution in estuarine waters. *Estuarine, Coastal and Shelf Science* 64, 699–709.

Zimmerman, J.T.F., 1976. Mixing and flushing of tidal embayments in the western Dutch Wadden Sea. Part I: Distribution of salinity and calculation of mixing timescales, *Netherlands Journal of Sea Research* 10, 149-191.

Bibliography for chapter 5

- Alongi, D.M., 2002. Coastal Ecosystem processes. CRC Press, Boca Raton, 419 pp.
- Andutta, F, Ridd, P.V., Wolanski, E., 2011. Dynamics of hypersaline coastal waters in the Great Barrier Reef. *Estuarine, Coastal and Shelf Science* 94, 299-305.
- Ayukai, T., Wolanski, E., 1997. Importance of biologically mediated removal of fine sediments from the Fly River plume, Papua New Guinea. *Estuarine, Coastal and Shelf Science* 44, 629–639.
- Bowden, K.F., Gilligan, R.M., 1971. Characteristic features of estuarine circulation as represented in the Mersey Estuary. *Limnology and Oceanography* 16, 490-502.
- Chadwick, D. B., Largier, J.L., 1999. Tidal exchange at the bay-ocean boundary. *Journal of Geophysical Research* 104 (C12), 29901–29924.
- Chicharo, L., Chicharo, M.A., Ben-Hamadou, R., 2006. Use of a hydrotechnical infrastructure (Alqueva Dam) to regulate planktonic assemblages in the Guadiana estuary: Basis for sustainable water and ecosystem services management. *Estuarine, Coastal and Shelf Science* 70, 3–18.
- Day, J.W. Jr., Hall, C.A., Kemp, W.M., Yanez-Aranacibia, A., 1989. *Estuarine Ecology*. John Wiley & Sons, New York, 558 pp.
- de Brauwere, A., de Brye, B., Blaise, S., Deleersnijder, E., 2011. Residence time, exposure time and connectivity in the Scheldt Estuary. *Journal of Marine Systems* 84, 85–95.
- Delhez, E.J.M., Campin, J.-M., Hirst, A.C., Deleersnijder, E., 1999. Toward a general theory of the age in ocean modelling. *Ocean Modelling* 1, 17–27.
- Delhez, E.J.M., Heemink, A.W., Deleersnijder, E., 2004. Residence time is a semi-enclosed domain from the solution of an adjoint problem. *Estuarine, Coastal and Shelf Science* 61, 691–702.
- Diaz, R., J., Rosenberg, R. 1995. Marine benthic hypoxia: A review of its ecological effects and the behavioural responses of benthic macrofauna. *Oceanography and Marine Biology. An Annual Review* 33, 245–303.
- Fischer, H.B., List, E.Y., Koh, R.C.Y., Imberger, J., Brooks, N.H., 1979. *Mixing in Inland and Coastal Waters*. Academic Press, New York, 483 pp.
- FitzGerald, D.M., Knight, J., 2005. *High Resolution Morphodynamics and Sedimentary Evolution of Estuaries*. Springer, Dordrecht, 364 pp.

- Fletcher, C.H. III, VanPelt, J.E., Brush, G.S., Sherman, J., 1993. Tidal wetland record of Holocene sea-level movements and climate history. *Palaeogeography Palaeoclimatology Palaeoecology* 102, 177–213.
- Geyer, W. R., Trowbridge, J. H., Bowen, M. M., 2000. The dynamics of a partially mixed estuary. *Journal of Physical Oceanography* 30, 2035–2048.
- Gillanders, B.M, Kingsford, M.J., 2002. Impact of changes in flow of freshwater on estuarine and open coastal habitats and the associated organisms. *Oceanography and Marine Biology. An Annual Review* 40, 233–309.
- Graneli, E., Turner, J.T., 2006. *Ecology of Harmful Algae*. Springer, Heidelberg. 413 pp.
- Lambeck, K., Chappell, J., 2001. Sea level change through the last glacial cycle. *Science* 292, 679–686.
- Mazda, Y., Wolanski, E., Ridd, P.V., 2007. The role of physical processes in mangrove environments. A manual for the preservation and conservation of mangrove ecosystems. Terrapub, Tokyo, 593 pp.
- McLusky, D.S., Elliott, M., 2004. *The Estuarine Ecosystem Ecology, Threats and Management*. Oxford University Press, Oxford, 214 pp.
- Middelburg, J.J., Herman, P.M.J., 2007. Organic matter processing in tidal estuaries. *Marine Chemistry* 106, 127–147.
- Prandle, D., 2009. *Estuaries: Dynamics, Mixing, Sedimentation and Morphology*. Cambridge University Press, Cambridge, 236 pp.
- Sheldon, J.E., Alber, M., 2006. The calculation of estuarine turnover times using freshwater fraction and tidal prism models: a critical evaluation. *Estuaries and Coasts* 29, 133–146.
- Swaney, D., Smith, S.V., Wulff, F., 2012. The LOICZ Biogeochemical modeling protocol and its application to estuarine ecosystems. Chapter 8 in Volume 9: *Estuarine and coastal ecosystem modeling* (eds., D. Baird and A. Mehta) in the *Treatise on Estuarine and Coastal Science* (Series eds., E. Wolanski, and D. McLusky), Elsevier, Amsterdam.
- Syvitski, J.P.M., Harvey, N., Wolanski, E., Burnett, W.C., Perillo, G.M.E., Gornitz, V., 2005. Dynamics of the coastal zone. pp. 39–94 in Crossland, C.J., Kremer, H.H., Lindeboom, H.J., Marshall Crossland, J.I., Le Tissier, M.D.A., (eds.), *Coastal Fluxes in the Anthropocene*. Springer-Verlag, Berlin, 231 pp.

- Takeoka, H., 1984. Fundamental concepts of exchange and transport time scales in a coastal sea. *Continental Shelf Research* 3, 311–326.
- Turrell, W.R., Brown, J., Simpson, J. H., 1996. Salt intrusion and secondary flow in a shallow, well-mixed estuary. *Estuarine, Coastal and Shelf Science* 42, 153–169.
- Valle-Levinson, A., 2010. *Contemporary Issues in Estuarine Physics*. Cambridge University Press, United Kingdom, 315 pp.
- Warner, J.C., Geyer, W.R., Lerczak, J.A., 2005. Numerical modeling of an estuary: A comprehensive skill assessment. *Journal of Geophysical Research* 110 (C05001), 1–13.
- Warner, J.C., Geyer, R.W., Arango, H.G., 2010. Using a composite grid approach in a complex coastal domain to estimate estuarine residence time. *Computers and Geosciences* 36, 921–935.
- Wolanski, E., 2007. *Estuarine Ecohydrology*. Elsevier, Amsterdam, 157 pp.
- Wolanski, E., Brinson, M., Cahoon, D.M.E., Perillo, G.M.E., 2009. Coastal wetlands. A synthesis. pp. 1–62 in Perillo, G.M.E., Wolanski, E., Cahoon, D.M.E., Brinson, M.M. (eds.), *Coastal Wetlands. An Integrated Ecosystem Approach*. Elsevier, Amsterdam.
- Wu, Y., Falconer, R.A, Lin, B., 2005. Modelling tracer metal concentration distribution in estuarine waters. *Estuarine, Coastal and Shelf Science* 64, 699–709.
- Yuan, D., Lin, B., Falconer, R.B., 2007. A modelling study of residence time in a macro-tidal estuary. *Estuarine, Coastal and Shelf Science* 71, 401–411.
- Zimmerman, J.T.F., 1988. Estuarine residence times, pp. 75–84, in Kjerfve, B. (ed.), *Hydrodynamics of estuaries, Vol 1*. CRC Press.